Functional Oxide Thin Films and Nanostructures: Growth, Interface, and Applications

Guest Editors: Aiping Chen, Ying-Hao Chu, Run-Wei Li, Thomas Fix, and Jia-Mian Hu

Functional Oxide Thin Films and Nanostructures: Growth, Interface, and Applications

Functional Oxide Thin Films and Nanostructures: Growth, Interface, and Applications

Guest Editors: Aiping Chen, Ying-Hao Chu, Run-Wei Li, Thomas Fix, and Jia-Mian Hu

Editorial Board

Bhanu P. Singh, India
Surinder Singh, USA
Vladimir Sivakov, Germany
Ashok Sood, USA
Adolfo Speghini, Italy
Marinella Striccoli, Italy
Xuping Sun, KSA
Ashok K. Sundramoorthy, USA
Angelo Taglietti, Italy
Bo Tan, Canada
Leander Tapfer, Italy
Valeri P. Tolstoy, Russia

Muhammet S. Toprak, Sweden
R. Torrecillas, Spain
Achim Trampert, Germany
Takuya Tsuzuki, Australia
Tamer Uyar, Turkey
Bala Vaidhyanathan, UK
Luca Valentini, Italy
Rajender S. Varma, USA
Ester Vazquez, Spain
Antonio Villaverde, Spain
Ajayan Vinu, Australia
Ruibing Wang, Macau

Shiren Wang, USA
Yong Wang, USA
Magnus Willander, Sweden
Ping Xiao, UK
Zhi Li Xiao, USA
Yangchuan Xing, USA
Doron Yadlovker, Israel
Yoke K. Yap, USA
Kui Yu, Canada
William Yu, USA
Michele Zappalorto, Italy
Renyun Zhang, Sweden

Contents

Editorial

Functional Oxide Thin Films and Nanostructures: Growth, Interface, and Applications

Aiping Chen,[1] Ying-Hao Chu,[2] Run-Wei Li,[3] Thomas Fix,[4] and Jia-Mian Hu[5]

[1]*Center for Integrated Nanotechnologies, Los Alamos National Laboratory, Los Alamos, NM 87545, USA*
[2]*Department of Materials Science and Engineering, National Chiao Tung University, Hsinchu 30010, Taiwan*
[3]*Key Lab of Magnetic Materials and Devices, Ningbo Institute of Material Technology and Engineering,*
 Chinese Academy of Sciences, Ningbo, Zhejiang 315201, China
[4]*Laboratoire ICube, CNRS-Université de Strasbourg, 67037 Strasbourg, France*
[5]*Department of Materials Science and Engineering, Pennsylvania State University, University Park, PA 16802, USA*

Correspondence should be addressed to Aiping Chen; apchen@lanl.gov

Functional oxides with novel physical/chemical properties have applications from optoelectronic devices, photocatalyst and information storage to biomedical applications, water splitting, and energy storage. The fascinating physical properties are strongly related to their electronic structures, surface morphology, interface, microstructure, defect, strain, and so forth [1–4]. Therefore, revealing the effect of these factors on functionalities is a key step to achieve practical applications of these oxides.

This special issue presents the synthesis, fabrication, and potential applications of metal oxide thin films and nanostructures. It was known that microstructure and strain play critical roles in physical properties in oxide thin films [5]. The research papers in this special issue further confirm that microstructures, surface morphology, interface, defect, and strain are connected with functionalities in different types of metal oxide thin films and nanostructures.

First set of papers are exploring the chemical synthesis of ZnO nanostructures to enhance the photocatalytic and photoelectrochemical reactions. For instance, N. A. Abd Samad et al. in their work titled "Easy Formation of Nanodisk-Dendritic ZnO Film via Controlled Electrodeposition Process" highlighted the newly developed nanodisk-dendritic ZnO film, which can harvest more incident photons to generate more photoinduced charge carriers to trigger the photocatalytic and photoelectrochemical reactions. A.-J. Wang et al. in a paper titled "Facile Synthesis of Rambutan-Like

ZnO Hierarchical Hollow Microspheres with Highly Photocatalytic Activity" reported the improved photocatalytic activity for the degradation of rhodamine B under ultraviolet irradiation. After 90 min of UV irradiation, almost 100% of RhB molecules are decomposed for rambutan-like ZnO hierarchical hollow microspheres, unlike that of commercial ZnO with 23% of RhB molecules remaining. This work not only provides a simple method to prepare ZnO hollow structures but also sheds some light on the improvement of the photocatalytic performance by designing efficient catalysts.

Y. Liu et al. in a paper titled "Electrohydrodynamic Processing of p-Type Transparent Conducting Oxides" reported the synthesis of p-type transparent conducting oxide films such as ZnO and $CuAlO_2$ thin films by electrospray electrospinning methods. The optical and electrical properties of these films have been carefully analyzed. The emerging applications of $CuAlO_2$ as potential nanobuilding block have been discussed.

Defect significantly affects the properties in thin films and nanostructures. Oxygen vacancy is an important type defect in oxides [6]. R. Félix et al. in a paper titled "The Role of Edge Dislocations on the Red Luminescence of ZnO Films Deposited by RF-Sputtering" investigated the oxygen pressure dependence of structural and optical properties of ZnO films. The major defects have been identified as edge dislocations. The TEM characterization indicates that films

deposited at low oxygen pressure present a higher density of threading dislocations. The red band shift has been found to correlate with the amount of edge dislocations.

C. L. Popa et al. in their work titled "Inhibitory Effect Evaluation of Glycerol-Iron Oxide Thin Films on Methicillin-Resistant *Staphylococcus aureus*" reported the inhibitory effect of glycerol-iron oxide thin films on methicillin-resistant *Staphylococcus aureus*. The results suggest that glycerol-iron oxide thin films could be used in the future for various biomedical and pharmaceutical applications.

Interface is another important factor in metal/oxide multilayers [7]. H. Jiang et al. in a paper titled "Fabrication and Characterization of Al/NiO Energetic Nanomultilayers" studied the redox reaction in Al/NiO nanomultilayers. The interface effect was studied by deposited multilayers with different periodicity. It was found that the thermal diffusion time becomes greater as the amount of thermal boundary conductance across the interfaces increases with relatively smaller modulation period. Therefore, the interface of the Al/NiO strongly influences the performance of energetic igniter.

Strain plays a critical role in controlling the growth and the properties of functional oxide thin films [8, 9]. B. Ifland et al. in a paper titled "Strain Driven Phase Decomposition in Ion-Beam Sputtered $Pr_{1-x}Ca_xMnO_3$ Films" used $Pr_{1-x}Ca_xMnO_3$ films as a model system to study the influence of strain on the Mn solubility in perovskite oxide thin films. They observed that large tensile strain during deposition limits the Mn solubility of the perovskite phase. Mn excess gives rise to precipitates and the precipitation seems to represent a stress relaxation path.

The guest editors hope that this special issue can stimulate further research in the field of functional oxide thin films and nanostructures.

Acknowledgments

Aiping Chen
Ying-Hao Chu
Run-Wei Li
Thomas Fix
Jia-Mian Hu

References

[1] V. T. Tra, J.-C. Yang, Y.-H. Hsieh, J.-Y. Lin, Y.-C. Chen, and Y.-H. Chu, "Controllable electrical conduction at complex oxide interfaces," *Physica Status Solidi—Rapid Research Letters*, vol. 8, no. 6, pp. 478–500, 2014.

[2] T. Fix, E.-M. Choi, J. W. A. Robinson et al., "Electric-field control of ferromagnetism in a nanocomposite via a ZnO phase," *Nano Letters*, vol. 13, no. 12, pp. 5886–5890, 2013.

[3] J.-M. Hu, L.-Q. Chen, and C.-W. Nan, "Multiferroic heterostructures integrating ferroelectric and magnetic materials," *Advanced Materials*, vol. 28, no. 1, pp. 15–39, 2016.

[4] X. Zhu, F. Zhuge, M. Li et al., "Microstructure dependence of leakage and resistive switching behaviours in Ce-doped $BiFeO_3$ thin films," *Journal of Physics D: Applied Physics*, vol. 44, no. 41, Article ID 415104, 2011.

[5] A. P. Chen, Z. X. Bi, Q. X. Jia, J. L. MacManus-Driscoll, and H. Y. Wang, "Microstructure, vertical strain control and tunable functionalities in self-assembled, vertically aligned nanocomposite thin films," *Acta Materialia*, vol. 61, no. 8, pp. 2783–2792, 2013.

[6] R. Zhao, W. W. Li, A. P. Chen et al., "Manipulating leakage behavior via distribution of interfaces in oxide thin films," *Applied Physics Letters*, vol. 105, no. 7, Article ID 072907, 2014.

[7] G. Radaelli, D. Petti, E. Plekhanov et al., "Electric control of magnetism at the $Fe/BaTiO_3$ interface," *Nature Communications*, vol. 5, article 3404, 2014.

[8] A. P. Chen, H. H. Zhou, Z. X. Bi et al., "A new class of room-temperature multiferroic thin films with bismuth-based supercell structure," *Advanced Materials*, vol. 25, no. 7, pp. 1028–1032, 2013.

[9] J. H. Haeni, P. Irvin, W. Chang et al., "Room-temperature ferroelectricity in strained $SrTiO_3$," *Nature*, vol. 430, no. 7001, pp. 758–761, 2004.

Research Article

Electrohydrodynamic Processing of p-Type Transparent Conducting Oxides

Yin Liu, Sureeporn Pollaor, and Yiquan Wu

New York State College of Ceramics at Alfred University, Alfred, NY 14802, USA

Correspondence should be addressed to Yiquan Wu; wuy@alfred.edu

Electrohydrodynamic processing is capable of synthesizing various materials in the form of porous/dense thin films, nanofibers, nanorods, nanobelts, and ribbons, which is highly favorable for functional oxides. The tailored microstructures and properties derived from electrohydrodynamic forming also give rise to new research interests on some classical oxides, such as transparent conducting oxides (TCOs). Here a case of feasible electrospray synthesis of classical ZnO is demonstrated with tailored p-type conductivity. Another p-type TCO, $CuAlO_2$, was prepared by both electrospray and electrospinning methods and the processing-derived electrical and optical properties are demonstrated. The last part of the paper discusses some emerging applications especially for $CuAlO_2$ as potential nanobuilding blocks enabled by electrohydrodynamic processing.

1. Introduction

The electrohydrodynamic phenomenon, which describes the interaction between liquid and electrical field, has been discovered for over one hundred years. However, the incorporation of this phenomenon into practical material processing approaches has just become available in recent decades [1–4]. The basic concept lies in the fact that the liquid meniscus escaping the capillary tip under electrical field would deform into a conical shape (Taylor core), from where the submicrometric liquid jet is formed. The jet could either go through physical disruption after propulsion to form monocharged nanodroplets or maintain its single wire shape, mainly depending on the viscoelasticity and dielectric properties. The former is called electrospray, while the latter is electrospinning. These two techniques have been widely utilized in synthesizing a large variety of materials ranging from polymers, ceramics, and metals to composites [5–8], with the forms of thin films, nanofibers, and nanobelts. The electrohydrodynamic derived technique could also rival other nanoscale fabrication techniques due to its simple setup and versatile capabilities in tailoring the nanostructure and properties. On the other hand, since there has been growing research interest in nanobuilding blocks for some emerging

technologies such as photocatalyst, thermoelectrics, batteries, and nanophosphors, this recalls the demand to employ electrohydrodynamic processing to fabricate classic and new materials in both low dimensions and various morphologies. Even though the electrohydrodynamic processing was originally designed for polymeric products, it is also capable of fabricating ceramics from either chemical solutions or suspensions. Table 1 lists some low dimensional oxide materials fabricated by electrohydrodynamic processing from previous reports. The main idea of fabricating the n- and p-type oxides through electrohydrodynamic processing is to firstly prepare and deposit the precursor solutions containing the desired ion species on substrates and then calcine the precursors to initiate crystallization. Besides the merits of simple setup and cost-efficiency, the electrohydrodynamic processing involves fewer preparation steps and exhibits good repeatability and potential in large-scale production, which is favorable for thin film technology and other emerging optoelectronic devices.

In our study, two oxide materials, $CuAlO_2$ and ZnO (crystal structure as shown in Figure 1), were discussed, which are both generally regarded as good candidates for transparent conducting oxides (TCOs), a class of materials with synergistic electrical conductivity and optical transmittance. Due to these unique properties, TCO has been widely used as

(a)   (b)
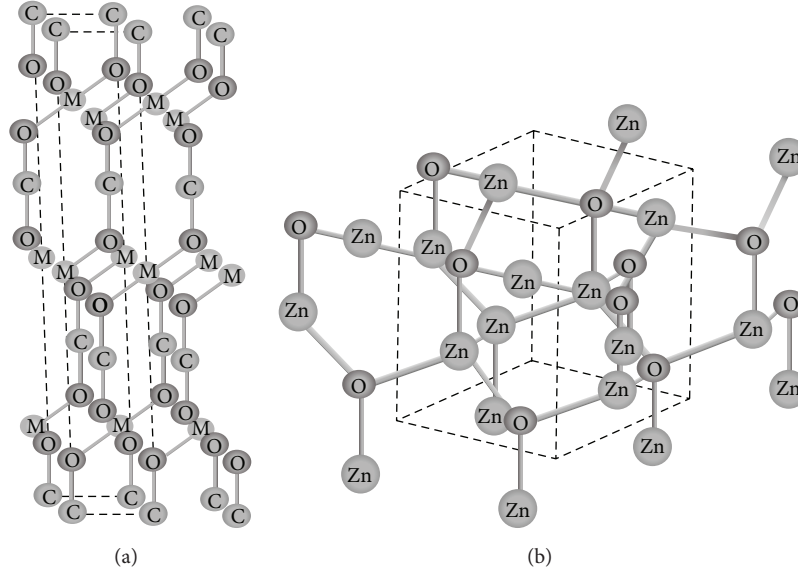
FIGURE 1: The delafossite CMO_2 (a) and wurtzite ZnO structures (b).

TABLE 1: Recent advances in oxide materials synthesized by electrohydrodynamic processing.

Materials	Morphology	Applications	Reference
AZO/ITO	Thin film	TCO	[26]
TiO_2	Core-shell spheres	DSSC	[27]
TiO_2	Nanofibers	Photocatalyst/batteries	[28]
TiO_2/SnO_2	Nanofibers	Photocatalyst	[29]
TiO_2/ZnO	Nanofibers	Photocatalyst	[30]
NiO-CdO	Nanofibers	Sensors	[31]
YSZ	Thin film	SOFCs	[32]
YSZ	Nanofibers	—	[33]
SnO_2	Thin film	Gas sensor	[34]
ZnO	Thin film	TCO	[35]
CdO	Nanofibers	TCO	[36]
CeO_2	Nanofibers	Capacitors, catalyst	[37]
Al_2O_3	Nanofibers	—	[38]
Ga_2O_3	Nanofibers	TCO	[39]
$LiCoO_2$	Wires	Cathode	[40]
MgO	Nanofibers	Luminescence	[41]

building blocks in architectural applications [9], flat-panel displays including OLEDs, liquid crystal displays, and plasma displays [10], light emitting diodes [11], biosensors [12], and other emerging optoelectronic devices in its form of coatings, thin films, or wires. Most TCOs exhibit unintentional n-type conductivity and degenerate doping could be utilized to achieve a comparable resistivity (in the order of magnitude 10^{-4}–10^{-2} $\Omega \cdot$cm) and carrier density ($\sim 10^{20}$ cm^{-3}) to conventional semiconductors. Unfortunately, there is no active junction device using TCOs to the best of our knowledge, mainly due to the monopolarity of the n-type TCOs [13, 14]. Notwithstanding the lack of research in p-type TCOs compared to n-type ones, the p-type TCOs are essential for

constructing the p-n functional window in which UV portion of the solar radiation could be absorbed by the electronics, while visible light can be transmitted [15]. The combination of the two types of TCOs not only is an effective approach to improve the optoelectronic performance but also is of great futuristic value to build up the "invisible electronics" [16], such as electronic paper and heads-up displays. $CuAlO_2$ is the first reported p-type TCO without intentional doping by Kawazoe et al. [17] in 1997. The most distinguished feature for this material is its anisotropic electrical conductivity [18] stemming from the delafossite structure (Figure 1(a)) and the linearly coordinated copper atoms. However, the development of this material has lagged far behind that of n-type TCOs, mainly due to two reasons. The first reason is its inherently low conductivity and difficulty in degenerate doping. Even though there have been a few reports on using divalent dopants such as Mg and Ca [19–21] to increase the hole concentration, the dominant O_2p states underlying the conduction band may strongly localize the extrinsic hole carriers [22]. The second reason lies in the fact that the conductivity highly depends on processing parameters and usually a wide range of optical bandgap values are reported from different synthesizing methods. There have been few reports [23, 24] on $CuAlO_2$ via electrohydrodynamic processing, which would be a reproducible and cost-effective method for fabricating thin films and fibers. ZnO, on the other hand, has been long used for n-type optoelectronic devices for decades. As shown in Figure 1, ZnO with wurtzite structure possesses large band gap and large portion open space, which is suitable for doping. However, it encounters the similar processing and doping issues as a p-type semiconductor mainly because of the self-compensation from native donor defects (Zn_i and V_O) [25]. By using the electrospray technique, we selected lithium (acceptor, A) and aluminum (donor, D) as the codopants to achieve the improvement in conductivity and the mitigation of lattice distortion simultaneously. The
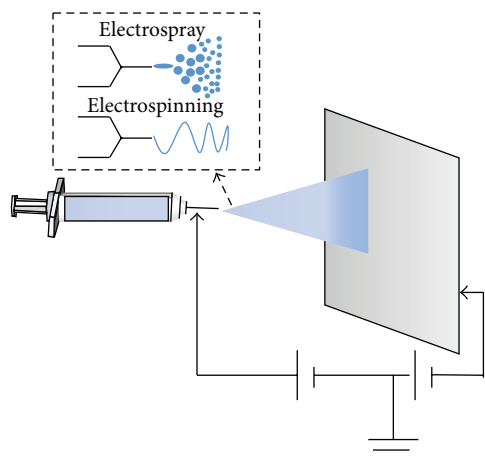
FIGURE 2: A general setup of electrohydrodynamic processing with droplets or a single fiber exiting the capillary under the forward bias electrical field.

enhanced dopant solubility in the present ZnO may shed new light on constructing homojunction devices.

2. Electrohydrodynamic Synthesis of p-Type CuAlO$_2$

2.1. Experimental Setup. A combination of electrohydrodynamic jet forming and modified sol-gel method was developed to synthesize CuAlO$_2$ ceramics directly from chemical solutions. Stoichiometric Cu(NO$_3$)$_2$·3H$_2$O (Sigma-Aldrich, puriss. p.a.), Al(NO$_3$)$_3$·9H$_2$O (Sigma-Aldrich, ACS reagent), and dopant ions (Y^{3+} and Ln^{3+}) in nitrate form were used as the starting agents dissolved in corresponding solvents. In the case of CuAlO$_2$ thin film fabrication through electrospray, nonaqueous precursor (1:1 ethylene glycol/ethanol, 0.5 M) was prepared and stirred at 70°C. Then a polyacrylamide route [42] was used in which acrylamide, N,N bis-methylene acrylamide, and ammonium persulfate were added to the solution one by one. The as-formed polyacrylamide gel could provide a diphasic medium to immobilize the precursor solution and render the feasible low-temperature synthesis for CuAlO$_2$ formation. For electrospinning precursor, the above metal salts were firstly dissolved in methanol and then mixed with citric acid solution. Polymeric agent Polyvinylpyrrolidone (PVP) (Sigma-Aldrich, average mol. wt. 40,000) was further added to the gel in the attempt to acquire suitable viscoelasticity for electrospinning. As shown in Figure 2, a home-built electrohydrodynamic jet forming setup utilizing DC high voltage was used for both electrospray (5–8 kV, 0.1 and 0.5 mL/h) and electrospinning (15–18 kV, 1 mL/h). The resultant jet-formed products deposited onto quartz substrates went through heat treatment at various temperatures to investigate the phase evolution.

2.2. Microstructure and Crystal Phase Evolution through Electrohydrodynamic Processing and Successive Heat Treatment. The microstructure through electrohydrodynamic processing could be highly tailored into various forms, while the crystallite size could remain at the submicron level. The key challenges to electrospray and electrospinning are to acquire dense thin films and uniform fiber dimensions through a stable electrohydrodynamic jetting. Due to the inherent complexity of the electrohydrodynamic jet forming and propulsion, the parameter optimization is still on the experimental basis and solid theoretical models that encompass pertinent variables have yet to be built. We herein show the examples of several processing parameters influencing microstructure evolution. Figure 3 is a brief summary of different microstructures generated under different spray rate, electrical field, and working time. The as-spray film exhibited amorphous topography consisting of overlapping monodispersed droplets. Upon heat treatment (800°C in argon) and the decomposition of organics, discrete spherical particles were formed on the substrate, and at an optimum electrospray condition shown in Figure 3(e) dense films of ~4 μm thickness were obtained (also confirmed from cross section view from Figure 3(f)). The electrical field required for electrospinning is higher due to significant dielectric constant increase in the viscous precursors tuned by high molecular weight PVP. The jet formed at the capillary would be a single cylindrical fiber with elongation and thinning effects, as long as a suitable electrohydrodynamic condition could be met. At the low voltage applied under 2000 V/cm, the microstructure of the as-spun fibers prior to thermal treatment is a mixture of droplets and fibers, indicating a transitional electrohydrodynamic jet forming deviated from electrostatic balance in which the conical jet is unstable with charged droplet encapsulated into the jet stream. Even though this special microstructure is of great importance in some applications such as drug delivery, the mixed structure cannot meet the requirements of producing uniform and interconnected fibrous ceramic coatings for optoelectronic applications. By using an electrical field of 2000 V/cm, uniform fibers could be formed and the self-sustained network could survive after thermal treatment, during which polymeric fibers were transformed into polycrystalline CuAlO$_2$. The enlarged micrograph of Figure 4(f) shows one single submicron fibers with fine polycrystalline grains.

Due to the narrow thermodynamic window of delafossite CuAlO$_2$ phase, various annealing temperatures were examined on both thin film and fibrous samples. According to the XRD results shown in Figure 5, at 500°C, only CuO phase was present due to the thermal decomposition of copper nitrate. With the help of acrylamide gelification, the crystallinity significantly improved after annealing in argon at 800°C, whereas this is not the case when no acrylamide was involved even at a higher annealing temperature. There was no intermediate phase such as spinel CuAl$_2$O$_4$ identified. For the case of the precursor used for electrospinning, which is simply a citrate-nitrate system, the spinel CuAlO$_4$ was formed by the following reaction: CuO + Al$_2$O$_3$ → CuAl$_2$O$_4$ at 900°C. According to the phase equilibria in the system of Cu$_2$O-CuO-Al$_2$O$_3$ [43], CuAlO$_4$ and CuO phases containing Cu(II) are stable at the temperature range of 625 to 1000°C, whereas the delafossite CuAlO$_2$ is a metastable phase below 1000°C, which could be decomposed to CuAlO$_4$. Single delafossite phase (CuAlO$_2$, rhombohedral, PDF#35-1401) was
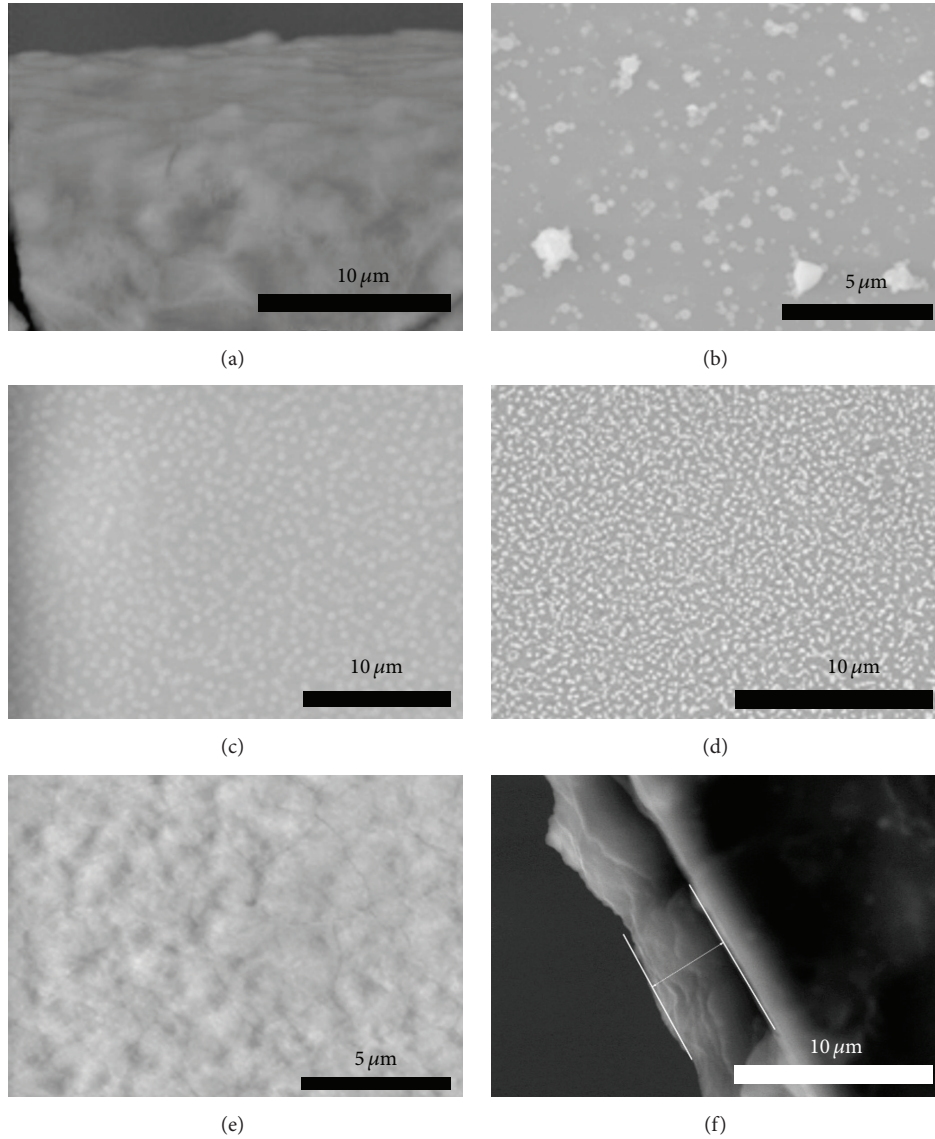
FIGURE 3: SEM microstructures of electrosprayed CuAlO$_2$: (a) as-sprayed without heat treatment from tilt view; (b) spray rate, 0.1 mL/h, electrical field, 500 V/cm, and spray time, 5 min; (c) spray rate, 0.5 mL/h, electrical field, 500 V/cm, and spray time, 10 min; (d) spray rate, 0.5 mL/h, electrical field, 1000 V/cm, and spray time, 15 min; (e) spray rate, 0.5 mL/h, electrical field, 1000 V/cm, and spray time, 30 min, with cross section image shown in (f).

formed in its stable form after annealing at 1100°C for 3 hr. The reaction formula is as follows:

$$CuO + CuAl_2O_4 \longleftrightarrow 2CuAlO_2 + \left(\frac{1}{2}\right)O_2 \qquad (1)$$

2.3. Electrical and Optical Characterizations of CuAlO$_2$ Thin Films and Nanofibers. Due to the poor p-type conductivity of delafossite CuAlO$_2$, there have been many attempts to improve the electrical conductivity, such as divalent doping [19–21] and nitrogen doping [44]. Trivalent dopant in substitution of Al site has become a new experimental interest in recent years. Based on some calculation results [22], the substitution doping is predicted to increase the density of

states at the top of the valence band. Additionally, the change of M-O covalency could lead to a decrease of O valance charge in the Cu-O-Al unit, which finally mediates Cu d states and an improved conductivity would be expected. Inspired by CuYO$_2$ compounds and the potential alloying effects, Y ion was chosen to partially substitute Al site. Figure 6 depicts three typical electrical characterization methods. All the samples exhibited semiconducting conductivity with a monotonically reduced thermal activation energy as the yttrium doping increased. Even though the various hopping mechanisms in CuAlO$_2$ have been reported, at the measured temperature range, the linearity indicted a thermal activation type hopping. Recalling the change of optical direct band gap shown in Figure 6(c), the introduction of yttrium modified
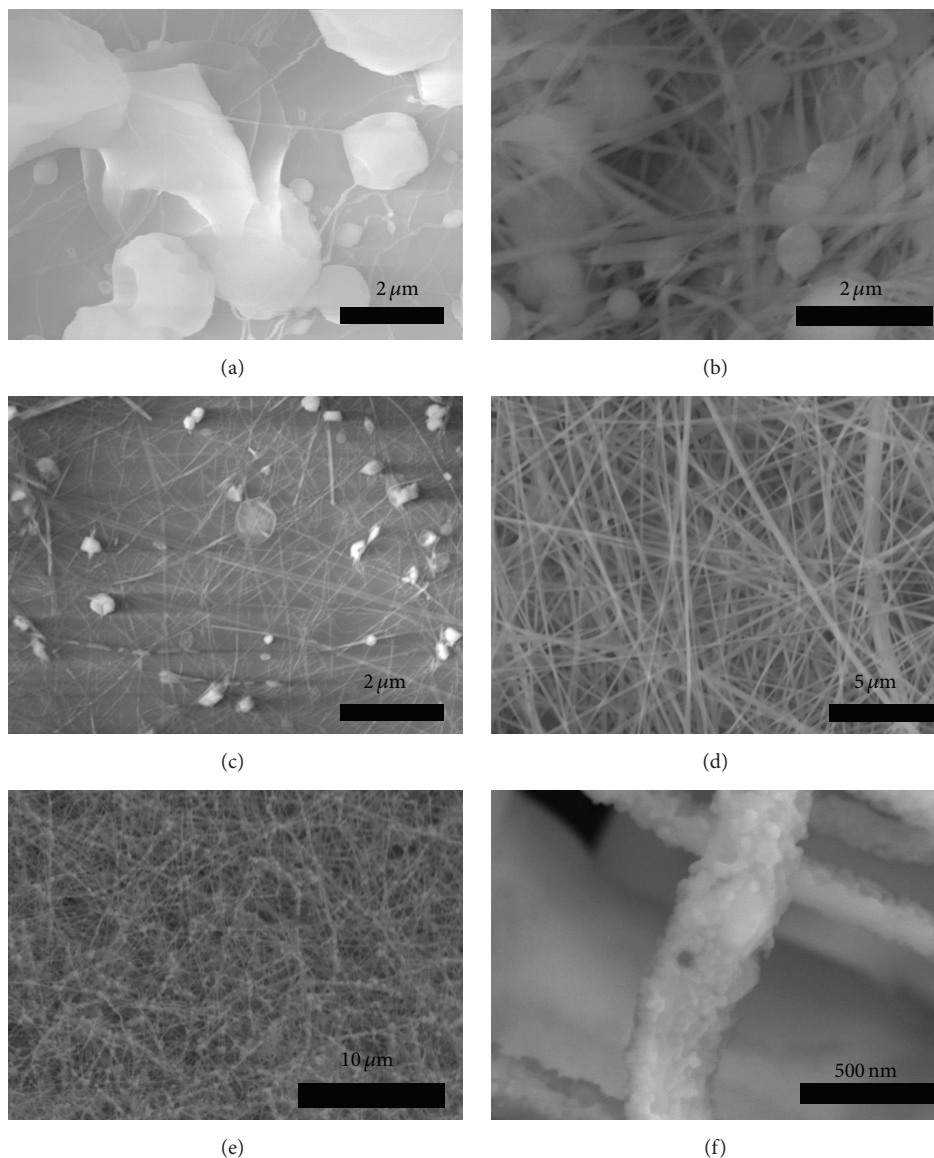
FIGURE 4: CuAlO$_2$ nanofibers fabricated through electrospinning: (a) as-spun, 500 V/cm; (b) as-spun, 1000 V/cm; (c) as-spun, 1500 V/cm; (d) as-spun, 2000 V/cm; (e) and (f) fully crystallized, annealed at 1100°C.

the band edge and might change Cu-O confinement to a degree that the excitons underlying the valence band became more delocalized, thus decreasing the activation energy when thermally excited from VB to CB. The overall resistivity obtained from calculating the V-I slope shows a decrease from 689 Ω·cm to 580 Ω·cm as the Y concentration goes up from 0 to 5 at.%. Even though the improvement is very small, the consistency lying within the band gap, resistivity, and thermal activation energy might indicate that the substitutional trivalent doping with orderly alloying effects could be useful for a better understanding of the doping mechanisms compared to divalent doping, which may increase the charge complexity and obscure some underlying phenomena.

The fate of electrohydrodynamic is its simplicity in producing nanostructured coatings or thin films with high transparency in the visible region, which is highly favored by

transparent conducting oxides. The samples could be easily deposited onto glass or quartz substrates due to the strong attractive force between charged jet and grounded collector. After annealing, the polycrystalline structure could be formed. The sample from electrospray (shown in Figure 3(f)) has a lowered transmittance in the visible region in Figure 7. The dense polycrystalline delafossite anisotropic structure could enhance the beam scattering, thus decreasing the transmittance. On the other hand, the electrospun sample with a stacking thickness of ~20 μm [6] has a porous structure and due to the stacking of fiber mats and reduced contact area, the actual coating thickness absorbing the visible light could not be high. Therefore, the electrospun sample exhibited higher transmittance compared to the electrospray coating.

Another striking fact about CuAlO$_2$ is the room temperature near-band-edge emission in the UV/blue region,

(a)

(b)
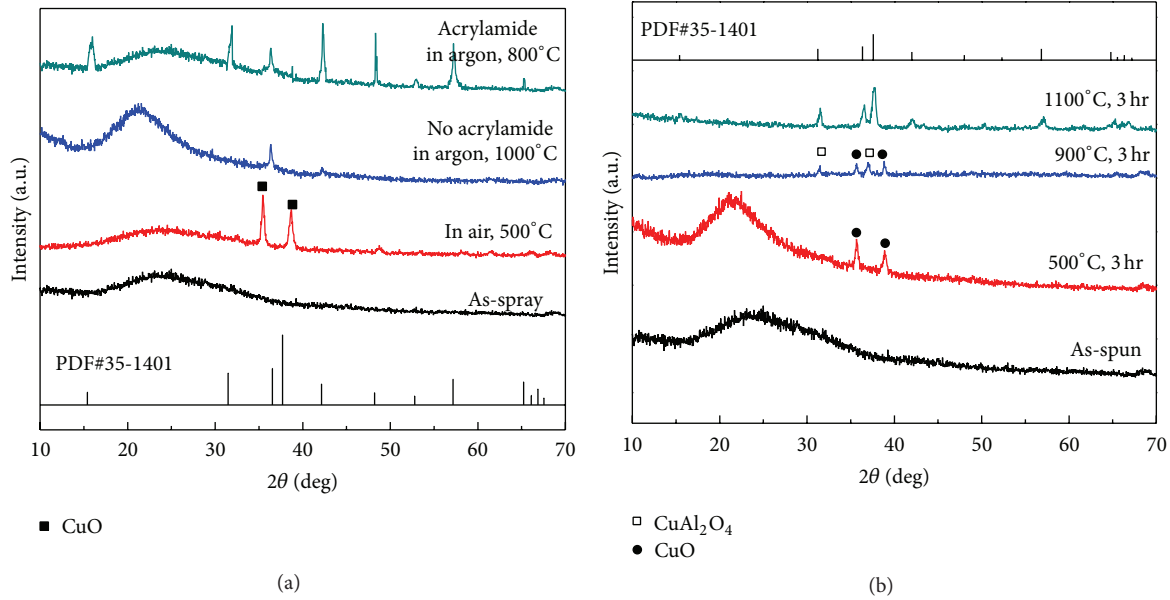
FIGURE 5: The XRD patterns of the electrospray (a) and electrospinning (b) products with respect to different heat treatment conditions.

making it a promising luminescent candidate. In delafossite $CuAlO_2$, Cu-O bonds in O-Cu-O dumbbell layers determine the electronic structure near the band gap and lead to strong localization of excitons in the x-y plane as well as larger binding energy. Since the binding energy exceeded the room temperature thermal energy ($kT \approx 0.025$ eV), room temperature PL emissions were presented. Our recent study [24] also showed that this near-band-edge emission might be also closely associated with Cu 3d/4p hybridization as a result of trivalent site mediation. The electrohydrodynamic processing could enable us to deposit $CuAlO_2$ precursors with different doping species and concentration and obtain the transparent sample ready for optical characterization. Figure 8 includes three samples with different trivalent site configurations. Distinct peak shift is identified, showing different Stokes shifts of d($3d_z^2$-4s) $\rightarrow$ $3d^9 4p^1$ transition. However, the trend showing here is in contradiction with the claim that this Stokes shift decreases as the size of the trivalent metal atom reduces [45]. The nanostructure fibers or thin films on the other hand could also contribute to the Stokes shift, usually a blue shift in the luminescence spectra. Therefore, the modification of the morphology and dimension of those nanostructures could generate tunable luminescence.

While most researchers focus on the electrical properties of $CuAlO_2$ as a p-type transparent conducting oxide, there are few reports in viewing $CuAlO_2$ as a potential phosphor material. In addition, with the development of field emission display and other flat display technologies, new generation of phosphors with good luminescence, conductivity, and stability is required. $CuAlO_2$ could be a promising host material in which Al site could be substituted with various trivalent rare earth dopants, without changing the hole transport within Cu^+ plane [46]. Since the main conduction path in delafossite crystals is close-packed Cu^+

layers [18], the electrical properties could be sustained in addition to photoluminescence properties. Conventional solid-state synthesis of $CuAlO_2$ powders or thin films requires high temperature sintering and repeated thermal treatments. We hereby prepared $CuAlO_2$ fibers via a cost-effective electrospinning method. The wire-like $CuAlO_2$ nanostructures possess higher surface area and sintering activity, which could lower the annealing temperature. Additionally, the one-dimensional material may also present extraordinary effectiveness in light emitting and transparent conducting [47–49]. Eu^{3+} cation was chosen as the emission activator and intense red emission from f-f transition of Eu^{3+} was identified. Eu^{3+} activator center was successfully doped into Al^{3+} site and this delafossite-type material could be used as potential host for luminescence application.

3. Electrospray Synthesis of Codoped ZnO

3.1. Experimental Setup and Thin Film Topography. The electrosprayed ZnO with codopants could be synthesized from a similar chemical solution method, in which $Zn(CH_3COO)_2 \cdot 2H_2O$ (Fisher Scientific), $AlN_3O_9 \cdot 9H_2O$ (≥98%, Sigma-Aldrich), and CLi_2O_3 (≥99%, Sigma-Aldrich) were dissolved in 9:1 v/v of Diethylene Glycol (≥99% BioUltra $C_4H_{10}O_3$, Sigma-Aldrich) and deionized water solution. For electrospray, a deposit rate of 0.06 mL/hr with applied voltage of 20.0 kV and 15 cm of deposit distance were used to deposit nanodroplets onto preheated substrate (93 ± 5°C) for 60 minutes. The as-sprayed substrates were annealed in air at 500°C for 5 hr. The crystallized ZnO thin films after calcination have an average thickness of ~160 nm.

3.2. Effects of Codoping on Morphology and Electrical Properties. The aim of using codopants is to mitigate lattice

(a)

(b)

(c)
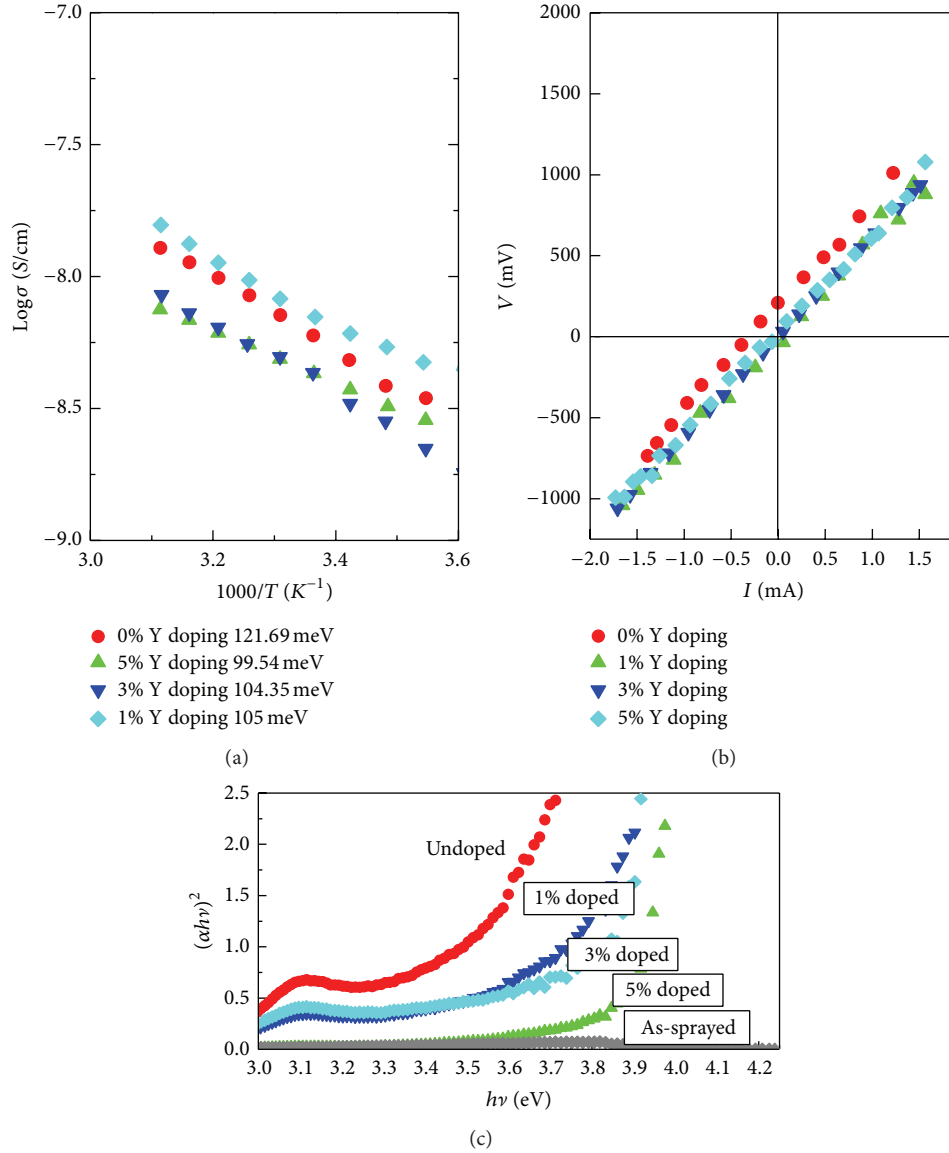
FIGURE 6: Summary of electrical properties of electrosprayed CuAlO$_2$ thin films. (a) Temperature-dependent DC conductivity. (b) Four-probe V-I curve. (c) Tauc plot extrapolated from UV diffuse reflectance.

distortion introduced by aluminum ions. From XRD shown in Figure 9, the degree of crystallinity decreased with the increase of Al concentration as shown in FWHM (002). The average introduced stress from the difference radii between the host and dopant restrained growth process. Moreover, the substitute defect was formed and increased a compressive stress that induced a degenerated issue resulting in small grain size. In contrast, after incorporating Li ions, the FWHM rarely changed over %Al range of dopant resulting in crystallite size remaining almost constant, indicating a stress relaxation and better crystallization took place. Less stress was introduced in the 3% Li-doped sample due to the smaller difference of radii between Zn and Li. By employing the Double-Voigt approach based on the diffraction patterns (002), the strain e$_0$ for undoped ZnO is ~0.0036 and it increased slightly to ~0.0046 in the 3% Li-doped ZnO thin

film. Therefore, the lattice distortion in Li codoped ZnO samples was kept constant as %Al increases indicating that the dopant solubility improved by codoping mechanism. However, the lattice distortion increased when Al concentration increased due to the small size of Al and less contraction at c-axis when being substituted on the Zn site.

The AFM in Figure 10 reveals the general topography of samples with different doping configurations. Undoped and Li-doped ZnO samples exhibited larger grain size compared to other doped and codoped ZnO samples. At 3.0% Al-doped ZnO has a large size difference compared to host (Zn^{2+}), so the stress caused a degenerated issue resulting in small grain size being observed which was consistent with crystallite size studies. It is noteworthy that introducing of the second Li dopant could smooth the thin film surface and a significant drop in RMS was also observed in Table 2. This improvement

TABLE 2: Roughness evolution observed by AFM from undoped and codoped ZnO samples.

Sample detail	Average roughness (nm)	RMS roughness (nm)	Skewness
Undoped ZnO	9.1591	11.5280	0.3712
3% Li-doped ZnO	5.3446	6.5457	−0.2644
3% Al-doped ZnO	33.6361	41.592	−0.1874
3-3% Al-Li codoped ZnO	13.6971	16.7416	0.0468
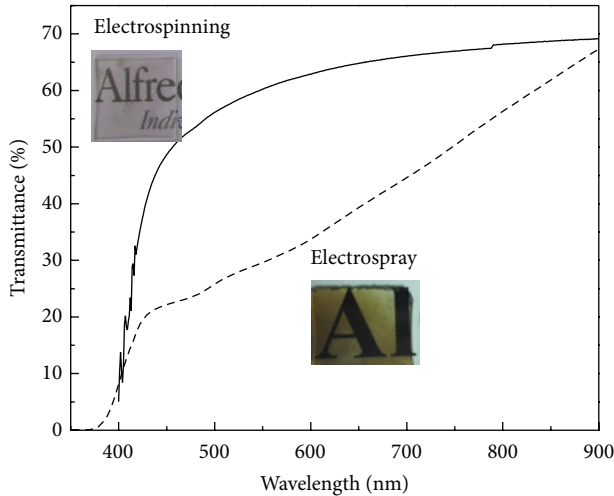
FIGURE 7: Transmittance spectra of $CuAlO_2$ coatings from both electrospray and electrospinning.

in thin film quality is also considered to be associated with the relaxation of lattice strains allowing growth process. The Li ions increased dopant solubility and accommodated Al to localize with minimal stress.

A visible transmittance of 85%–90% could be achieved in the electrosprayed samples as shown in Figure 11. As Al^{3+} went up, transmittance in visible range increased because there was no segregation of Al at grain boundary and Al_i defect as scattering centers. Another plausible reason lies in the fact that AlO_6 octahedron was reported [50] to decrease the surface roughness, which could also help increase the in-line transmittance. Li promoted solubility and facilitated grain growth, which improved the transmittance by mitigating grain boundary effect. A presence of Li in codoped ZnO showed higher transparency suggesting that there was no interstitial Li (Li_i) defect or near-band-edge defect to increase light absorption in visible range meaning that the defect complex (Li_{Zn}-Li_i) was formed. Therefore, the reduction of charge effective carrier was observed.

The Burstein-Moss effect or band gap widening was observed in all doped samples due to the fact that the excess charge carriers by dopants were blocked at the lowest part of the conduction band. The double occupation is prohibited according to Pauli exclusive principle. However, the band gap energy of Li codoped samples was maintained because the
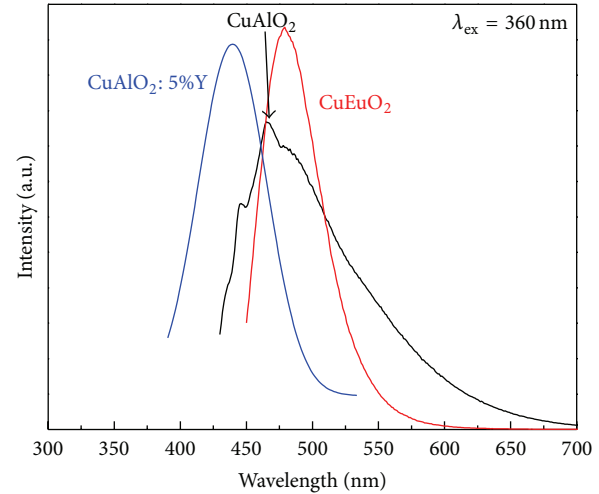

FIGURE 8: Room temperature photoluminescence of 3 delafossite samples synthesized via electrospinning.

defect complex was formed to reduce ionic defects and thus electronic defects were decreased.

The electrical properties results in Table 3 reveal that all Li-doped ZnO films showed p-type semiconductor meaning that hole carriers were dominated in an electrical conductivity. The resistivity and the resistance of as-annealed films by Hall-effect measurement and in-line 4-point probe measurement showed the same tendency. A 1.5–3% (Al, Li) codoped ZnO film showed the lowest resistance, resistivity, and sheet resistivity of the film of 9.6 Ohm, 9.59 Ohm·cm, and 29.5 Ohm/cm^2, respectively. The carrier mobility was 9.51 cm^2/Vs and the carrier density was 6.85×10^{16} cm^{-3}. This phenomenon can also be explained in terms of mobility effect which was improved by enhancing dopant solubility at the optimal acceptor-to-donor ratio of 2 : 1. The highest solubility indicated by the lowest lattice distortion suggested that the incorporation of acceptor improved by forming acceptor-donor (A-D-A) defect complex resulting in the electronic band structure being tailored to enhance the efficiency of charge carrier transportation [51]. This A-D-A defect complex shifted acceptor and donor energy levels close to the valence and conduction bands, respectively, by electrostatic force. These periodical A-D-A defect complexes or trimmers induced a short-range dipole-like scattering mechanism resulting in a decrease of mobility scattering [52]. Moreover, the grain boundary was diminished as shown in SEM image, so the grain boundary scattering exhibited the smallest effect compared to other doped ZnO-based films. The lowest resistivity was observed in the 1.5–3% Al-Li codoped ZnO due to the increased hole mobility in order to compensate for the loss of carrier from a native defect or a defect cluster (Li_{Zn}-Li_i).

The higher resistivity and low mobility were observed in 3% Li monodoped ZnO film due to the fact that the mobility was low because p-type dopant preferred to localize at deep level of acceptor. In addition, the energy band structure of single doped ZnO was higher than that of the codoped one [51]. At 3-3% (Al-Li) codoped ZnO due to the hole carrier density was reduced to more than 50% compared to 3%

TABLE 3: General electrical properties measured from Li-doped and Li-Al codoped ZnO samples.

Sample detail	Resistance (Ohm)	Resistivity (Ohm·cm)	Mobility (cm²/Vs)	Carrier density (cm⁻³)	Sheet resistance (Ohm/cm²)	Type of carriers
3% Li-doped ZnO	15.07	15.06	0.918	$4.52E + 17$	$3.18E + 03$	Holes
1.5–3% Al-Li-doped ZnO	9.60	9.59	9.51	$6.85E + 16$	$2.95E + 01$	Holes
3-3% Al-Li-doped ZnO	19.05	19.05	1.54	$2.13E + 17$	$3.11E + 03$	Holes
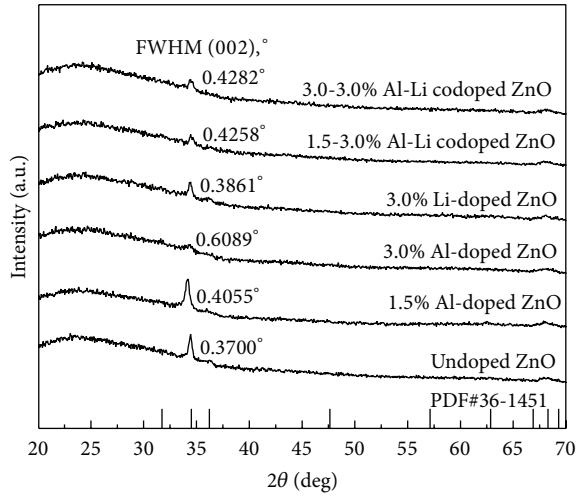
(a)
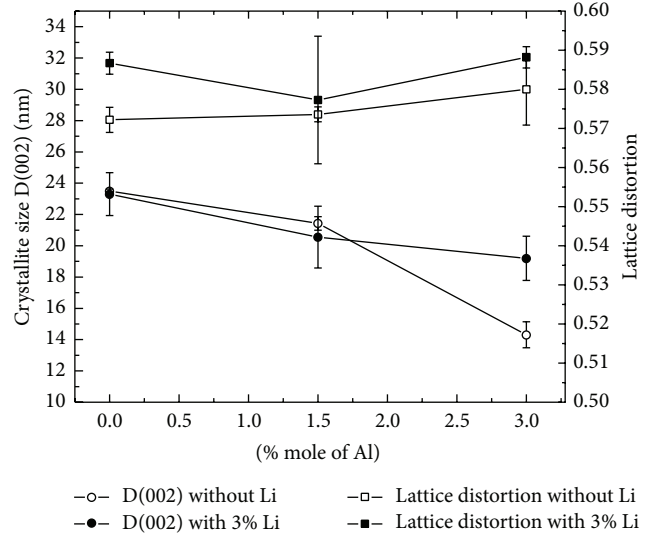
(b)

FIGURE 9: XRD patterns of ZnO with the summarized crystallite information from Rietveld refinements.
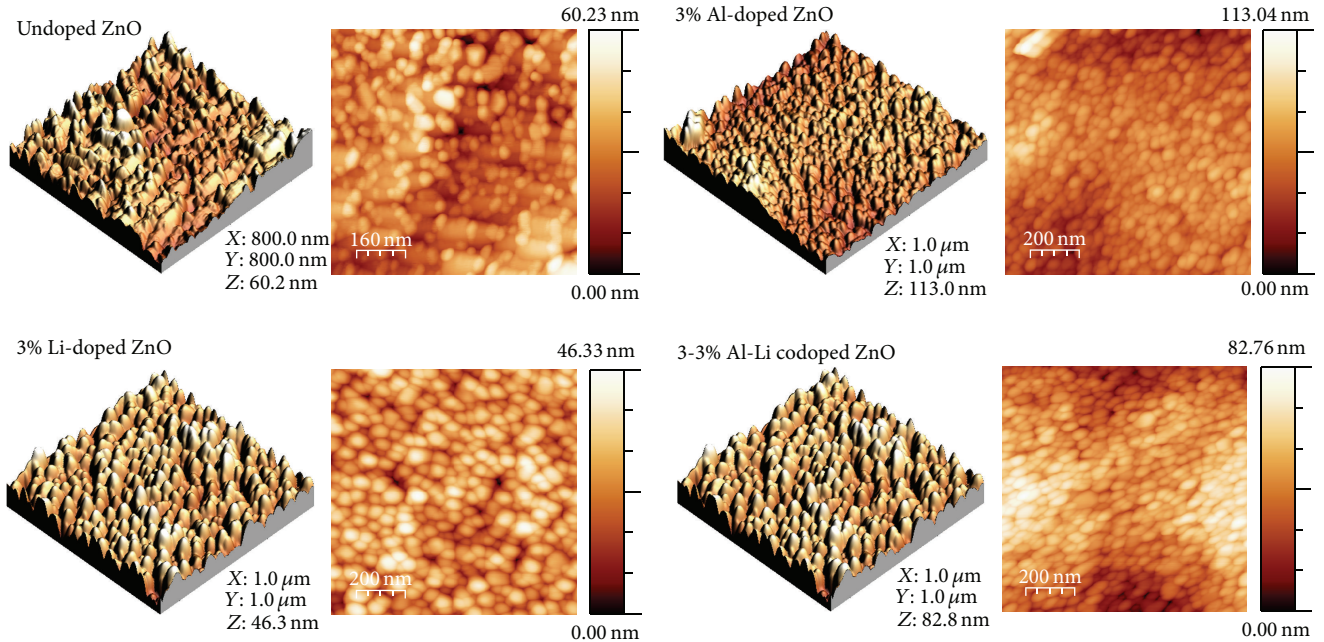
FIGURE 10: AFM images of ZnO-based TCO.

Li-doped ZnO. Al doping at high concentration could form substitute defect (Al_{Zn}) and induce the population of intrinsic defect (Zn_i), which was in agreement with lattice distortion studies in Figure 9. Consequently, the higher resistivity p-type ZnO film could be found.

4. Emerging Applications of Classical p-Type TCOs

As mentioned above, the versatile nature of electrohydrodynamic processing could open new doors for new materials
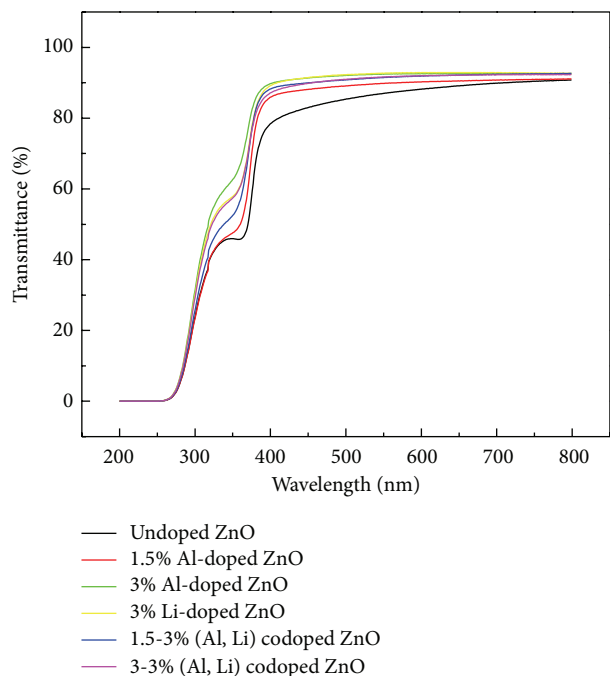
FIGURE 11: Transmittance spectra and the optical properties of ZnO films on glass substrates.
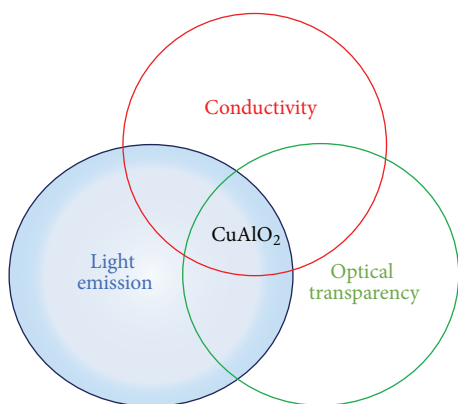
FIGURE 12: Proposed CuAlO$_2$ nanostructured materials integrating three important functionalities.

with innovative morphologies and tailored properties. In the case of CuAlO$_2$ study, which is basically inspired by urgent TCO development, we proposed a potential scheme of multifunctional nanobuilding blocks (Figure 12) which may pose future implications for emerging applications in the area of optoelectronics, thermoelectrics, catalyst, and nanophosphors.

Besides the investigation of near-band-edge emission, given the anisotropic electronic structure and higher conductivity along the basal plane, this delafossite material might be reviewed as a potential host material for luminescence applications. The large trivalent site in this structure is highly tunable and any modification on the trivalent site will unlikely degrade the overall p-type conductivity due to the strong confinement in this superlattice-resembled structure.
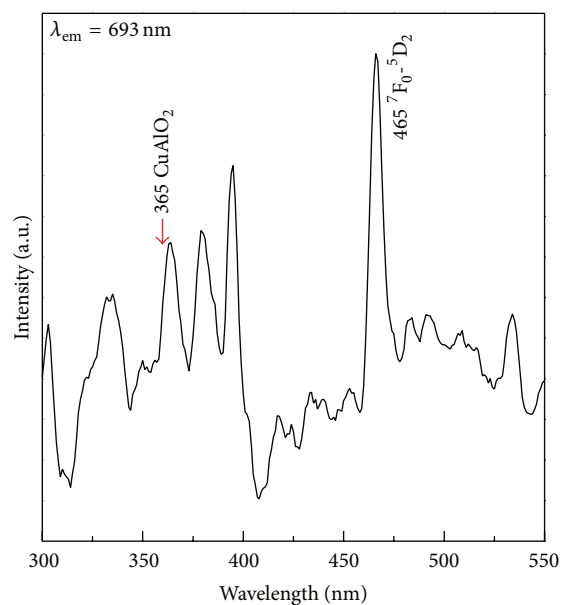
(a)
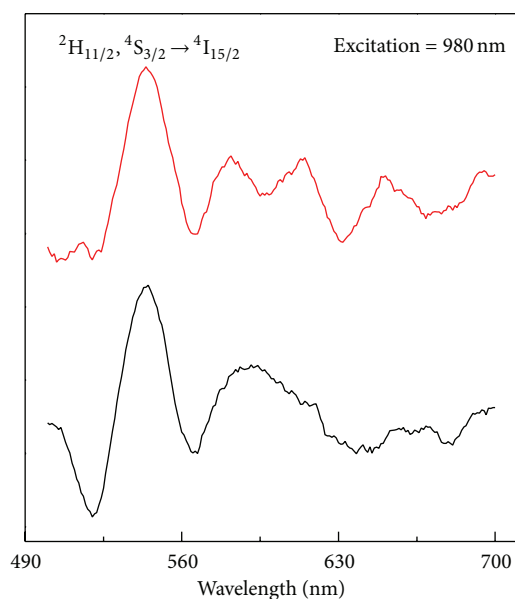
(b)

FIGURE 13: Photoluminescence spectra of CuAlO$_2$ as host materials: (a) doped with Eu^{3+}; (b) doped with Er^{3+} and Yb^{3+}.

Figure 13 shows the characteristic photoluminescence from Ln^{3+} color centers. It could be seen that CuAlO$_2$ indeed could act as an effective host material providing trivalent occupancy and it exhibited the capability of both downconversion and upconversion.

The intercalation of trivalent dopants was further examined by XPS as shown in Figure 14. The binding energies for Cu 2p$_{3/2}$ are centered at ~933.4 eV with no shift observed with respect to Eu doping. It has been widely acknowledged that in the delafossite structure the strong two-dimensional
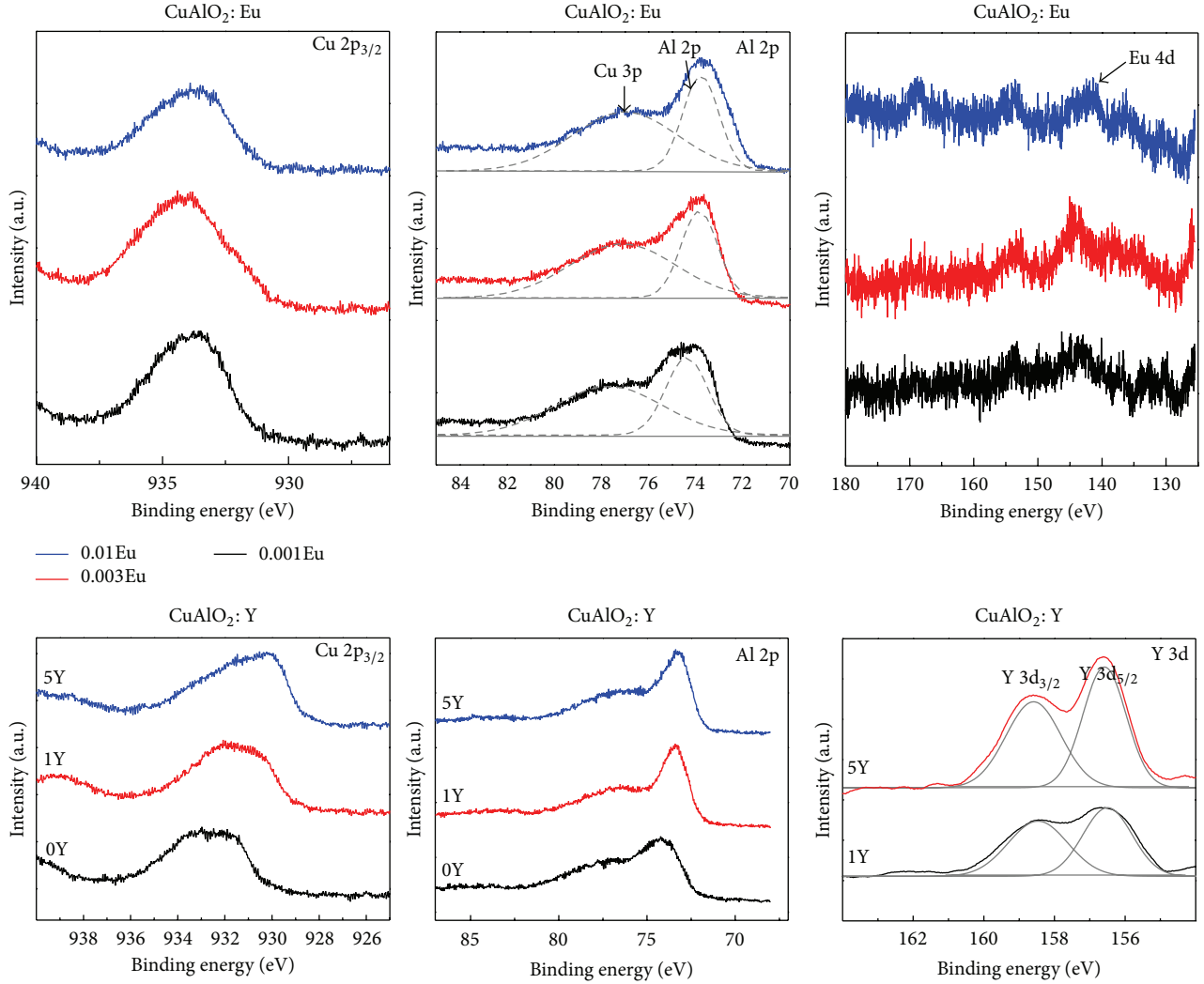
FIGURE 14: XPS core-level spectra of different sites in CuAlO$_2$ hosts with different trivalent substitution.

confinement of Cu-O bonds along z-axis restrains the electronic structure [53]. In contrast to Cu 2p$_{3/2}$ peaks, Al 2p peaks shift to lower binding energies at higher dopant concentrations (74.52 eV for $x = 0.001$, 74.09 eV for $x = 0.003$, and 73.54 eV for $x = 0.01$) due to the environment change around MO$_6$ octahedra along the ab plane. The different Cu 2p$_{3/2}$ and Al 2p BE responses to trivalent ion substitution lead to the conjecture that the introduced rare earth within MO$_2$ layer would insignificantly disturb the hole conduction path in Cu$^+$ layer. Therefore, the p-type conductivity might not be impaired. However, when examining the yttrium doping in the delafossite host, both Cu and Al peaks shifted to lower binding energies, indicating an overall weakening of binding environment after introducing yttrium ions. Our study [24] on the reduced mass of Y doped samples also confirms the observation from XPS.

Due to the strong Cu-O dumbbell bond and the large RE ion radii, it is unlikely that the trivalent RE ions will occupy interstitial sites in the delafossite. On the other hand, a supplemental site occupancy of trivalent ions onto pristine Al site in CuMO$_2$ delafossite could be revealed from the change of lattice parameters in terms of trivalent ionic radius [54]. The lattice constant increases pseudolinearly with the increase of M site ion radius, while the constant c is independent of M site ion radius and should remain constant. Taking the case of Eu doping as an example, according to our host material, CuAlO$_2$, the lattice constant could be estimated by $a = 2.784 \times r_R + 1.437$, in which the constant 2.784 was calculated from the a value at zero doping level from the standard powder diffraction file (PDF#35-1401). The trivalent ion radius r_R follows a weighted sum of both Al^{3+} radius and Eu^{3+} radius ($r_R = (1 - x)r_{Al} + xr_{Eu}$) [55]. The calculated value is shown as a dashed line in Figure 15 and the experimental data is extracted from the Rietveld refinement of the delafossite phase CuAl$_{1-x}$Eu$_x$O$_2$. The correlation between lattice constants and trivalent ionic radii generally follows the calculated rules, indicating the occupancy of extrinsic trivalent ions on the Al sites.

$$a = 2.784 \times r_R + 1.437$$
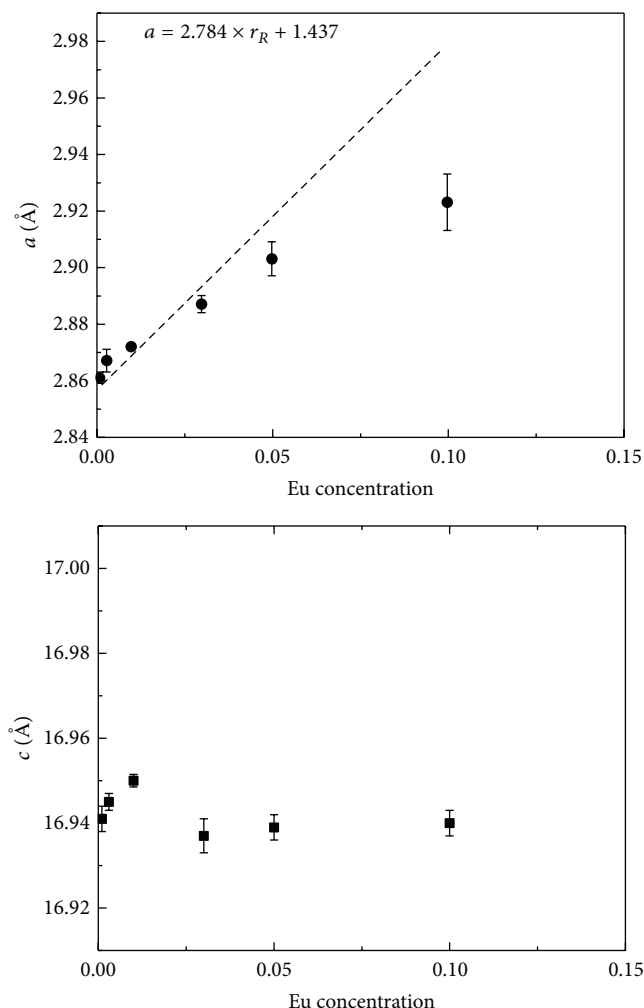
FIGURE 15: The lattice parameters of a and c of the 3R-polytype structure delafossite $CuAl_{1-x}Eu_xO_2$ as a function of Eu concentration. The dash line shows the respective calculated a values.

5. Conclusion

We have shown two case studies on p-type $CuAlO_2$ and ZnO, respectively, due to the high demand for developing p-type oxides with enhanced properties. Electrohydrodynamic processing is capable of fabricating both oxides with fine microstructures and comparable properties. The major advantages of employing electrospray and electrospinning are the low cost and versatility in materials selection and microstructure control. For the case of $CuAlO_2$, electrospray through polyacrylamide route is feasible in obtaining highly crystallized TCO thin films at a lower temperature, while $CuAlO_2$ electrospun fibers with improved visible transmittance could be fabricated in a similar way, yet in completely different morphologies. For ZnO, even though there have been some reports on electrohydrodynamic processing, we testified the feasibility of codoping and observed a simultaneous improvement in surface smoothness and conductivity. The compensated Li exhibited the efficacy to mitigate the deficiencies introduced by degenerate doping. We believe that

the electrohydrodynamic processing would be applied on a broader basis and would be beneficial to next-generation multifunctional materials.

Conflict of Interests

The authors declare that there is no conflict of interests regarding the publication of this paper.

References

[1] H. Fong, I. Chun, and D. H. Reneker, "Beaded nanofibers formed during electrospinning," *Polymer*, vol. 40, no. 16, pp. 4585–4592, 1999.

[2] A. L. Yarin, S. Koombhongse, and D. H. Reneker, "Taylor cone and jetting from liquid droplets in electrospinning of nanofibers," *Journal of Applied Physics*, vol. 90, no. 9, pp. 4836–4846, 2001.

[3] D. Li and Y. Xia, "Electrospinning of nanofibers: reinventing the wheel?" *Advanced Materials*, vol. 16, no. 14, pp. 1151–1170, 2004.

[4] W. Sigmund, J. Yuh, H. Park et al., "Processing and structure relationships in electrospinning of ceramic fiber systems," *Journal of the American Ceramic Society*, vol. 89, no. 2, pp. 395–407, 2006.

[5] Y. Wu and R. L. Clark, "Electrohydrodynamic atomization: a versatile process for preparing materials for biomedical applications," *Journal of Biomaterials Science, Polymer Edition*, vol. 19, no. 5, pp. 573–601, 2008.

[6] Y. Liu, T. L. Olson, and Y. Wu, "Luminescence and microstructure of Nd doped $Y_2Si_2O_7$ electrospun fibers," *Journal of the American Ceramic Society*, vol. 97, no. 8, pp. 2390–2393, 2014.

[7] H. Wu, L. Hu, M. W. Rowell et al., "Electrospun metal nanofiber webs as high-performance transparent electrode," *Nano Letters*, vol. 10, no. 10, pp. 4242–4248, 2010.

[8] D. Li and Y. Xia, "Direct fabrication of composite and ceramic hollow nanofibers by electrospinning," *Nano Letters*, vol. 4, no. 5, pp. 933–938, 2004.

[9] D. S. Ginley and C. Bright, "Transparent conducting oxides," *MRS Bulletin*, vol. 25, no. 8, pp. 15–18, 2000.

[10] H. Kim, J. S. Horwitz, W. H. Kim, A. J. Mäkinen, Z. H. Kafafi, and D. B. Chrisey, "Doped ZnO thin films as anode materials for organic light-emitting diodes," *Thin Solid Films*, vol. 420-421, pp. 539–543, 2002.

[11] Z. Q. Yao, B. He, L. Zhang et al., "Energy band engineering and controlled p-type conductivity of $CuAlO_2$ thin films by nonisovalent Cu-O alloying," *Applied Physics Letters*, vol. 100, no. 6, Article ID 062102, 2012.

[12] T. Konry and R. S. Marks, "Physico-chemical studies of indium tin oxide-coated fiber optic biosensors," *Thin Solid Films*, vol. 492, no. 1-2, pp. 313–321, 2005.

[13] A. N. Banerjee and K. K. Chattopadhyay, "Recent developments in the emerging field of crystalline p-type transparent conducting oxide thin films," *Progress in Crystal Growth and Characterization of Materials*, vol. 50, no. 1–3, pp. 52–105, 2005.

[14] I. Hamada and H. Katayama-Yoshida, "Energetics of native defects in $CuAlO_2$," *Physica B: Condensed Matter*, vol. 376-377, pp. 808–811, 2006.

[15] G. Thomas, "Materials science: invisible circuits," *Nature*, vol. 389, no. 6654, pp. 907–908, 1997.

[16] F. N. Ishikawa, H.-K. Chang, K. Ryu et al., "Transparent electronics based on transfer printed aligned carbon nanotubes on rigid and flexible substrates," *ACS Nano*, vol. 3, no. 1, pp. 73–79, 2009.

[17] H. Kawazoe, M. Yasukawa, H. Hyodo, M. Kurita, H. Yanagi, and H. Hosono, "P-type electrical conduction in transparent thin films of $CuAlO_2$," *Nature*, vol. 389, no. 6654, pp. 939–942, 1997.

[18] M. S. Lee, T. Y. Kim, and D. Kim, "Anisotropic electrical conductivity of delafossite-type $CuAlO_2$ laminar crystal," *Applied Physics Letters*, vol. 79, no. 13, pp. 2028–2030, 2001.

[19] G. Dong, M. Zhang, W. Lan, P. Dong, and H. Yan, "Structural and physical properties of Mg-doped $CuAlO_2$ thin films," *Vacuum*, vol. 82, no. 11, pp. 1321–1324, 2008.

[20] H. Jiang, X. Wang, X. Zang et al., "Electronic properties of bivalent cations (Be, Mg and Ca) substitution for Al in delafossite $CuAlO_2$ semiconductor by first-principles calculations," *Journal of Alloys and Compounds*, vol. 553, pp. 245–252, 2013.

[21] B.-W. Huang, C.-Y. Wen, G.-W. Lin et al., "Influence of Ca/Al ratio on properties of amorphous/nanocrystalline Cu-Al-Ca-O thin films," *Journal of the American Ceramic Society*, vol. 98, no. 1, pp. 125–129, 2015.

[22] D. O. Scanlon, A. Walsh, B. J. Morgan, G. W. Watson, D. J. Payne, and R. G. Egdell, "Effect of Cr substitution on the electronic structure of $CuAl_{1-x}Cr_xO_2$," *Physical Review B*, vol. 79, no. 3, Article ID 035101, 2009.

[23] S. Zhao, M. Li, X. Liu, and G. Han, "Synthesis of $CuAlO_2$ nanofibrous mats by electrospinning," *Materials Chemistry and Physics*, vol. 116, no. 2-3, pp. 615–618, 2009.

[24] Y. Liu, Y. Huang, H. J. Seo, and Y. Wu, "Blueshift in near-band-edge emission in Y^{3+}-doped $CuAlO_2$ nanofibers," *Optical Materials Express*, vol. 4, no. 12, pp. 2602–2607, 2014.

[25] G. Wang, S. Chu, N. Zhan, Y. Lin, L. Chernyak, and J. Liu, "ZnO homojunction photodiodes based on Sb-doped p-type nanowire array and n-type film for ultraviolet detection," *Applied Physics Letters*, vol. 98, no. 4, Article ID 041107, 2011.

[26] K. Mahmood, R. Munir, H. W. Kang, and H. J. Sung, "An atmospheric pressure-based electrospraying route to fabricate the multi-applications bilayer (AZO/ITO) TCO films," *RSC Advances*, vol. 3, no. 48, pp. 25741–25751, 2013.

[27] B. Liu, K. Nakata, M. Sakai et al., "Mesoporous TiO_2 core-shell spheres composed of nanocrystals with exposed high-energy facets: facile synthesis and formation mechanism," *Langmuir*, vol. 27, no. 13, pp. 8500–8508, 2011.

[28] D. Li and Y. Xia, "Fabrication of titania nanofibers by electrospinning," *Nano Letters*, vol. 3, no. 4, pp. 555–560, 2003.

[29] Z. Liu, D. D. Sun, P. Guo, and J. O. Leckie, "An efficient bicomponent TiO_2/SnO_2 nanofiber photocatalyst fabricated by electrospinning with a side-by-side dual spinneret method," *Nano Letters*, vol. 7, no. 4, pp. 1081–1085, 2007.

[30] Z. Zhang, C. Shao, X. Li et al., "Electrospun nanofibers of ZnO-SnO_2 heterojunction with high photocatalytic activity," *The Journal of Physical Chemistry C*, vol. 114, no. 17, pp. 7920–7925, 2010.

[31] Y. Ding, Y. Wang, L. Zhang, H. Zhang, and Y. Lei, "Preparation, characterization and application of novel conductive NiO-CdO nanofibers with dislocation feature," *Journal of Materials Chemistry*, vol. 22, no. 3, pp. 980–986, 2012.

[32] O. Wilhelm, S. E. Pratsinis, D. Perednis, and L. J. Gauckler, "Electrospray and pressurized spray deposition of yttria-stabilized zirconia films," *Thin Solid Films*, vol. 479, no. 1-2, pp. 121–129, 2005.

[33] A.-M. Azad, "Fabrication of yttria-stabilized zirconia nanofibers by electrospinning," *Materials Letters*, vol. 60, no. 1, pp. 67–72, 2006.

[34] Y. Matsushima, T. Yamazaki, K. Maeda, and T. Suzuki, "Fabrication of SnO_2 particle-layers using the electrospray method and gas sensing properties for H_2," *Journal of Electroceramics*, vol. 13, no. 1–3, pp. 765–770, 2004.

[35] A. Hosseinmardi, N. Shojaee, M. Keyanpour-Rad, and T. Ebadzadeh, "A study on the photoluminescence properties of electrospray deposited amorphous and crystalline nanostructured ZnO thin films," *Ceramics International*, vol. 38, no. 3, pp. 1975–1980, 2012.

[36] A. M. Bazargan, S. M. A. Fateminia, M. E. Ganji, and M. A. Bahrevar, "Electrospinning preparation and characterization of cadmium oxide nanofibers," *Chemical Engineering Journal*, vol. 155, no. 1-2, pp. 523–527, 2009.

[37] X. Yang, C. Shao, Y. Liu, R. Mu, and H. Guan, "Nanofibers of CeO_2 via an electrospinning technique," *Thin Solid Films*, vol. 478, no. 1-2, pp. 228–231, 2005.

[38] G. Larsen, R. Velarde-Ortiz, K. Minchow, A. Barrero, and I. G. Loscertales, "A method for making inorganic and hybrid (organic/inorganic) fibers and vesicles with diameters in the submicrometer and micrometer range via sol-gel chemistry and electrically forced liquid jets," *Journal of the American Chemical Society*, vol. 125, no. 5, pp. 1154–1155, 2003.

[39] J. Zhao, W. Zhang, E. Xie, Z. Ma, A. Zhao, and Z. Liu, "Structure and photoluminescence of β-Ga_2O_3:Eu^{3+} nanofibers prepared by electrospinning," *Applied Surface Science*, vol. 257, no. 11, pp. 4968–4972, 2011.

[40] Y. Mizuno, E. Hosono, T. Saito et al., "Electrospinning synthesis of wire-structured $LiCoO_2$ for electrode materials of high-power Li-ion batteries," *The Journal of Physical Chemistry C*, vol. 116, no. 19, pp. 10774–10780, 2012.

[41] C. Shao, H. Guan, Y. Liu, and R. Mu, "MgO nanofibres via an electrospinning technique," *Journal of Materials Science*, vol. 41, no. 12, pp. 3821–3824, 2006.

[42] K. R. Murali and M. Balasubramanian, "Properties of $CuAlO_2$ thin films deposited by polyacrylamide gel route," *Materials Science in Semiconductor Processing*, vol. 16, no. 1, pp. 38–42, 2013.

[43] K. T. Jacob and C. B. Alcock, "Thermodynamics of $CuAlO_2$ and $CuAl_2O_4$ and phase equilibria in the system Cu_2O–CuO–Al_2O_3," *Journal of the American Ceramic Society*, vol. 58, no. 5-6, pp. 192–195, 1975.

[44] R.-S. Yu, S.-C. Liang, C.-J. Lu, D.-C. Tasi, and F.-S. Shieu, "Characterization and optoelectronic properties of p-type N-doped $CuAlO_2$ films," *Applied Physics Letters*, vol. 90, no. 19, Article ID 191117, 2007.

[45] D. O. Scanlon and G. W. Watson, "Conductivity limits in $CuAlO_2$ from screened-hybrid density functional theory," *The Journal of Physical Chemistry Letters*, vol. 1, no. 21, pp. 3195–3199, 2010.

[46] N. Tsuboi, T. Hoshino, H. Ohara et al., "Control of luminescence and conductivity of delafossite-type $CuYO_2$ by substitution of rare earth cation (Eu, Tb) and/or Ca cation for Y cation," *Journal of Physics and Chemistry of Solids*, vol. 66, no. 11, pp. 2134–2138, 2005.

[47] W. Bu, Z. Hua, H. Chen, and J. Shi, "Epitaxial synthesis of uniform cerium phosphate one-dimensional nanocable heterostructures with improved luminescence," *The Journal of Physical Chemistry B*, vol. 109, no. 30, pp. 14461–14464, 2005.

[48] G. Jia, Y. Zheng, K. Liu, Y. Song, H. You, and H. Zhang, "Facile surfactant- and template-free synthesis and luminescent properties of one-dimensional Lu_2O_3:Eu^{3+} phosphors," *The Journal of Physical Chemistry C*, vol. 113, no. 1, pp. 153–158, 2009.

[49] J. Yang, C. Li, Z. Cheng et al., "Size-tailored synthesis and luminescent properties of one-dimensional Gd_2O_3:Eu^{3+} nanorods and microrods," *Journal of Physical Chemistry C*, vol. 111, no. 49, pp. 18148–18154, 2007.

[50] S.-Y. Kuo, W.-C. Chen, F.-I. Lai et al., "Effects of doping concentration and annealing temperature on properties of highly-oriented Al-doped ZnO films," *Journal of Crystal Growth*, vol. 287, no. 1, pp. 78–84, 2006.

[51] T. Yamamoto, "Codoping method for solutions of doping problems in wide-band-gap semiconductors," *Physica Status Solidi (A)*, vol. 193, no. 3, pp. 423–433, 2002.

[52] T. Yamamoto and H. Katayama-Yoshida, "Physics and control of valence states in ZnO by codoping method," *Physica B: Condensed Matter*, vol. 302-303, pp. 155–162, 2001.

[53] A. Narayan Banerjee, S. W. Joo, and B.-K. Min, "Quantum size effect in the photoluminescence properties of p-type semiconducting transparent $CuAlO_2$ nanoparticles," *Journal of Applied Physics*, vol. 112, no. 11, Article ID 114329, 2012.

[54] K. Isawa, Y. Yaegashi, M. Komatsu et al., "Synthesis of delafossite-derived phases, $RCuO_{2+\delta}$ with $R = Y$, La, Pr, Nd, Sm, and Eu, and observation of spin-gap-like behavior," *Physical Review B*, vol. 56, no. 6, pp. 3457–3466, 1997.

[55] M. K. Chong, K. Pita, and C. H. Kam, "Photoluminescence of sol–gel-derived Y_2O_3:Eu^{3+} thin-film phosphors with Mg^{2+} and Al^{3+} co-doping," *Applied Physics A*, vol. 79, no. 3, pp. 433–437, 2004.

Research Article

The Role of Edge Dislocations on the Red Luminescence of ZnO Films Deposited by RF-Sputtering

Rocío Félix,[1,2] Marco Peres,[3,4,5] Sergio Magalhães,[5] Maria Rosario Correia,[3] Armando Lourenço,[4] Teresa Monteiro,[3] Rafael García,[1,2] and Francisco M. Morales[1,2]

[1]*Department of Materials Science and Metallurgical Engineering and Inorganic Chemistry, University of Cádiz, Puerto Real, 11510 Cádiz, Spain*

[2]*Institute of Research on Electron Microscopy and Materials of the University of Cádiz (IMEYMAT), Puerto Real, 11510 Cádiz, Spain*

[3]*Department of Physic and I3N, University of Aveiro, Campus of Santiago, 3810-193 Aveiro, Portugal*

[4]*Department of Physics, CICECO, University of Aveiro, 3810-193 Aveiro, Portugal*

[5]*Instituto Superior Técnico (IST), Campus Tecnológico e Nuclear, Estrada Nacional 10, Bobadela, 2695-066 Loures, Portugal*

Correspondence should be addressed to Rocío Félix; rocio.felix@uca.es

The existence of extended defects (i.e., dislocations) in inorganic semiconductors, such as GaN or ZnO, responsible for broad emission peaks in photoluminescence analysis remains unresolved. The possible assignments of these luminescence bands are still matter of discussion. In this study, two different zinc oxide samples, grown under different oxygen partial pressures and substrate temperatures, are presented. Epitaxial and structural properties were analysed by means of X-ray diffraction and transmission electron microscopy techniques. They confirm that the layers are single-phase with a good crystalline quality. Nevertheless, a different density of threading dislocations, with a higher contribution of edge dislocations, was found. Photoluminescence spectroscopy has been used to investigate the optical properties. The steady state luminescence spectra performed at 14 K evidenced the donor bound exciton recombination and deep green and red emission bands. The red band with a maximum at 1.78 eV was found to be stronger in the sample grown at lower oxygen pressure which also shows higher density of threading dislocations. From the temperature and excitation density dependence of the red band, a donor acceptor pair recombination model was proposed, where hydrogen and zinc vacancies are strong candidates for the donor and acceptor species, respectively.

1. Introduction

Nowadays ZnO is among other semiconductors, one of the most studied materials, due to the potentialities offered by its wide direct band gap (3.37 eV) at room temperature and high (~60 meV) free exciton binding energy [1, 2]. These characteristics together with the easiness of depositing thin ZnO films by different techniques with a considerable quality make this material a suitable semiconductor for a broad range of applications in optical and electrical devices (light emitting diodes, transparent thin film transistors, and surface acoustic wave systems [2–6]). Despite the increasing interest in this material, a deeper understanding of the role of the structural defects in the oxide host is still necessary, for

example, to overcome the difficulties in obtaining p-type conductivity, among others. For instance, line defects, and more specifically threading dislocations (TDs), are known to have effects on photonic and electronic materials behaviours [7, 8] causing a degradation in the semiconductor device. For example, TDs produce undesirable phenomena that lead to the appearance of additional electronic energy levels in the band gap influencing the semiconductor electrical and optical properties [8].

From the luminescence point of view, it is well established that the recombination processes on high quality ZnO layers occur nearby the band gap with the emission due to free and donor bound excitons [9]. Additionally, surface excitons and stacking faults related luminescence effects have also been
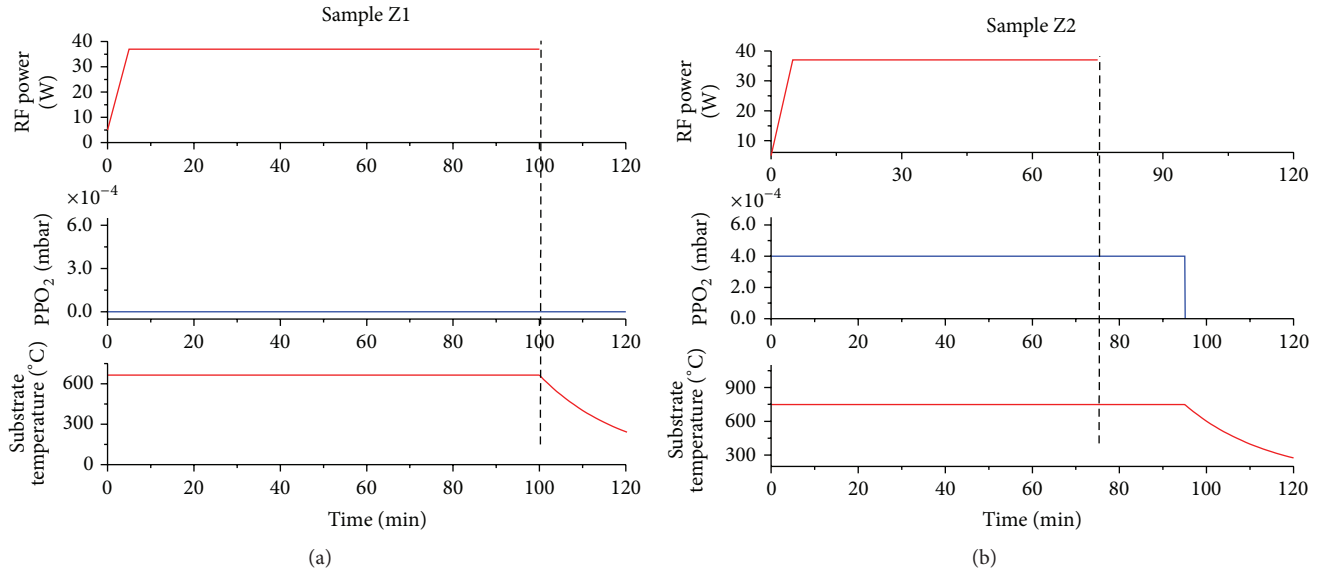
FIGURE 1: Deposition parameters profiles (substrate temperature, O_2 partial pressure (PPO$_2$), and RF power) of sample Z1 (a) and sample Z2 (b).

reported [10–12]. On the lower energy side, the luminescence has been attributed to donor acceptor pairs (DAP) and recombination's broad bands to often unknown origin [13]. The latter can occur in distinct spectral regions and have been observed in the blue, green, orange, and red spectral regions, when the samples are excited with photons with energy higher than the band gap [2, 14]. Based on the luminescence behaviour with time, temperature, and excitation density, several models have been proposed for the emitting centres including impurity related [15–18], DAP [2, 13, 19], free-to-bound transitions [14, 20, 21] and potential fluctuations [20, 22]. The observation of the different broad bands is shown to be sample dependent and their assignment to point or structural defects are still under debate.

In this work, ZnO thin films were deposited by radio-frequency- (RF-) sputtering on [0001] c-Al$_2$O$_3$ for different growth parameters. The samples were characterized by diffraction-contrast two-beam transmission electron microscopy (DC-2B-TEM). Additionally, electron and X-ray diffraction (XRD), plus photoluminescence (PL), were used in order to check correlations of structural and optical properties. The emphasis was placed on the red emission band with a maximum at 1.78 eV which was found to be stronger in samples with higher density of TDs. A correlation between the red luminescence band and the highest TD density is discussed in the context of this paper.

2. Experimental

Two zinc oxide film samples (Z1 and Z2) were deposited by RF-sputtering on c-sapphire substrate using the same RF power.

Sample Z1 was deposited in the absence of oxygen and sample Z2 with an oxygen partial pressure of 4.0×10^{-4} mbar.

The Z1 and Z2 samples were grown at $664°C$ and $746°C$, respectively. These growth parameters profiles are shown in Figure 1. The distance from the target to the substrate was maintained constant and for the deposition processes a commercial ZnO target with a 99.9% purity was used.

Structural and optical studies were performed by transmission electron microscopy (TEM), selected area electron diffraction (SAED), XRD, and PL spectroscopy.

The structure of the samples was characterised by TEM after samples were prepared in cross sections (XTEM) or for plan-view (PVTEM). They were thinned to reach the electron transparency with conventional methods of mechanical grinding and polishing, dimpling (dimple grinder GATAN TM 656), and ion milling (applied with a GATAN low voltage precision ion polish system, PIPS). Bright field (BF) and dark field (DF) DC-2B-TEM micrographs and SAED patterns were collected with a JEOL-1200EX microscope. The TD density for each ZnO layer was calculated as the average value of 8 different areas sizes ranging between 0.5 and 1 μm^2 for PVTEM and 5 different lengths or regions between 0.7 and 3.7 μm for XTEM preparation. The ZnO film thickness and surface roughness were also estimated from the analyses of 10 BF-TEM images, with analysed lengths between 12 and 30 μm depending on the sample.

The XRD measurements were carried out with a Philips XRD X'pert diffractometer with the Cu Kα in out-of-plane configuration for symmetric planes and in skew geometry for asymmetric ones. XRD reciprocal space maps (RSM) were obtained for the symmetric (0002) reflections and ϕ-scans for asymmetric planes (20$\bar{2}$1). The PL studies were carried out using a 325 nm He-Cd laser line as excitation source, and a Spex 1704 monochromator (with a 1200 grooves/mm grating) coupled with a cooled photomultiplier (Hamamatsu R928) was used to disperse and detect the luminescence, respectively. The temperature dependent PL measurements

(a)

(b)
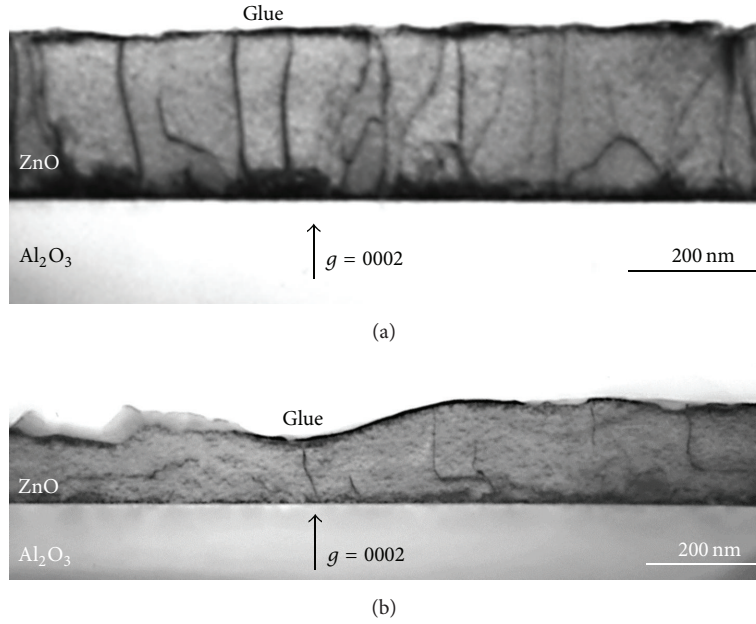
FIGURE 2: DC-2B-BF XTEM images of Z1 (a) and Z2 (b) samples displaying screw + mixed dislocations (they were taken in $[11\bar{2}0]$ zone axis using the (0002) excited reflection).

were acquired in the temperature range between 14 K and room temperature (RT) using a closed-cycle-cryostat. For the excitation intensity dependence commercial calibrated neutral density filters were used. All the PL spectra were corrected to the spectral response of the collection and detection system.

3. Results and Discussion

3.1. Structural Properties. TEM was applied to get information about the structural quality and the presence of defects at the ZnO films. The thickness and surface roughness of the layers were analysed from lengths of 12 μm for sample Z1 and 30 μm for sample Z2 (see Table 1). According to a higher growth deposition time (as present in Figure 1), the ZnO layer in sample Z1 is thicker and less rough.

Concerning TD characterization by TEM, the method used in this work is based on the combination (cross-correlation) of DC-2B-BF TEM images from XTEM and PVTEM preparations [23] which allows obtaining on the one hand edge + mixed and screw + mixed TDs and on the other hand density of TDs at different depths of the ZnO layers.

Images of TDs in DC-2B-TEM conditions were obtained when the samples are oriented taking into account the invisibility criterion $g \cdot b = 0$. Therefore, dislocations become invisible if this criterion is satisfied, where "g" is the excited reflection and "b" is the Burgers vector [24]. Besides, depending on Burgers vector, TDs are classified in three different groups, that is, screw, edge, and mixed, which in the concerned wurtzite system correspond to $b_s = \langle 0001 \rangle$, $b_e = (1/3)\langle 11\bar{2}0 \rangle$, and $b_{e+s} = b_m = (1/3)\langle 11\bar{2}3 \rangle$, respectively.

TABLE 1: Thickness and roughness of ZnO layers for samples Z1 and Z2.

Sample	Thickness (nm)	Roughness (nm)
Z1	322 ± 12	38 ± 12
Z2	195 ± 20	84 ± 20

TABLE 2: Groups of TDs that can be observed in TEM for each preparation and two-beam conditions.

Preparation	Zone axis	Reflection (g)	Type of TDs
PVTEM	[0001]	$(11\bar{2}0)$	Edge and mixed
XTEM	$[11\bar{2}0]$	(0002)	Screw and mixed

Traditionally, dislocations are given in groups (edge + mixed or screw + mixed) because images with only one type of dislocations are not geometrically possible to be obtained. For this reason, in the present work, the TD density data will be given together, that is, screw + mixed and edge + mixed. Table 2 shows the crystallographic direction (zone axis) and the related reflection (g) selected to acquire the TEM images for each preparation, together with the type of TDs that are observed.

The number of TDs is directly measured from DC-2B-BF TEM micrographs (a couple of examples are shown in Figures 2 and 3). Thereupon, as indicated in Table 2, edge + mixed dislocations were calculated by using the $g = (11\bar{2}0)$ excited reflection near the [0001] zone axis of ZnO from PVTEM preparations. Likewise, screw + mixed dislocations were calculated by using the (0002) excited reflection near the $[11\bar{2}0]$ zone axis of ZnO from XTEM.

TABLE 3: TD densities at ZnO surface and annihilation for samples Z1 and Z2.

| Sample | Surface dislocation densities | | Annihilation of screw + mixed TDs (%) |
	Edge + mixed (10^8 cm^{-2})	Screw + mixed (10^8 cm^{-2})	
Z1	84.9 ± 10.3	12.1 ± 0.7	44
Z2	31.7 ± 3.9	4.5 ± 0.3	51

(a)

(b)
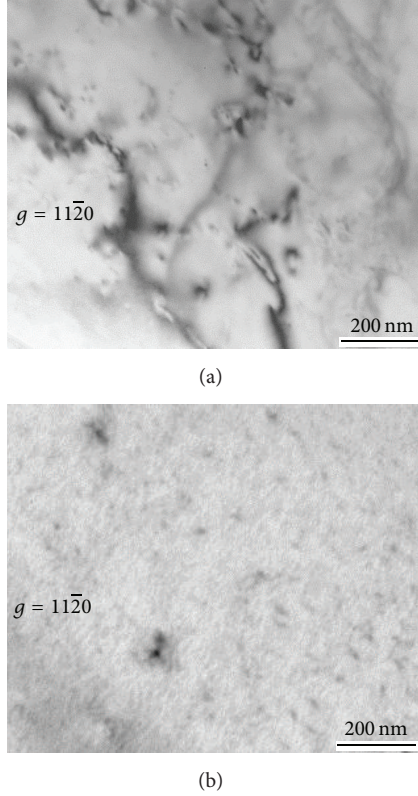
FIGURE 3: PVTEM DC-BF micrographs of Z1 (a) and Z2 (b) samples where edge + mixed dislocations are visible. They were taken using the $g = (11\bar{2}0)$ excited reflection.

FIGURE 4: Density of screw + mixed (s + m) dislocations for Z1 (red) and Z2 (green) samples in dependence on the distance from sapphire/ZnO interface. The densities of TDs were measured at different height rate (20%, 50%, and 70%) of the ZnO layer, where 0% belongs to sapphire/ZnO interface and 100% refers to ZnO surface.

Since it is well known that TD density values measured from PVTEM preparations are more accurate than those estimated from XTEM [25], the screw + mixed TD density on the ZnO surface has been determined through the edge + mixed TD density. In order to do that, we have relied on previously reported results [26, 27] that claim that edge + mixed dislocations are about 80–90% of the whole, while screw + mixed dislocations range between 10 and 20 per cent. Consequently, the edge + mixed TD density (directly calculated from the PVTEM preparation) is assumed as 85% of the whole, whereas the remaining percentage belongs to the screw + mixed TD density. The thickness of each XTEM preparation is evaluated by equalling the screw + mixed TD density directly measured value at the ZnO surface, to that calculated from the PVTEM. Once the thickness is determined, the density of TDs propagating from the sapphire/ZnO interface towards the ZnO surface (TD density

evolution) can be evaluated, and therefore the annihilation rate can be estimated (see Table 3 and Figure 4). Additionally, data of TD density at ZnO surface obtained by using the aforementioned method are shown in Table 3. The errors in this table were calculated through the minimum square method (for the directly measured densities) and the well-known statistical formula for mean value errors.

Evaluating the TEM results, it is found that sample Z1 has a higher TD density than sample Z2 (Table 3). This can be also seen in Figure 2, where pictures for Z1 and Z2 samples have the same scale marker and a higher number of screw + mixed TDs are predicted for sample Z1 at first glance. Besides, it has been evidenced from Figures 2 and 3 that the main structural defects observed in the ZnO layers correspond to TDs (screw + mixed and edge + mixed) with densities ranging from 10^8 to 10^9 cm^{-2} from the interface to the surface (Table 3). These values have a good agreement with previously reported results on good quality state of the art ZnO layers [3, 28–30]. For the analysed samples no stacking faults were identified

(a)

(b)

(c)

(d)
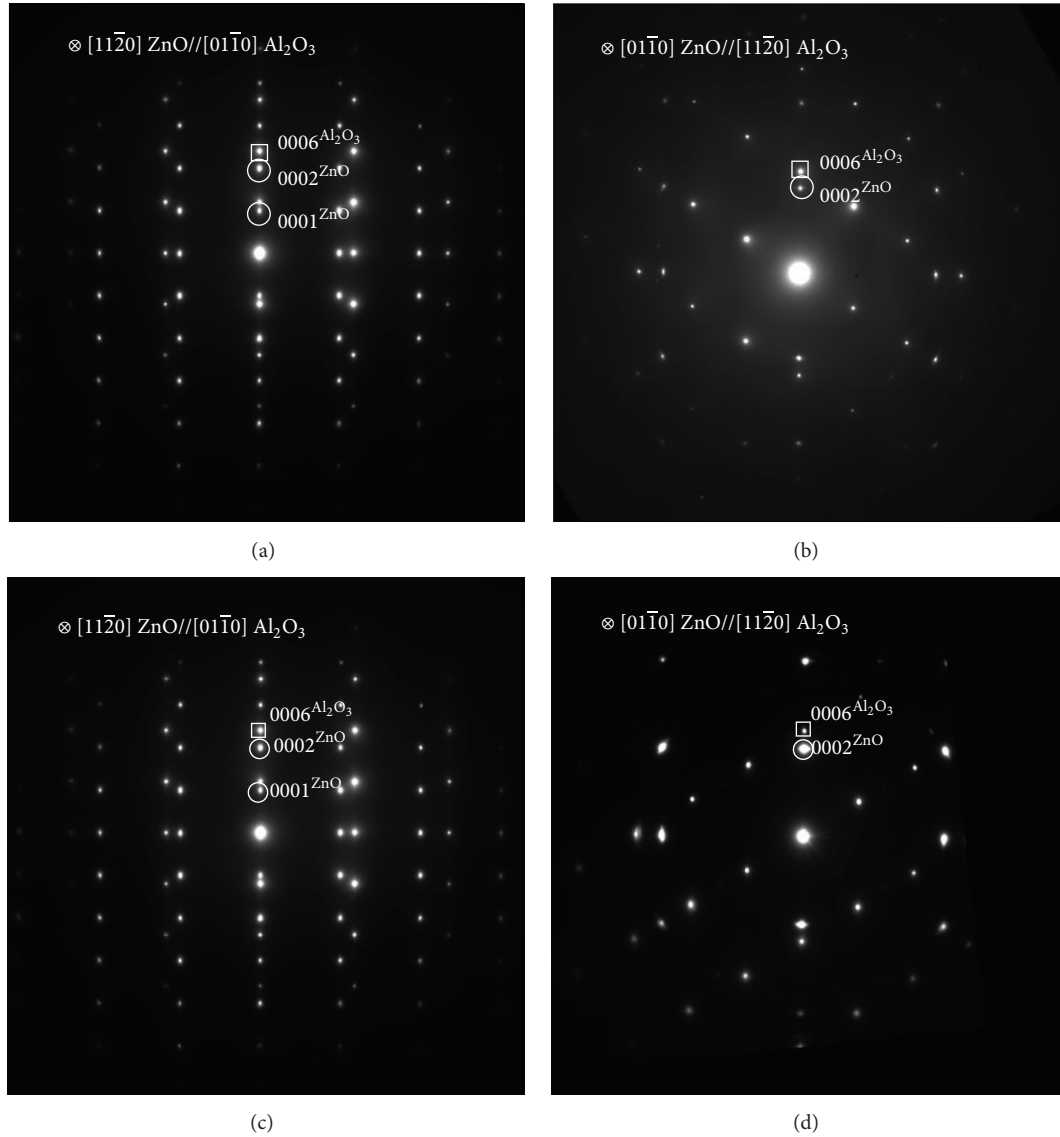
FIGURE 5: SAED patterns of the complete heterostructure in XTEM preparations. (a) and (b) SAED patterns in $[11\bar{2}0]$ and $[01\bar{1}0]$ zone axis of ZnO layers, respectively, for sample Z1. (c) and (d) SAED patterns in $[11\bar{2}0]$ and $[01\bar{1}0]$ zone axis of ZnO layers, respectively, for sample Z2.

and the TD density was found to be dependent on the depth inside the film. Attending to the screw + mixed annihilations, the results reveal that about 44% for sample Z1 and 51% in the case of sample Z2 annihilate when they reach the ZnO surface.

SAED patterns for XTEM preparations were also recorded giving indications of the good single-crystallinity of ZnO in regions around the Al_2O_3 and ZnO interface and at ZnO surface and of its heteroepitaxial placement on the whole heterostructure. Figure 5 shows well-defined characteristic reflections of ZnO wurtzite and α-Al_2O_3. Therefore, the following heteroepitaxial relationships can be concluded: $[11\bar{2}0]ZnO//[01\bar{1}0]\gamma$-$Al_2O_3$ and $[01\bar{1}0]ZnO//[11\bar{2}0]\gamma$-$Al_2O_3$.

Figure 6 shows the 2 theta-omega (2θ-ω) scans for Z1 and Z2 samples. The data indicate that only one diffraction maximum attributed to the (0002) ZnO reflection is observed for the investigated layers. This result specifies that the crystallites grow preponderantly oriented with the c-axis normal to the substrate. To evaluate the samples structural quality, the RSM for the reflection (0002) were carried out as shown in Figure 7. The shape and broadening of the symmetric RSM are very similar for both samples, indicating that the type of defects should be similar. The broadening can be accounted by stoichiometry/strain gradients, tilt, and the limited size [31]. In the investigated layers the stoichiometry/strain gradients should be one of the major effects on the broadening, as suggested by the TEM measurements. We also
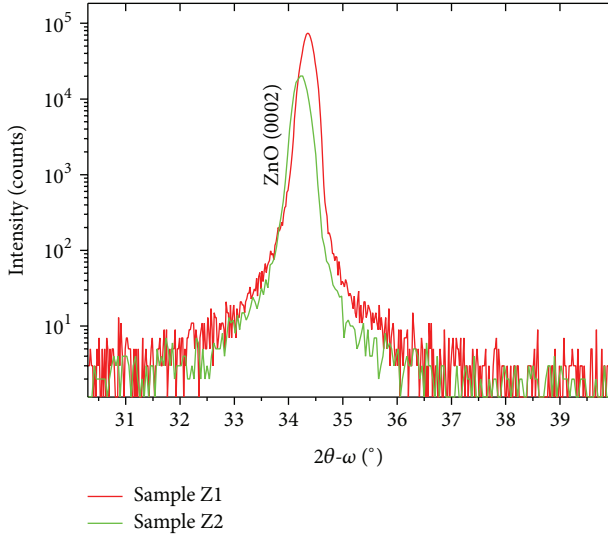
FIGURE 6: XRD 2 theta-omega scans for the reflection (0002) obtained in out-of-plane geometry for Z1 (red) and Z2 (green) samples.

performed ϕ-scans in order to evaluate the azimuthal rotation of the crystallites by calculating the twist angle, α_{ϕ} [32].

Figure 8 shows the ϕ-scans of the asymmetric $(20\bar{2}1)$ reflection, corresponding to a plane with an inclination angle of $74.83°$ with respect to the [0001] direction. A distinct broadening can be clearly identified for both samples. This result evidences that dissimilar twist angles (estimated as $0.290°$ and $0.109°$, for samples Z1 and Z2, resp.) occur among the crystallites. Assuming that the twisted angle is proportional to the density of the edge dislocations [31, 32], these results suggest that a high density of edge dislocations is present in the sample Z1.

3.2. Optical Properties. Figure 9 shows the 14 K PL spectra of the two ZnO layers obtained with above band gap excitation. On the high energy side, the samples luminescence corresponds to the free (FX), donor bound (D^0X) and surface (SX) excitons, followed by the two-electron satellite lines and LO-phonon replicas of the bound excitons [9, 20, 33–36]. Additionally, a structured green luminescence (~2.4 eV) and an unstructured red band (~1.78 eV) are observed. The LO-phonon-assisted structured green band has been ascribed as a Cu-impurity related defect [37]. Copper impurities are known to be trace contaminants in low purity commercial ZnO targets, as the ones used in this work. Intrinsic defects such as Zn_i, O_i, V_O, V_{Zn}, and their complexes have been reported in the literature as being responsible for the unstructured broad emission bands in ZnO [38, 39]. When the growth conditions are performed under oxygen deficiency, as the case of Z1 sample, V_O and Zn_i are expected to be the main intrinsic point defects. However, first-principles calculations have shown that these defects have a high energy formation; consequently their occurrence is unlikely [40]. According to Janotti and Van de Walle [40] the neutral V_O leads to a deep donor level located at ~1 eV below the conduction band,

V_{Zn} are deep acceptors, and Zn_i are shallow donors. The latter is also known to form unstable defects due to their low energy migration [40]. Nowadays, it has been widely accepted that V_{Zn} (and their aggregates) are the most likely acceptors in ZnO [41–44], introducing energy levels between 1.6 and 2.1 eV below the conduction band [44].

Previous studies have also shown a strong correlation between the screw dislocations and the near band edge PL intensity [45]. Namely, the generated strain fields around screw dislocations leading to heterogeneous spatial distribution of the carriers are known to disturb the density of states reducing the PL recombination efficiency. On the other hand, it has been pointed out that the edge dislocations assume an important role on the deep level emission in semiconductors by trapping point defects and impurities in their strain fields [3, 46].

As can be seen in Figure 9 (in logarithmic scale), besides the already stated transitions, a broad red band of unknown origin was detected in both samples, however, with a stronger emission in sample Z1, which is the sample with the highest estimated value of the TD density (~10^9 cm^{-2}). In order to establish a coherent interpretation of the 1.78 eV emission, band temperature and excitation dependent PL studies were carried out for Z1 sample, presented in Figures 10 and 11.

The evolution of the red band PL intensity with temperature depicted in Figure 10(a) evidences a decrease in the overall intensity when the temperature increases. Furthermore, a shift to lower energy of the band maximum is observed for temperatures above 40 K (Figure 10(b)). By assuming a Gaussian band shape to fit the deep level recombination, the evolution of the integrated intensity of the red band can be established as shown in Figure 10(c). Considering a classical model to describe a single thermally activated nonradiative recombination channel, the evolution of the integrated intensity, $I(T)$, with temperature follows a Mott law according to

$$I(T) = I_0 \left[1 + a \cdot \exp\left(-\frac{E_a}{k_B} \right) \right]^{-1}, \tag{1}$$

where I_0 stands for the low temperature intensity when the nonradiative processes are neglected; a is a temperature independent effective degeneracy, E_a is the activation energy for the nonradiative processes, and k_B is the Boltzmann constant. The best fit is achieved for an activation energy of 14 ± 2 meV.

It should be mentioned that similar broad red bands have been reported in bulk, films, and nanostructures of ZnO and GaN materials [38, 47]. Particularly, Reshchikov et al. [38] found in bulk material of ZnO an emission band (denoted as RL1) with the maximum near the same energy and a thermal quenching described by similar activation energy. However, while in the latter case no shifts of the RL1 band maximum were identified between 14 K and the RT, in our work the red luminescence maximum shifts following the band gap shrinkage (Figure 10(b)). This behaviour suggests that the defect related with the 1.78 eV band should involve electronic energy levels sensitive to the band gap reduction, described by the effective mass theory.
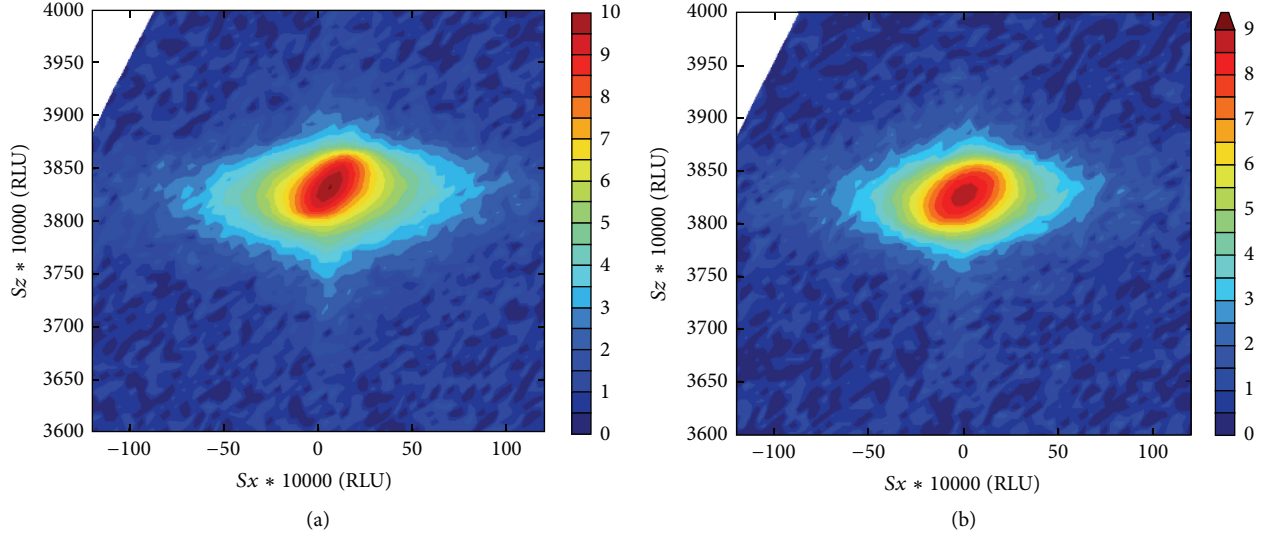
FIGURE 7: RSM of the (0002) symmetric reflections for (a) Z1 and (b) Z2 samples.
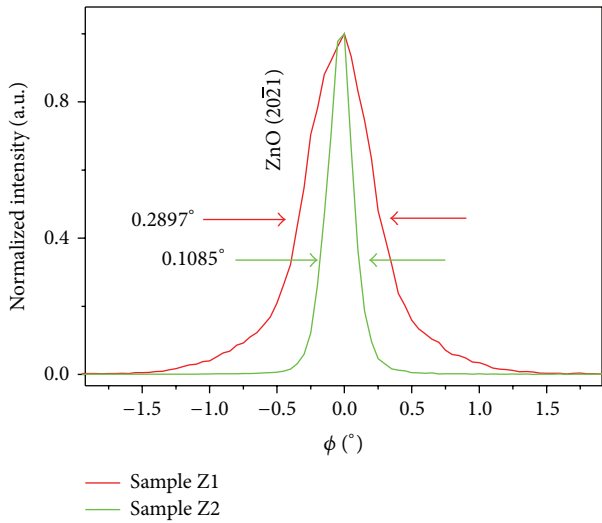
FIGURE 8: ϕ-scans for (20$\bar{2}$1) reflection obtained in skew geometry for samples Z1 (red) and Z2 (green).
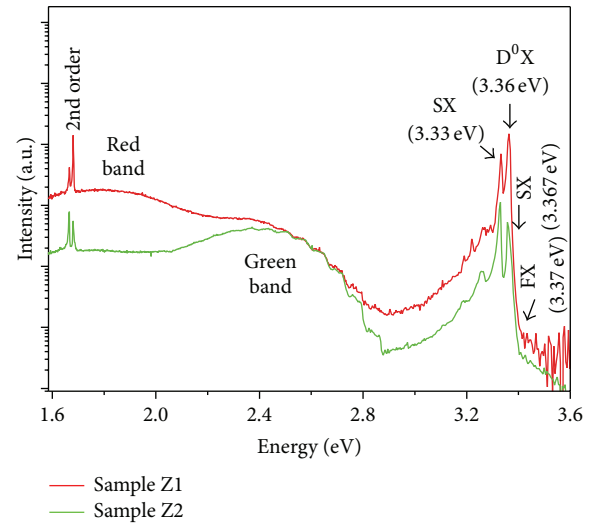
FIGURE 9: The PL spectra of the Z1 (red) and Z2 (green) samples obtained by the He-Cd excitation at 14 K (the spectra are presented in logarithmic scale).

Increasing the excitation density, the measured 14 K PL spectra (Figure 11(a)) promote a high energy shift of the band maximum. This is a common behaviour in DAP transitions due to the saturation of distant pairs, which have low transition probabilities [48]. In our case a ~20 meV shift can be observed among the low and high excitation intensities (Figure 11(b)). An additional indication that the red 1.78 eV band behaves as a DAP transition is provided by the sublinear dependence (Figure 11(c)) of the integrated PL intensity with the excitation intensity ($I_{PL} \alpha I_{exc}^{\beta}$) expected for this type of recombination processes [49]. The emission energy of a DAP (E_{DAP}) with a separation r is given by [48]

$$E_{DAP} = E_g - E_d - E_a + \frac{e^2}{4\pi\varepsilon_0\varepsilon_r r}, \qquad (2)$$

where E_g stands for the band gap energy, E_d and E_a stand for the donor and acceptor binding energies, and the $1/r$ term corresponds to the Coulomb interaction among the ionized species.

Considering that under the low excitation intensity conditions an infinite pair separation is reached, the Coulomb term could be neglected, and an ($E_a + E_d$) ~1.68 eV is estimated by assuming a band gap energy of 3.437 eV at 14 K. If the 14 meV determined from the red band quenching corresponds to the binding energy of an exciton bound to the donor ($E_{b,d}$) by using the Haynes rule derived by Meyer et al. [9] for shallow donors, $E_{b,d} = 0.365E_d - 3.8$ (meV), a donor binding energy of ~49 meV is estimated. This energy value suggests that H participate in DAP [9]. The acceptor

(a)

(b)

(c)
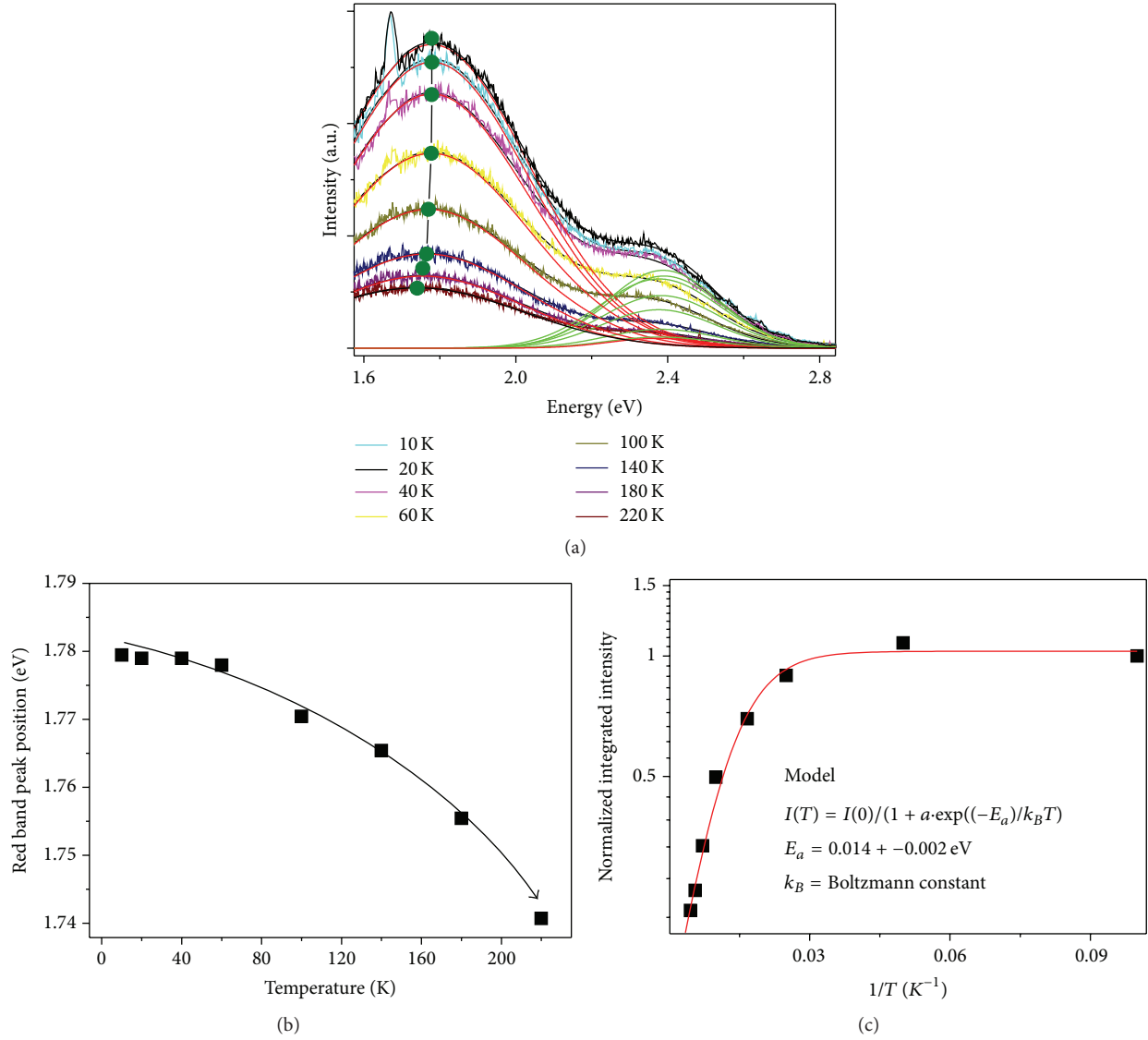
FIGURE 10: Sample Z1. (a) Temperature dependent deep level PL spectra obtained with above band gap excitation, (b) temperature dependence of the red band peak energy, and (c) dependence of the integrated emission intensity with the temperature for the red band.

level should be placed at ~1.75 eV above the valence band, if in agreement with the expected energy level for zinc vacancies [44]. Taking into account the discussion provided on the nature and energy level location of the intrinsic defects referred to above, the red emission band could be associated with a DAP involving the hydrogen shallow donor and zinc vacancies as deep acceptors. Consequently, the stronger intensity of the red emission for sample Z1 (with the higher TD density) suggests that higher amount of point defects could be induced in samples with the highest threading dislocations density.

4. Conclusions

In this work, ZnO films have been deposited on c-Al_2O_3 substrate under presence and absence of oxygen. These

different oxygen pressures have strong effects on the structural and optical properties of ZnO layers. The films are monocrystalline with a highlighted quality. However, the TEM characterization has revealed that the sample grown without oxygen atmosphere presents a higher density of TDs, the majority of them being edge dislocations type. Moreover, it was found that both samples evidence heterogeneity in depth, displaying a decrease of the TD density from the sapphire/ZnO interface to the sample surface. In agreement with the TEM results, the asymmetrical ϕ-scans for $(20\bar{2}1)$ reflection reveal a high value of twist angle for the sample process with null oxygen pressure, indicating high density of edge dislocations. In addition by optical characterization, a green band at ~2.4 eV and a red band at ~1.78 eV are observed. The green structured band is similar to the one previously assigned to the presence of Cu_{Zn} acceptor due to copper impurities likely due to trace contaminants in

(a)

(b)

(c)
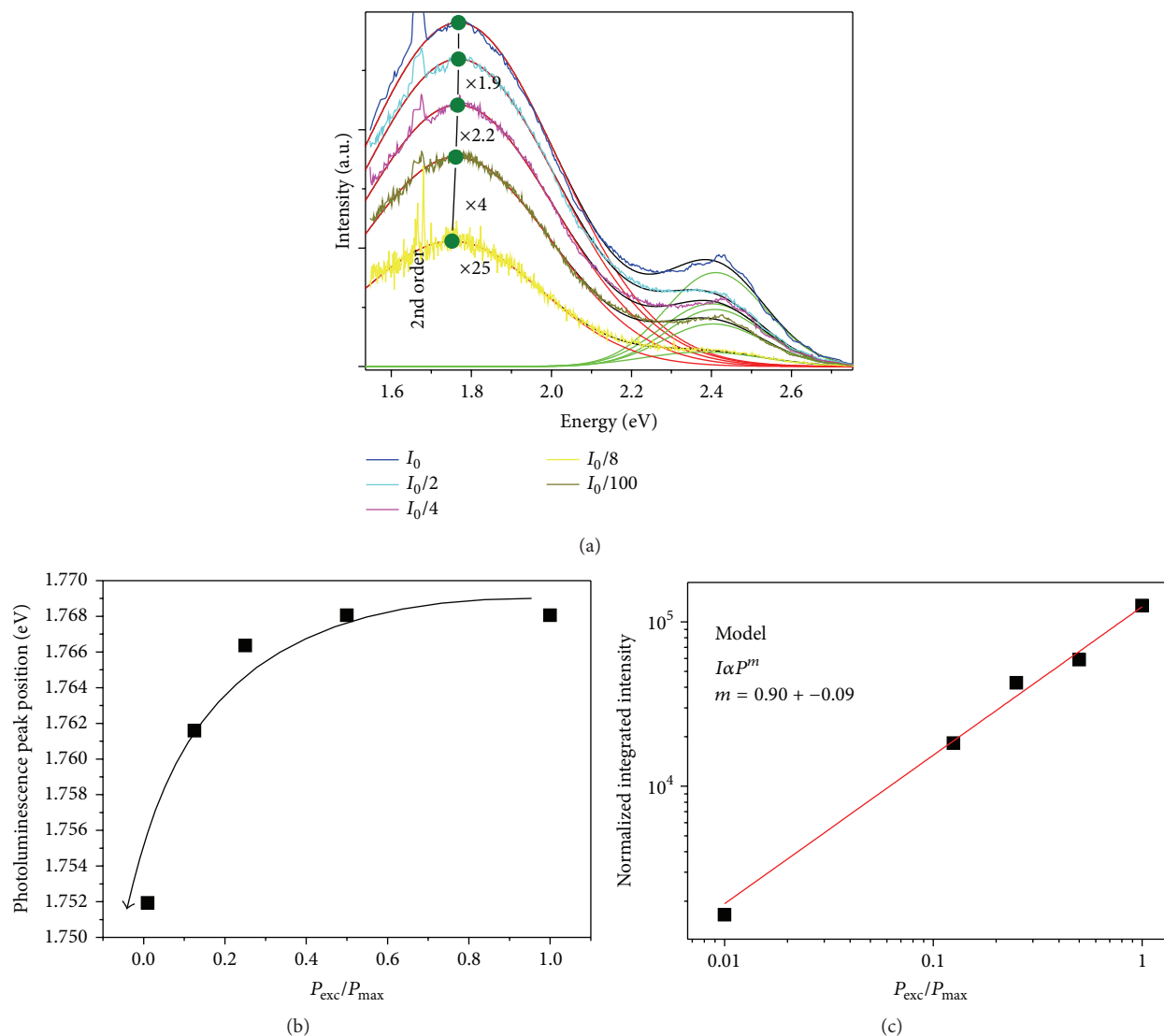
FIGURE 11: Sample Z1. (a) 14 K PL spectra obtained with above band gap excitation by using different excitation intensities, (b) red band peak energy dependence with the excitation intensity, and (c) dependence of the red band integrated intensity with the excitation intensity.

the precursor target. The red luminescence is more pronounced in the sample with the uppermost density of TDs. Hence, this red band has been analysed in detail, in order to find a correlation with the different amount of edge dislocations. From the temperature and excitation dependence of the red band, a donor acceptor pair recombination model has been proposed, where hydrogen and zinc vacancies are strong candidates for the donor and acceptor species, respectively. These results suggest that such optically active point defects are promoted in the sample with higher amount of edge dislocations.

Conflict of Interests

The authors declare that there is no conflict of interests regarding the publication of this paper.

References

[1] Z. K. Tang, G. K. L. Wong, P. Yu et al., "Room-temperature ultraviolet laser emission from self-assembled ZnO microcrystallite thin films," *Applied Physics Letters*, vol. 72, no. 25, pp. 3270–3272, 1998.

[2] U. Ozgur, Y. I. Alivov, C. Liu et al., "A comprehensive review of ZnO materials and devices," *Journal of Applied Physics*, vol. 98, no. 4, Article ID 041301, 2005.

[3] C. Y. Lin, W.-R. Liu, C. S. Chang, C.-H. Hsu, W. F. Hsieh, and F. S.-S. Chien, "Effect of threading dislocations on local contacts in epitaxial ZnO films," *Journal of the Electrochemical Society*, vol. 157, no. 3, pp. H268–H271, 2010.

[4] Z. L. Wang, "Towards self-powered nanosystems: from nanogenerators to nanopiezotronics," *Advanced Functional Materials*, vol. 18, no. 22, pp. 3553–3567, 2008.

[5] J. Zhou, Y. Gu, Y. Hu et al., "Gigantic enhancement in response and reset time of ZnO UV nanosensor by utilizing Schottky contact and surface functionalization," *Applied Physics Letters*, vol. 94, no. 19, Article ID 191103, 2009.

[6] K. Liu, M. Sakurai, and M. Aono, "ZnO-based ultraviolet photodetectors," *Sensors*, vol. 10, no. 9, pp. 8604–8634, 2010.

[7] U. Bangert, A. J. Harvey, R. Jones et al., "Dislocation-induced electronic states and point-defect atmospheres evidenced by electron energy loss imaging," *New Journal of Physics*, vol. 6, 2004.

[8] Y. Ohno, H. Koizumi, T. Taishi et al., "Optical properties of dislocations in wurtzite ZnO single crystals introduced at elevated temperatures," *Journal of Applied Physics*, vol. 104, no. 7, Article ID 073515, 2008.

[9] B. K. Meyer, H. Alves, D. M. Hofmann et al., "Bound exciton and donor-acceptor pair recombinations in ZnO," *Physica Status Solidi B: Basic Research*, vol. 241, no. 2, pp. 231–260, 2004.

[10] V. Khranovskyy, M. O. Eriksson, G. Z. Radnoczi et al., "Photoluminescence study of basal plane stacking faults in ZnO nanowires," *Physica B: Condensed Matter*, vol. 439, pp. 50–53, 2014.

[11] D. O. Dumcenco, Y. S. Huang, D. H. Kuo, and K. K. Tiong, "Photoluminescence characterization of vertically aligned ZnO microrods," *Journal of Luminescence*, vol. 132, no. 8, pp. 1890–1895, 2012.

[12] J. Rodrigues, T. Holz, R. Fath Allah et al., "Effect of N_2 and H_2 plasma treatments on band edge emission of ZnO microrods," *Scientific Reports*, vol. 5, Article ID 10783, 2015.

[13] T. Monteiro, A. J. Neves, M. C. Carmo et al., "Near-band-edge slow luminescence in nominally undoped bulk ZnO," *Journal of Applied Physics*, vol. 98, no. 1, Article ID 013502, 2005.

[14] M. Peres, S. Magalhães, M. R. Soares et al., "Disorder induced violet/blue luminescence in rf-deposited ZnO films," *Physica Status Solidi (C)*, vol. 10, no. 4, pp. 662–666, 2013.

[15] N. Bano, I. Hussain, O. Nur, M. Willander, P. Klason, and A. Henry, "Study of luminescent centers in ZnO nanorods catalytically grown on 4H-p-SiC," *Semiconductor Science and Technology*, vol. 24, no. 12, Article ID 125015, 2009.

[16] C. H. Ahn, Y. Y. Kim, D. C. Kim, S. K. Mohanta, and H. K. Cho, "A comparative analysis of deep level emission in ZnO layers deposited by various methods," *Journal of Applied Physics*, vol. 105, no. 1, Article ID 013502, 2009.

[17] A. B. Djurišić, Y. H. Leung, K. H. Tam et al., "Green, yellow, and orange defect emission from ZnO nanostructures: influence of excitation wavelength," *Applied Physics Letters*, vol. 88, no. 10, Article ID 103107, 2006.

[18] R. Bhaskar, A. R. Lakshmanan, M. Sundarrajan, T. Ravishankar, M. T. Jose, and N. Lakshminarayan, "Mechanism of green luminescence in ZnO," *Indian Journal of Pure & Applied Physics*, vol. 47, no. 11, pp. 772–774, 2009.

[19] G. Xiong, K. B. Ucer, R. T. Williams et al., "Donor-acceptor pair luminescence of nitrogen-implanted ZnO single crystal," *Journal of Applied Physics*, vol. 97, no. 4, Article ID 043528, 2005.

[20] M. Schirra, R. Schneider, A. Reiser et al., "Stacking fault related 3.31-eV luminescence at 130-meV acceptors in zinc oxide," *Physical Review B—Condensed Matter and Materials Physics*, vol. 77, no. 12, Article ID 125215, 2008.

[21] Q. X. Zhao, M. Willander, R. E. Morjan, Q-H. Hu, and E. E. B. Campbell, "Optical recombination of ZnO nanowires grown on sapphire and Si substrates," *Applied Physics Letters*, vol. 83, no. 1, pp. 165–167, 2003.

[22] T. Makino, Y. Segawa, S. Yoshida, A. Tsukazaki, A. Ohtomo, and M. Kawasaki, "Gallium concentration dependence of room-temperature near-band-edge luminescence in n-type ZnO:Ga," *Applied Physics Letters*, vol. 85, no. 5, pp. 759–761, 2004.

[23] J. M. Mánuel, F. M. Morales, R. García, R. Aidam, L. Kirste, and O. Ambacher, "Threading dislocation propagation in AlGaN/GaN based HEMT structures grown on Si (111) by plasma assisted molecular beam epitaxy," *Journal of Crystal Growth*, vol. 357, no. 1, pp. 35–41, 2012.

[24] J. W. Edington, *Practical Electron Microscopy in Material Science*, MacMillan Press, Eindhoven, The Netherlands, 1975.

[25] D. M. Follstaedt, N. A. Missert, D. D. Koleske, C. C. Mitchell, and K. C. Cross, "Plan-view image contrast of dislocations in GaN," *Applied Physics Letters*, vol. 83, no. 23, pp. 4797–4799, 2003.

[26] F. Vigué, P. Vennéguès, S. Vézian, M. Laügt, and J.-P. Faurie, "Defect characterization in ZnO layers grown by plasma-enhanced molecular-beam epitaxy on (0001) sapphire substrates," *Applied Physics Letters*, vol. 79, no. 2, pp. 194–196, 2001.

[27] W.-R. Liu, W. F. Hsieh, C.-H. Hsu, K. S. Liang, and F. S.-S. Chien, "Threading dislocations in domain-matching epitaxial films of ZnO," *Journal of Applied Crystallography*, vol. 40, no. 5, pp. 924–930, 2007.

[28] W.-R. Liu, B. H. Lin, S. Yang et al., "The influence of dislocations on optical and electrical properties of epitaxial ZnO on Si (111) using a γ-Al_2O_3 buffer layer," *CrystEngComm*, vol. 14, no. 5, pp. 1665–1671, 2012.

[29] Y. B. Zhang, G. K. L. Goh, and S. Li, "Reduction of threading dislocations in hydrothermally grown ZnO films by lateral epitaxial overgrowth," *Thin Solid Films*, vol. 518, no. 24, pp. E104–E106, 2010.

[30] Y. Sawai, K. Hazu, and S. F. Chichibu, "Surface stoichiometry and activity control for atomically smooth low dislocation density ZnO and pseudomorphic MgZnO epitaxy on a Zn-polar ZnO substrate by the helicon-wave-excited-plasma sputtering epitaxy method," *Journal of Applied Physics*, vol. 108, no. 6, Article ID 063541, 2010.

[31] M. A. Moram and M. E. Vickers, "X-ray diffraction of III-nitrides," *Reports on Progress in Physics*, vol. 72, no. 3, 2009.

[32] T. Metzger, R. Höpler, E. Born et al., "Defect structure of epitaxial GaN films determined by transmission electron microscopy and triple-axis X-ray diffractometry," *Philosophical Magazine A: Physics of Condensed Matter, Structure, Defects and Mechanical Properties*, vol. 77, no. 4, pp. 1013–1025, 1998.

[33] K. Thonke, T. Gruber, N. Teofilov, R. Schönfelder, A. Waag, and R. Sauer, "Donor-acceptor pair transitions in ZnO substrate

material," *Physica B: Condensed Matter*, vol. 308–310, pp. 945–948, 2001.

[34] L. Wischmeier, T. Voss, I. Rückmann et al., "Dynamics of surface-excitonic emission in ZnO nanowires," *Physical Review B*, vol. 74, no. 19, Article ID 195333, 2006.

[35] J. Grabowska, A. Meaney, K. K. Nanda et al., "Surface excitonic emission and quenching effects in ZnO nanowire/nanowall systems: limiting effects on device potential," *Physical Review B*, vol. 71, no. 11, Article ID 115439, 2005.

[36] K. Thonke, M. Schirra, R. Schneider et al., "The role of stacking faults and their associated 0.13 ev acceptor state in doped and undoped ZnO layers and nanostructures," *Microelectronics Journal*, vol. 40, no. 2, pp. 210–214, 2009.

[37] R. Dingle, "Luminescent transitions associated with divalent copper impurities and the green emission from semiconducting zinc oxide," *Physical Review Letters*, vol. 23, no. 11, pp. 579–581, 1969.

[38] M. A. Reshchikov, H. Morkoç, B. Nemeth et al., "Luminescence properties of defects in ZnO," *Physica B: Condensed Matter*, vol. 401-402, pp. 358–361, 2007.

[39] M. D. McCluskey and S. J. Jokela, "Defects in ZnO," *Journal of Applied Physics*, vol. 106, no. 7, Article ID 071101, 2009.

[40] A. Janotti and C. G. Van de Walle, "Native point defects in ZnO," *Physical Review B—Condensed Matter and Materials Physics*, vol. 76, no. 16, Article ID 165202, 2007.

[41] L. A. Kappers, O. R. Gilliam, S. M. Evans, L. E. Halliburton, and N. C. Giles, "EPR and optical study of oxygen and zinc vacancies in electron-irradiated ZnO," *Nuclear Instruments and Methods in Physics Research B: Beam Interactions with Materials and Atoms*, vol. 266, no. 12-13, pp. 2953–2957, 2008.

[42] A. K. Das, P. Misra, R. Kumar et al., "Studies on highly resistive ZnO thin films grown by DC-discharge-assisted pulsed laser deposition," *Applied Physics A: Materials Science & Processing*, vol. 114, no. 4, pp. 1119–1128, 2014.

[43] L. M. Kukreja, P. Misra, J. Fallert, D. M. Phase, and H. Kalt, "Correlation of spectral features of photoluminescence with residual native defects of ZnO thin films annealed at different temperatures," *Journal of Applied Physics*, vol. 112, no. 1, Article ID 013525, 2012.

[44] Y. Dong, F. Tuomisto, B. G. Svensson, A. Y. Kuznetsov, and L. J. Brillson, "Vacancy defect and defect cluster energetics in ion-implanted ZnO," *Physical Review B—Condensed Matter and Materials Physics*, vol. 81, no. 8, Article ID 081201, 2010.

[45] D. G. Zhao, D. S. Jiang, H. Yang et al., "Role of edge dislocations in enhancing the yellow luminescence of *n*-type GaN," *Applied Physics Letters*, vol. 88, no. 24, Article ID 241917, 2006.

[46] A. Stroud and J. H. You, "Edge dislocation effect on optical properties in wurtzite ZnO," *Journal of Crystal Growth*, vol. 340, no. 1, pp. 92–97, 2012.

[47] M. A. Reshchikov, A. Usikov, H. Helava, and Y. Makarov, "Fine structure of the red luminescence band in undoped GaN," *Applied Physics Letters*, vol. 104, no. 3, Article ID 032103, 2014.

[48] M. A. Reshchikov and H. Morkoç, "Luminescence properties of defects in GaN," *Journal of Applied Physics*, vol. 97, no. 6, Article ID 061301, 2005.

[49] T. Schmidt, K. Lischka, and W. Zulehner, "Excitation-power dependence of the near-band-edge photoluminescence of semiconductors," *Physical Review B*, vol. 45, no. 16, pp. 8989–8994, 1992.

Research Article

Inhibitory Effect Evaluation of Glycerol-Iron Oxide Thin Films on Methicillin-Resistant *Staphylococcus aureus*

C. L. Popa,[1] A. M. Prodan,[2,3,4] P. Chapon,[5] C. Turculet,[2,3] and D. Predoi[1]

[1]*National Institute of Materials Physics, P.O. Box MG 07, 077125 Magurele, Romania*
[2]*Emergency Hospital Floreasca Bucharest, 8 Calea Floresca, Sector 1, 014461 Bucharest, Romania*
[3]*Carol Davila University of Medicine and Pharmacy, 8 Eroii Sanitari, Sector 5, 050474 Bucharest, Romania*
[4]*Department of Science and Engineering of Oxide Materials and Nanomaterials, Faculty of Applied Chemistry and Materials Science, University Politehnica of Bucharest, 1-7 Polizu Street, P.O. Box 12-134, 011061 Bucharest, Romania*
[5]*Horiba Jobin Yvon S.A, 16-18 rue du Canal, 91165 Longjumeau Cedex, France*

Correspondence should be addressed to D. Predoi; dpredoi@gmail.com

The main purpose of this study was to evaluate the inhibitory effect of glycerol- iron oxide thin films on *Methicillin-Resistant Staphylococcus aureus* (MRSA). Our results suggest that glycerol-iron oxide thin films could be used in the future for various biomedical and pharmaceutical applications. The glycerol-iron oxide thin films have been deposited by spin coating method on a silicon (111) substrate. The structural properties have been studied by X-ray diffraction (XRD) and scanning electron spectroscopy (SEM). The XRD investigations of the prepared thin films demonstrate that the crystal structure of glycerol-iron oxide nanoparticles was not changed after spin coating deposition. On the other hand, the SEM micrographs suggest that the size of the glycerol-iron oxide microspheres increased with the increase of glycerol exhibiting narrow size distributions. The qualitative depth profile of glycerol-iron oxide thin films was identified by glow discharge optical emission spectroscopy (GDOES). The GDOES spectra revealed the presence of the main elements: Fe, O, C, H, and Si. The antimicrobial activity of glycerol-iron oxide thin films was evaluated by measuring the zone of inhibition. After 18 hours of incubation at 37°C, the diameters of the zones of complete inhibition have been measured obtaining values around 25 mm.

1. Introduction

During the last decade, iron oxide nanoparticles such as magnetite (Fe_3O_4) and/or maghemite (γ-Fe_2O_3), with various coatings and diameters of 3–30 nm, have been used in biological applications [1] for diagnostics and/or cancer treatment. Recently, functionalized magnetic nanoparticles have been applied in a range of new biomedical and diagnostic applications such as magnetic resonance imaging (MRI), contrast agents [2, 3], targeted drug delivery [4], molecular biology [5], DNA purification [6], cell separation [7], and hyperthermia therapy [8].

The biocompatibility and low toxicity of functionalized iron oxide magnetic nanoparticles [9–11] with different biopolymers are crucial parameters for various applications.

Two of the phases of iron oxides, Fe_3O_4 and γ-Fe_2O_3, present a major interest in numerous applications due to their particular magnetic properties and because iron oxide nanoparticles consist of nontoxic elements several new researches have focused on iron oxide thin films [12].

In previous studies, the growth of hematite (α-Fe_2O_3) thin films by reactive evaporation of iron in an oxygen atmosphere [13] was reported. Akl [14] in her studies on optical properties of crystalline and noncrystalline iron oxide thin films deposited by spray pyrolysis showed that the film structure changed from noncrystalline to crystalline at the same substrate temperature. Moreover, Akl [14] demonstrated that the effect of substrate temperature as well as the deposition time can influence the optical properties, with the optical constants being dependent on the film thickness and independent of the growth temperature. Previous studies have proved that nanoparticles can contribute to bactericidal effects [15]. According to Taylor and Webster [16], iron oxide nanoparticles may bring some supplementary

benefits for biofilm treatment. In their studies on the use of superparamagnetic nanoparticles (SPION) for prosthetic biofilm prevention, they showed that SPION can be used for numerous anti-infection orthopedic applications [16].

The spin coating method used to deposit glycerol-iron oxide thin films is a simple, inexpensive technique and a promising candidate for obtaining biocompatible surfaces for potential applications in the medical field. The specific characteristics of nanoscale iron oxides particles were determined in order to use them in a variety of different applications. On the other hand, glycerol is a natural antimicrobial agent and a common ingredient found in food and cosmetics. According to Projan et al. [17], low concentrations of glycerol can inhibit various *staphylococci*. Moreover, recent studies [18] have shown that the monolaurate glycerol can inhibit growth of Candida and *Gardnerella vaginalis* bacterial strains *in vitro* and *in vivo*, inhibiting the signal transduction at microbial plasma membranes.

This study also reports the preparation and characterization of glycerol-iron oxide layer. Firstly, we synthesized glycerol stabilized with iron oxide nanoparticles in normal atmospheric conditions by coprecipitation method. Secondly, glycerol-iron oxide thin films were prepared by spin coating deposition. The glycerol-iron oxide nanoparticles and glycerol-iron oxide thin films were characterized by X-Ray diffraction (XRD) and scanning electron microscopy (SEM). The qualitative chemical analysis of the glycerol-iron oxide thin films was evaluated by glow discharge optical emission spectroscopy (GDOES). Finally the inhibitory effect of glycerol-iron oxide layer on methicillin-resistant *Staphylococcus aureus* (MRSA) was investigated.

2. Experimental Section

2.1. Thin Film of Glycerol Coated Iron Oxide. Ferrous chloride tetrahydrate ($FeCl_2 \cdot 4H_2O$), ferric chloride hexahydrate ($FeCl_3 \cdot 6H_2O$), chlorhydric acid (HCl), natrium hydroxide (NaOH), and ammonia (NH_3) were purchased from Merck Glycerol. $C_3H_8O_3$, (99.5%) was purchased from Sigma. Deionized water was used in the synthesis of nanoparticles and in the rinsing of clusters. The Ø6″ Silicon Wafer, Type P/⟨100⟩, was purchased from TED PELLA, INC. Microscopy Products for Science and Industry.

The glycerol-iron oxide nanoparticles (GIO) were synthetized by coprecipitation method in air at room temperature. The ferric and ferrous chlorides (molar ratio 2 : 1) were prepared by dissolving 0.30 M of $FeCl_3 \cdot 6H_2O$ and $FeCl_2 \cdot 4H_2O$ in 60 mL of HCl (0.16 M) [19, 20]. The resulting solution was added drop by drop into 200 mL of NaOH (1 M) containing 50 mL glycerol. The suspension was vigorously stirred for 1 h and heated another 2 h at 80°C. Glycerol coated magnetic iron oxide nanoparticles were purified by ultrafiltration after centrifugation at 10000 rpm for 60 min. The resulted glycerol-iron oxide nanoparticles were redispersed in ethanol solutions containing 25 mL (GIO-1) and 50 mL (GIO-2) glycerol under vigorous stirring. Finally, one milliliter of the solution was pipetted onto the substrate (commercially pure Si), and the substrate was spun at 1000 rpm for

30 s. The resulting films were annealed in air at 60°C for 2 h immediately after coating and then heated at 100°C for 1 h in vacuum to remove excess solvent and to further densify the film [9].

2.2. Characterization Methods. The samples were characterized for phase content by X-ray diffraction (XRD) with a Bruker D8-Advance X-ray diffractometer in the scanning range 25–70° using Cu Kα (1.5416 Å) incident radiation. The morphology of the material was studied using a Quanta Inspect F scanning electron microscope (SEM). The top surface analysis of the samples was studied by Glow Discharge Optical Emission Spectroscopy (GDOES) [21, 22] using a GD Profiler 2 from Horiba/Jobin-Yvon. The technique is suitable for thin film analysis and permits determining the chemical gradient composition from the surface to the bulk and, if the ablation rate can be estimated, to determine the thickness of different layers of the nanocomposite materials [23, 24].

Methicillin-resistant *Staphylococcus aureus* (MRSA) bacterial strain was obtained from Polymed Medical Center, Bucharest, Romania. The MRSA strain used in this study was isolated from an abdominal wound after right hemicolectomy. The MRSA strain clinically isolated is believed to be most representative for this type of bacteria. The bacteria were cultured at 37°C in blood agar with 5% sheep blood and a chromogen agar medium CPS3 (Biomerieux Franta). The final working concentration was of 1×10^6 CFU mL^{-1}. MRSA was typed with the latex agglutination assay Slidex Staphylococcus Detection (no. 73117, Biomerieux, Marcy l'Etoile, France) using a cefoxitin disk [25] according to [26]. For this strain a resistance profile was determined using the Kirby–Bauer method with multidisc (Bio-Rad, DF, Mexico) and CLSI guide 2014 edition.

3. Results and Discussions

The XRD investigations of dried GIO nanoparticles are illustrated in Figure 1. Based on XRD data refinement, the GIO nanoparticles synthesized by coprecipitation method showed characteristic peaks which are assigned to the (220), (311), (400), (422), (511), and (440) reflections of the mixture of the spinel phases maghemite (γ-Fe_2O_3) and magnetite (Fe_3O_4). The proportion of the two phases was calculated by Rietveld refinement for the GIO nanoparticles. The maghemite ($a = 0.835$ nm) was found in proportion of 91.9116% ± 0.119 while the magnetite ($a = 0.840$ nm) was found in proportion of 8.0884% ± 0.236. According to previous studies [27] it should be noted that the standard XRD patterns of (γ-Fe_2O_3) and (Fe_3O_4) are difficult to distinguish. The calculated mean size of the nanoparticles was about 7.7 ± 0.023 nm.

SEM analysis was used to observe the morphology of GIO nanoparticles and GIO thin films (GIO-1 and GIO-2). In Figure 2 the SEM image of GIO nanoparticles is presented. The SEM image shows that the glycerol coated iron oxide nanoparticles are spherical and their average diameter is about 9 ± 1 nm. Therefore, the average size of the nanoparticles deduced by SEM investigations is in good agreement with XRD analysis.
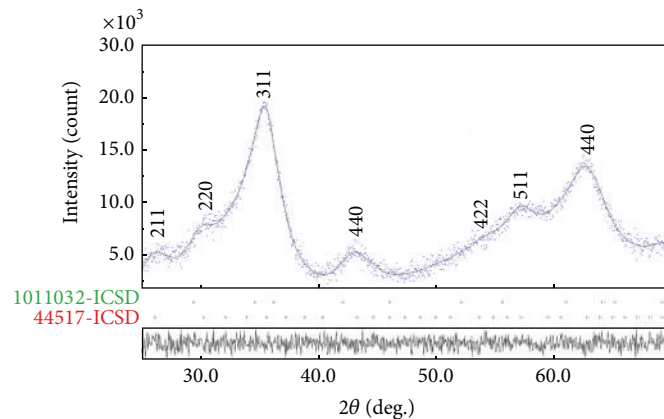
FIGURE 1: Experimental (blue), calculated (solid line gray), and difference plots (lover line) of the glycerol coated iron oxide nanoparticles (mixture of the spinel phases γ-Fe_2O_3 (44517-ICSD) and magnetite Fe_3O_4 (1011032-ICSD)).
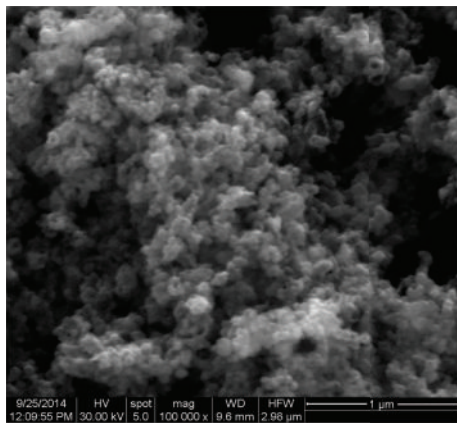
FIGURE 2: SEM image of the glycerol coated iron oxide nanoparticles.

FIGURE 3: X-ray diffraction patterns of GIO-1 and GIO-2 thin films.

The XRD patterns of GIO-1 and GIO-2 thin films are also similar and conserve the structure of GIO nanoparticles (Figure 3). The reflections were assigned to the spinel phases (γ-Fe_2O_3 magnetite Fe_3O_4). The sizes of GIO-1 and GIO-2 thin films were calculated by Sherrer's formula [28]. The average particle sizes of GIO-1 and GIO-2 thin films were estimated to be 18.7 ± 1 nm and 24.8 ± 1 nm, respectively, deduced from the position of characteristic peaks assigned to the (311), (400), (511), and (440) reflections.

The XRD investigations of GIO-1 and GIO-2 thin films demonstrated that the crystal structure of GIO nanoparticles does not change after spin coating deposition.

The morphology and mean nanoparticle diameters of GIO thin films (GIO-1 and GIO-2) are illustrated in Figure 4. The SEM images of GIO thin films (GIO-1 and GIO-2) show a homogenous surface structure. The sizes of the glycerol-iron oxide microspheres obtained on the thin film surfaces exhibit a narrow size distribution (Figure 4). After acquiring SEM micrographs on different areas of the two thin films (GIO-1 and GIO-2), statistical histograms have been performed. These histograms showed that the mean nanoparticle diameters have values around 19.9 ± 0.07 nm for

the GIO-1 thin film (Figure 4(c)) and around 23.9 ± 0.11 nm for the GIO-2 thin film (Figure 4(d)).

Furthermore, the size of the spherical microspheres increases with the increase of glycerol amount (GIO-2).

Glow discharge optical emission spectroscopy (GDOES) is an atomic emission spectrometer system that can be used mainly to analyze elemental composition of solids, liquids, and gases [29]. In our studies, the GDOES method was used for qualitative determination of the constituent elements in the films. According to Jakubéczyová et al. [30], from the concentration profiles it is possible to approximately deduce the layer thickness. However, errors are to be expected in this type of recalculation. Moreover, Vnouček [31] in her studies on "Povrchové efekty při GDOES (Surface Effects at GDOES)" affirms that there is no universal way for the elimination of these inaccuracies and it is necessary to carry out individual calibrations. Similarly, Payling et al. [32] in their studies showed that depth calculation from GDOES measurements is the result of several steps, "each bringing potential uncertainties."

(a)

(b)

(c)

(d)
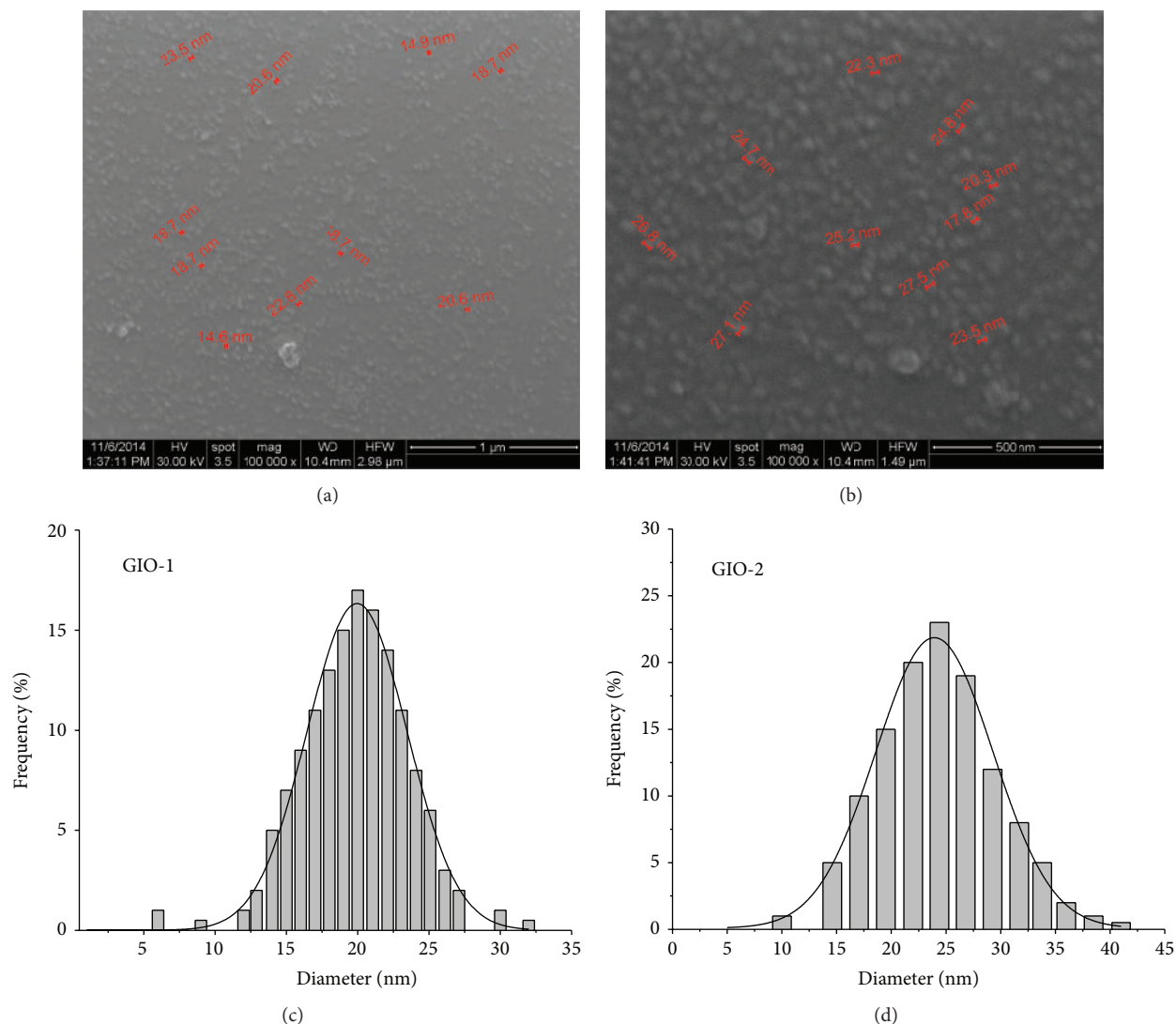
FIGURE 4: SEM images of GIO-1 (a) and GIO-2 (b) thin films. The mean nanoparticle diameters of GIO-1 (c) and GIO-2 (d) thin films.

The elemental distribution from coating to substrate with glycerol-iron oxide nanoparticles was investigated using GDOES depth profile. GDOES spectra were acquired for thin films of glycerol-iron oxide nanoparticles dispersed in ethanol solution containing 25 mL (GIO-1) and 50 mL (GIO-2) glycerol under vigorous stirring and deposited on a pure Si substrate (Figure 5).

The results shown in Figure 5 reveal the distribution of the main elements of the coating and substrate along the depth direction including Fe, O, C, H, and Si. Interpretation is not easy but it is clear that the oxygen content increased at the top surface of the GIO-1 and GIO-2 thin films and the iron content remained constant up to a certain depth for the coating obtained for the two layers. Also, the carbon and hydrogen contents were higher in the coating obtained from glycerol-iron oxide nanoparticles dispersed in the ethanol solution containing 50 mL glycerol (GIO-2). From Figure 5 we also observe that the GIO-2 profile exhibits higher silicon concentrations compared to GIO-1 profile, while the oxygen concentration is slightly higher for GIO-1 compared to the GIO-2; this might be linked to the coverage of the layer on Si over the sputtered area (4 mm).

The objective of our study was to investigate the antibacterial activity of glycerol-iron oxide thin films (GIO-1 and GIO-2) on *Methicillin-Resistant Staphylococcus aureus* bacterial strain. The second substrate, from Figure 6(B), is faded because the glycerol-iron oxide ratio is greater than the one used in Figure 6(A). The increase of the amount of glycerol in the sample leads to a discoloration of the solution used for layer deposition. The antimicrobial activity of glycerol-iron oxide thin films was evaluated in triplicate by measuring the zone of inhibition after 18 hours of incubation at 37°C. After incubation, the diameters of the zones of complete inhibition (seen with the naked eye) were measured. Around glycerol-iron oxide thin films onto commercially pure Si substrate we can see the bright inhibition zones indicating the antibacterial activity (Figure 6). The antibacterial activity increased from 22 ± 1 mm (Figure 6(A)) to 27 ± 1 mm (Figure 6(B)).
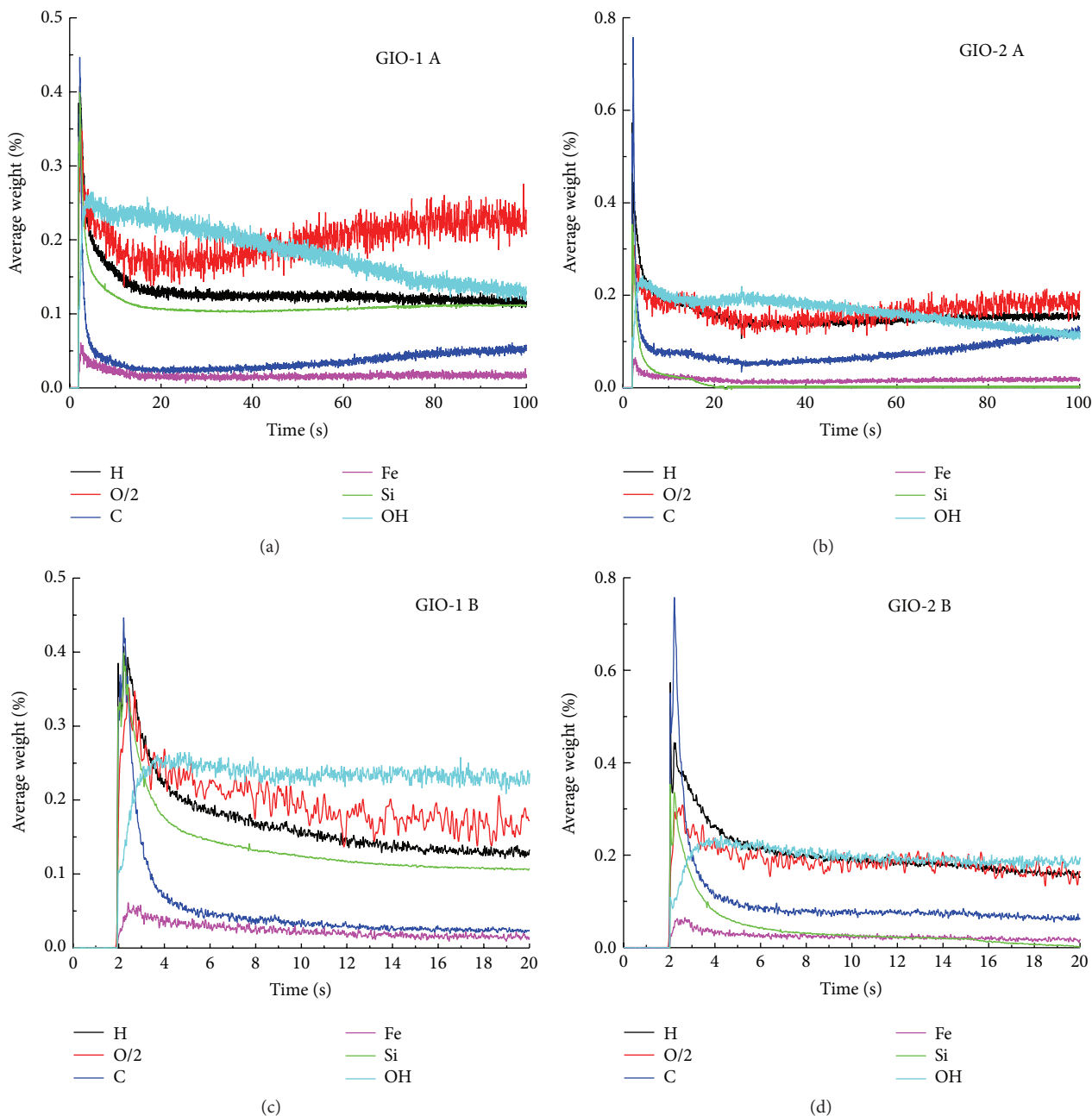
FIGURE 5: Typical GDOES composition depth profiles of GIO-1 A and GIO-2 A thin films after dispersion of glycerol-iron oxide nanoparticles in ethanol solution containing 25 mL and 50 mL glycerol under vigorous stirring. The GIO-1 B and GIO-2 B show zoomed in time regions 0–20 s.

The values of antibacterial activity diameter of the three samples utilized in the study of antimicrobial activity of glycerol-iron oxide thin films are presented in Table 1.

To highlight the antimicrobial effect of GIO thin films, the GIO thin films deposited on commercially pure Si (100) were exposed to the MRSA. After 2, 4, 6, 12, and 24 h the suspension was collected. After collection, the suspension was incubated on agar medium for 24 h. More than that, the number of colonies forming units per milliliter (CFU/mL) was established. In Figure 7 the antimicrobial effect

depending on the time of contact with the surface of the GIO thin films for MRSA was presented.

After 24 h a drastic decrease of the MRSA CFU for the two samples (GIO-1 and GIO-2 thin films) was noticed. As you can see in Figure 7, the antimicrobial effect occurs just 2 h after the time of contact with the surface of GIO-1 and GIO-2 thin films with MRSA. After 6 h of contact with the surface of GIO-1 thin films, the CFU of MRSA decreased linearly up to 24 h. For the GIO-2 thin films, the antimicrobial effect increased linearly in time between 0 and 24 h. After 24 h,
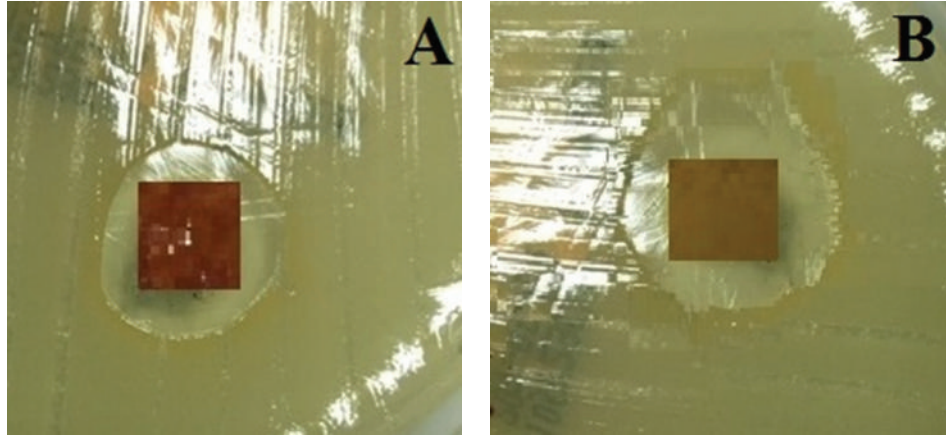
FIGURE 6: Antibacterial activity of glycerol-iron oxide thin films on *Methicillin-resistant Staphylococcus aureus* bacterial strain. A: GIO-1; B: GIO-2.

TABLE 1: The values of antibacterial activity diameter of the three samples utilized for antimicrobial evaluation.

Sample	Diameter of the complete inhibition zones ($D1$)	Diameter of the complete inhibition zones ($D2$)	Diameter of the complete inhibition zones ($D3$)	Mean diameter of the complete inhibition zones ($\widetilde{D}$)
GIO-1	21.6 mm	23.4 mm	21 mm	22 mm
GIO-2	25.8 mm	25.9 mm	29.3 mm	27 mm
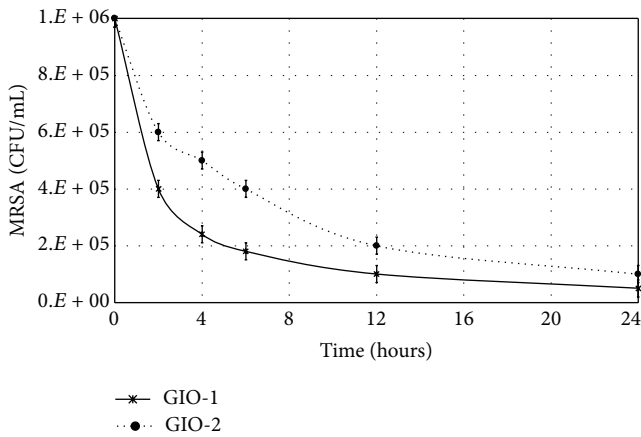
FIGURE 7: The antimicrobial effects depending on the time of contact with the surface of GIO thin films.

the number of MRSA CFU approached to zero. According to the experimental results of the antibacterial studies, the survival bacteria are meaningfully reduced when the amount of glycerol increased. The generation of OH could be the reason why the antimicrobial effectiveness of glycerol layer of iron oxide increased when the amount of glycerol increased.

It is well known that in recent years nanotechnology has made major progress. Thus, different types of metals and metal oxides at the nanoscale with antimicrobial properties were obtained [33–37]. Due to their low toxicity to humans and their antimicrobial activity, silver nanoparticles have been intensively investigated [34, 38]. More recently, the first studies on antimicrobial silver doped hydroxyapatite were

reported by Ciobanu et al. [39, 40]. Iron oxide nanoparticles have been widely used in biomedical research areas due to their special magnetic properties, their surface properties, and their biocompatibility. A major challenge is represented by the production of a magnetic drug delivery system in which magnetic nanoparticles coated with drugs can be directed to infection sites by an external magnetic field [41]. Along this line, we try to find an alternative treatment based only on iron oxide nanoparticles, without the use of antibiotics. Touati [42] in his research on iron and oxidative stress in bacteria showed that reactive oxygen species (ROS) generated by magnetite nanoparticles could kill bacteria without killing healthy cells (cells nonaffected by the bacteria). Our present study on the evaluation of the inhibitory effect of glycerol-iron oxide layer on MRSA bacterial strain could be included in the common effort to find alternative solutions to antibiotics for the treatment or prevention of microbial infections.

The results of our studies are in good agreement with previous studies conducted by Saegeman et al. [43]. In the study on short- and long-term bacterial inhibiting effect of high concentrations of glycerol used in the preservation of skin allografts [43] it was shown that glycerol certainly induces bacteriostasis. Poirier et al. [44] have demonstrated that a prolonged stay at a specific activity of the water activity, a_w (measure of the amount of unbound water that is freely available for microorganisms), is not supported by bacteria. This could demonstrate the bacterial inhibition effect of glycerol because most organisms cannot cope with a low specific water activity a_w. Moreover, Mille et al. [45] showed that glycerol solutions reduce the water content necessary for the bacterial cells.

According to the results presented in this research, it can be concluded that the glycerol-iron oxide thin films possess antimicrobial properties against MRSA bacterial strain. It can be stated that the glycerol-iron oxide layer could be used in the medical field to prepare a new antimicrobial product.

4. Conclusions

In this research, the glycerol-iron oxide thin films were obtained simply by spin coating deposition method on a silicon (111) substrate. The XRD patterns of glycerol-iron oxide thin films conserve the structure of glycerol coated iron oxide nanoparticles. The structure of glycerol-iron oxide thin films is homogenous and the size of the spherical microspheres increases with the increase of glycerol amount. The GDOES spectra performed on glycerol-iron oxide thin films reveal the distribution of the main elements Fe, O, C, H, and Si. The thickness of thin films has been affected by the concentration of glycerol in the glycerol-iron oxide nanoparticles solution.

MRSA bacterial strain presented an inhibition zone which increased when the glycerol amount in the samples increased. In addition, the glycerol-iron oxide thin films showed better antibacterial performance when the amount of glycerol increased. In conclusion, we can say that the present research proposes a new antimicrobial product that could be used for various medical applications involving inhibition of antibiotic-resistant bacteria.

Conflict of Interests

The authors declare that they have no competing interests.

Acknowledgments

References

[1] U. Häfeli, W. Schütt, J. Teller, and M. Zborowski, *Scientific and Clinical Applications of Magnetic Carriers*, Springer, New York, NY, USA, 1997.

[2] L. M. Lacava, Z. G. M. Lacava, M. F. Da Silva et al., "Magnetic resonance of a dextran-coated magnetic fluid intravenously administered in mice," *Biophysical Journal*, vol. 80, no. 5, pp. 2483–2486, 2001.

[3] L. Babes, B. Denizot, G. Tanguy, J. J. Le Jeune, and P. Jallet, "Synthesis of iron oxide nanoparticles used as MRI contrast agents: a parametric study," *Journal of Colloid and Interface Science*, vol. 212, no. 2, pp. 474–482, 1999.

[4] S. M. Moghimi, A. C. Hunter, and J. C. Murray, "Long-circulating and target-specific nanoparticles: theory to practice," *Pharmacological Reviews*, vol. 53, no. 2, pp. 283–318, 2001.

[5] M. A. Bogoyevitch, T. S. Kendrick, D. C. H. Ng, and R. K. Barr, "Taking the cell by stealth or storm? Protein Transduction Domains (PTDs) as versatile vectors for delivery," *DNA and Cell Biology*, vol. 21, no. 12, pp. 879–894, 2002.

[6] M. Uhlen, "Magnetic separation of DNA," *Nature*, vol. 340, no. 6236, pp. 733–734, 1989.

[7] I. Safařík and M. J. Safaříkova, "Use of magnetic techniques for the isolation of cells," *Journal of Chromatography B*, vol. 722, no. 1-2, pp. 33–53, 1999.

[8] A. Jordan, R. Scholz, K. Maier-Hauff et al., "Presentation of a new magnetic field therapy system for the treatment of human solid tumors with magnetic fluid hyperthermia," *Journal of Magnetism and Magnetic Materials*, vol. 225, no. 1-2, pp. 118–126, 2001.

[9] S. L. Iconaru, E. Andronescu, C. S. Ciobanu, A. M. Prodan, P. le Coustumer, and D. Predoi, "Biocompatible magnetic iron oxide nanoparticles doped dextran thin films produced by spin coating deposition solution," *Digest Journal of Nanomaterials and Biostructures*, vol. 7, no. 1, pp. 399–409, 2012.

[10] E. Andronescu, M. Costache, C. S. Ciobanu, A. M. Prodan, and D. Predoi, "Synthesis and characterization of bio-compatible maghemite nanoparticles," *Digest Journal of Nanomaterials and Biostructures*, vol. 5, no. 3, pp. 779–786, 2010.

[11] E. Andronescu, C. S. Ciobanu, L. Pall, M. Costache, and D. Predoi, "Preliminary biocompatibility studies of hydroxyapatite coated iron oxide," *Romanian Journal of Materials*, vol. 40, no. 3, pp. 242–249, 2010.

[12] D. Predoi, C. S. Ciobanu, M. Radu et al., "Hybrid dextran-iron oxide thin films deposited by laser techniques for biomedical applications," *Materials Science and Engineering C*, vol. 32, no. 2, pp. 296–302, 2012.

[13] M. F. Al-Kuhaili, M. Saleem, and S. M. A. Durrani, "Optical properties of iron oxide (α-Fe$_2$O$_3$) thin films deposited by the reactive evaporation of iron," *Journal of Alloys and Compounds*, vol. 521, pp. 178–182, 2012.

[14] A. A. Akl, "Optical properties of crystalline and non-crystalline iron oxide thin films deposited by spray pyrolysis," *Applied Surface Science*, vol. 233, no. 1–4, pp. 307–319, 2004.

[15] S. S. Behera, J. K. Patra, K. Pramanik, N. Panda, and H. Thatoi, "Characterization and evaluation of antibacterial activities of chemically synthesized iron oxide nanoparticles," *World Journal of Nano Science and Engineering*, vol. 2, no. 4, pp. 196–200, 2012.

[16] E. N. Taylor and T. J. Webster, "The use of superparamagnetic nanoparticles for prosthetic biofilm prevention," *International Journal of Nanomedicine*, vol. 4, pp. 145–152, 2009.

[17] S. J. Projan, S. Brown-Skrobot, P. M. Schlievert, F. Vandenesch, and R. P. Novick, "Glycerol monolaurate inhibits the production of beta-lactamase, toxic shock toxin-1, and other staphylococcal exoproteins by interfering with signal transduction," *Journal of Bacteriology*, vol. 176, no. 4, pp. 4204–4209, 1994.

[18] K. L. Strandberg, M. L. Peterson, Y.-C. Lin, M. C. Pack, D. J. Chase, and P. M. Schlievert, "Glycerol monolaurate inhibits *Candida* and *Gardnerella vaginalis in vitro* and *in vivo* but not *Lactobacillus*," *Antimicrobial Agents and Chemotherapy*, vol. 54, no. 2, pp. 597–601, 2010.

[19] E. H. Kim, Y. Ahn, and H. S. Lee, "Biomedical applications of superparamagnetic iron oxide nanoparticles encapsulated within chitosan," *Journal of Alloys and Compounds*, vol. 434-435, pp. 633–636, 2007.

[20] B. Gaihre, S. Aryal, N. A. M. Barakat, and H. Y. Kim, "Gelatin stabilized iron oxide nanoparticles as a three dimensional

template for the hydroxyapatite crystal nucleation and growth," *Materials Science and Engineering C*, vol. 28, no. 8, pp. 1297–1303, 2008.

[21] J. Malherbe, B. Fernández, H. Martinez, P. Chapon, P. Panjan, and O. F. X. Donard, "In-depth profile analysis of oxide films by radiofrequency glow discharge optical emission spectrometry (rf-GD-OES): possibilities of depth-resolved solid-state speciation," *Journal of Analytical Atomic Spectrometry*, vol. 23, no. 10, pp. 1378–1387, 2008.

[22] M. Wilke, G. Teichert, R. Gemma et al., "Glow discharge optical emission spectroscopy for accurate and well resolved analysis of coatings and thin films," *Thin Solid Films*, vol. 520, no. 5, pp. 1660–1667, 2011.

[23] M. V. Barbosa, G. Hammes, C. Binder, A. N. Klein, and J. D. B. De Mello, "Physicochemical characterisation of tribolayers by micro-Raman and GDOES analyses," *Tribology International*, vol. 81, pp. 223–230, 2014.

[24] S. M. Barinov, J. V. Rau, S. N. Cesaro et al., "Carbonate release from carbonated hydroxyapatite in the wide temperature rage," *Journal of Materials Science: Materials in Medicine*, vol. 17, no. 7, pp. 597–604, 2006.

[25] Department of Health and Human Services. Centers for Disease Control, "Detection of Oxacillin/Methicillin-resistant *Staphylococcus aureus*," April 2008, http://www.cdc.gov/ncidod/dhqp/ar_lab_mrsa.html.

[26] N. V. Ayala-Núñez, H. H. L. Villegas, L. del Carmen Ixtepan Turrent, and C. Rodríguez Padilla, "Silver nanoparticles toxicity and bactericidal effect against methicillin-resistant staphylococcus aureus: Nanoscale does matter," *Nanobiotechnology*, vol. 5, no. 1–4, pp. 2–9, 2009.

[27] G. Schimanke and M. Martin, "In situ XRD study of the phase transition of nanocrystalline maghemite (γ-Fe$_2$O$_3$) to hematite (α-Fe$_2$O$_3$)," *Solid State Ionics*, vol. 136-137, pp. 1235–1240, 2000.

[28] H. P. Klug and L. E. Alexander, *X-Ray Diffraction Procedures for Polycrystalline and Amorphous Materials*, John Wiley & Sons, New York, NY, USA, 1962.

[29] T. K. Rout, "Nanolayered oxide on a steel surface reduces surface reactivity: evaluation by glow discharge optical emission spectroscopy (GDOES)," *Scripta Materialia*, vol. 56, no. 7, pp. 573–576, 2007.

[30] D. Jakubéczyová, P. Hvizdoš, and M. Selecká, "Investigation of thin layers deposited by two PVD techniques on high speed steel produced by powder metallurgy," *Applied Surface Science*, vol. 258, no. 12, pp. 5105–5110, 2012.

[31] M. Vnouček, *Surface effects at GDOES [Ph.D. Study Work]*, University of West Bohemia, Pilsen, Czech Republic, 2002 (Czech).

[32] R. Payling, D. G. Jones, and A. Bengston, *Glow Discharge Optical Emission Spectrometry*, John Wiley & Sons, New York, NY, USA, 1997.

[33] P. K. Stoimenov, R. L. Klinger, G. L. Marchin, and K. J. Klabunde, "Metal oxide nanoparticles as bactericidal agents," *Langmuir*, vol. 18, no. 17, pp. 6679–6686, 2002.

[34] A. D. Russell and W. B. Hugo, "Antimicrobial activity and action of silver," in *Progress in Medicinal Chemistry*, vol. 31, chapter 7, pp. 351–370, Elsevier, 1994.

[35] C. S. Ciobanu, S. L. Iconaru, M. C. Chifiriuc, A. Costescu, P. Le Coustumer, and D. Predoi, "Synthesis and antimicrobial activity of silver-doped hydroxyapatite nanoparticles," *BioMed Research International*, vol. 2013, Article ID 916218, 10 pages, 2013.

[36] C. S. Ciobanu, S. L. Iconaru, I. Pasuk et al., "Structural properties of silver doped hydroxyapatite and their biocompatibility," *Materials Science and Engineering C*, vol. 33, no. 3, pp. 1395–1402, 2013.

[37] A. M. Prodan, S. L. Iconaru, C. M. Chifiriuc et al., "Magnetic properties and biological activity evaluation of iron oxide nanoparticles," *Journal of Nanomaterials*, vol. 2013, Article ID 893970, 7 pages, 2013.

[38] J. R. Morones, J. L. Elechiguerra, A. Camacho et al., "The bactericidal effect of silver nanoparticles," *Nanotechnology*, vol. 16, no. 10, pp. 2346–2353, 2005.

[39] C. S. Ciobanu, F. Massuyeau, L. V. Constantin, and D. Predoi, "Structural and physical properties of antibacterial Ag-doped nano-hydroxyapatite synthesized at 100°C," *Nanoscale Research Letters*, vol. 6, no. 1, article 613, 2011.

[40] C. S. Ciobanu, S. L. Iconaru, P. Le Coustumer, L. V. Constantin, and D. Predoi, "Antibacterial activity of silver doped hydroxyapatite nanoparticles against gram-positive and gram-negative bacteria," *Nanoscale Research Letters*, vol. 7, no. 1, pp. 324–332, 2012.

[41] N. Tran, A. Mir, D. Mallik, A. Sinha, S. Nayar, and T. J. Webster, "Bactericidal effect of iron oxide nanoparticles on *Staphylococcus aureus*," *International Journal of Nanomedicine*, vol. 5, no. 1, pp. 277–283, 2010.

[42] D. Touati, "Iron and oxidative stress in bacteria," *Archives of Biochemistry and Biophysics*, vol. 373, no. 1, pp. 1–6, 2000.

[43] V. S. M. Saegeman, N. L. Ectors, D. Lismont, B. Verduyckt, and J. Verhaegen, "Short- and long-term bacterial inhibiting effect of high concentrations of glycerol used in the preservation of skin allografts," *Burns*, vol. 34, no. 2, pp. 205–211, 2008.

[44] I. Poirier, P.-A. Maréchal, and P. Gervais, "Effects of the kinetics of water potential variation on bacteria viability," *Journal of Applied Microbiology*, vol. 82, no. 1, pp. 101–106, 1997.

[45] Y. Mille, L. Beney, and P. Gervais, "Viability of *Escherichia coli* after combined osmotic and thermal treatment: a plasma membrane implication," *Biochimica et Biophysica Acta*, vol. 1567, pp. 41–48, 2002.

Research Article

Easy Formation of Nanodisk-Dendritic ZnO Film via Controlled Electrodeposition Process

Nur Azimah Abd Samad, Chin Wei Lai, and Sharifah Bee Abd Hamid

Nanotechnology & Catalysis Research Centre (NANOCAT), 3rd Floor, Block A, Institute of Postgraduate Studies (IPS), University of Malaya, 50603 Kuala Lumpur, Malaysia

Correspondence should be addressed to Chin Wei Lai; cwlai@um.edu.my

A facile electrodeposition synthesis was introduced to prepare the nanodisk-dendritic ZnO film using a mixture solution of zinc chloride ($ZnCl_2$) with potassium chloride (KCl) that acted as a directing agent. This study aims to determine the best photoelectrochemical response for solar-induced water splitting. Based on our results obtained, it was found that an average diagonal of nanodisk was approximately 1.70 μm with the thickness of ≈150 nm that was successfully grown on the surface of substrate. The photocatalytic and photoelectrochemical responses of the resultant wurtzite type based-nanodisk-dendrite ZnO film as compared to the as-prepared ZnO film were monitored and evaluated. A photocurrent density of 19.87 mA/cm^2 under ultraviolet rays and 14.05 mA/cm^2 under visible light (500 nm) was recorded for the newly developed nanodisk-dendritic ZnO thin film. It was believed that nanodisk-dendritic ZnO film can harvest more incident photons from the illumination to generate more photoinduced charge carriers to trigger the photocatalytic and photoelectrochemical reactions. Moreover, strong light scattering effects and high specific surface area of 2D nanostructures aid in the incident light absorption from any direction.

1. Introduction

Behind the rapid development of social, economic, and technology, energy becomes a crucial issue around the globe. A global warming devastation occurs from time to time and is becoming severe in the 21st century. Abrupt climate change happens around the world. Intergovernmental Panel on Climate Change (IPCC) is the responsible body to control the global temperature variation; it had announced that the global temperature absolutely increased with the estimation of 0.4 and 0.8°C for the past century and this phenomenon was the 10 warmest years over the last 15 years [1]. In the North Atlantic, the atmospheric circulation above Greenland also changed abruptly due to the global warming [2, 3]. Global warming phenomenon occurred as a result of greenhouse effect which led to the increasing in atmospheric temperature [3]. Increases in concentration of greenhouse gases such as nitrous oxide (N_2O), methane (CH_4), and carbon dioxide (CO_2) were the main causes of the drought in the areas from East Africa coastal area to the Arabian Sea, South Asia, East Asia, and South China. In the case of water (sea/river) level

rising during the 21st century, global warming resulted in the melting of remaining ice masses. IPCC forecasts global mean sea levels (GMSLs) are likely to increase with the variation of 4-5 mm/year by 2050, 0.5–0.9 m by 2100, thus the losses of up to 30% of coastal wetlands [4]. Two major net heat sources had documented (1) net heating generated by human activities and (2) geothermal heat flow. In addition, the exploitation of nuclear energy and nonrenewable energy thus produces an additional heat in the world [5]. These driving forces lead the researchers to reduce the greenhouse effect and environmental protection with presenting creative ideas. In this paper, we are focusing on the alternative energy, hydrogen gas production. Today's hydrogen production is produced from fossil fuels, methane, and coal gasification [6]. The production of hydrogen gas determines the environmental impact and energy efficiency. Light-induced water splitting system is attractive to be studied. Thus, the photocatalysed degeneration of water with nanodisk-dendritic zinc oxide film was chosen to be the catalyst.

Zinc oxide is an n-type semiconductor, with direct wide band gap (3.37 eV) due to its electrons conductivity, and it has

TABLE 1: The different types of hexagonal ZnO disk based on preparation method.

Researcher	Preparation methods	Findings	References
Yin et al. (2014)	*Simple double-solvothermal method in the presence of glycine*	Complex superstructure was assembled by hexagonal disks; the thickness of the disk is about 300 nm	[25]
Zeng et al. (2009)	*Hydrothermal* method	Uniform single-crystalline ZnO nanodisks were well developed with 1.5 μm in diameter and 300 nm in thickness	[17]
Zhang et al. (2007)	*Electrodeposition* method, HBO$_3$ as an electrolyte with zinc foil as anode, voltage 180 V, and the system kept at 2°C	Zinc/ZnO core-shell hexagonal nanodisk dendrites were produced with diameter from about 100 nm to several hundred nanometers and thicknesses are about 20–40 nm.	[15]
Li et al. (2007)	*Electrochemical deposition* method	The shape of the ZnO dendritic structure is similar to the branch of a fern; ZnO dendritic structure is in the range of 6–10 μm and 200 nm of thickness	[26]
Xu et al. (2004)	*Vapour phase transport (VPT)* method	Zinc oxide nanodisk; 3 μm in diagonal and 300 nm in thickness	[21]

the wurtzite hexagonal crystal structure. The stoichiometric excess of zinc ions is believed to cause the electrons conductivity where the zinc ions live in interstitial locations in the crystal lattice [7]. The other property of ZnO is the high exciton binding energy (60 meV) in ZnO crystal which can produce efficient excitonic emission under room temperature ultraviolet (UV) luminescence [8–10]. Moreover, rectification, optical properties, and chemical properties of ZnO bring great interest to the research world [9–16]. Synthesis method will determine the crystal shape from acicular needles to plate shaped crystal. By all means, this is the uniqueness of zinc oxide which can be made to form into a variety of crystalline shapes [17]. Furthermore, nearly neutral (pH ∼ 6) system applied to the formation of ZnO nanostructures supports the environmental protection [17]. According to Table 1, electrochemical deposition method is likely to produce nanodisk-dendritic ZnO and disk-shape morphology is less familiar in research. At the same time, it has unique properties and leads to potential applications such as water-splitting process [18], electrodes for dye sensitized solar cells [19], and nanosensors [20, 21]. Equally important, the low active surface area and fast recombination losses of photoinduced charge carriers remain as a great challenge for ZnO nanostructures. Therefore, in this paper, the formation of nanodisk-dendritic zinc oxide was studied. The ability of nanodisk-dendritic ZnO photoelectrode in current-voltage characteristics and methyl orange (MO) degradation also has been studied.

2. Experimental Section

2.1. Synthesis of Nanodisk-Dendritic ZnO. ZnO nanostructures films were produced by electrodeposition process of zinc (Zn) foil (thickness 0.25 mm, 99.9% trace metals basis, Sigma-Aldrich) in a bath with electrolytes composed of 50 mL

of 0.5 mM zinc chloride (ZnCl$_2$) and 50 mL of 0.1 M potassium chloride (KCl) at 3.0 V at temperature of 80°C. From our literature studies, 3.0 V and 80°C were selected in our study because the polycrystalline structure of ZnO will start to evolve at this potential difference and temperature with obviously and randomly oriented grains. The as-prepared pH of electrolyte is about 5-6, which was measured using a pH meter Mettler Toledo InLab Expert Pro. The electrodeposition process was conducted with two-electrode configuration system, where platinum electrode served as anode and Zn foil served as cathode. This closed system was then connected to a DC power supply. After electrodeposition process, the nanodeposit has been rinsed thoroughly with acetone for analysis Emsure Acs, Iso, Reag. Ph Eur for analysis and dried at atmosphere. The deposited ZnO nanostructured film was then annealed at 600°C for 3 hours because the zinc peaks will be negligible and completely oxidised [15].

2.2. Characterizations of Nanodisk-Dendritic ZnO. The crystallinity and phase transition of the samples were analyzed by using Bruker D8 Advance equipped with EVA-Diffract Software (Germany) X-ray Diffraction (XRD) with Cu K$_\alpha$ radiation and wavelength λ = 1.5418 Å. Meanwhile, the surface and cross-sectional morphologies of the samples have been viewed by Field Emission Scanning Electron Microscopy (FESEM) Quanta FEG 450 and the elemental analysis of ZnO nanostructured film was determined with Hitachi Energy Dispersive X-Ray Spectroscopy (EDX) analysis.

To study the photocurrent density of the sample, a three-electrode PEC cell with nanodisk-dendritic ZnO film served as anode, a platinum rod as the cathode, and a saturated calomel electrode (SCE) as the reference electrode arranged in a quarts cell filled with 1 M sodium hydroxide (NaOH) containing 1 v% of ethylene glycol. A 150 W xenon lamp (Zolix
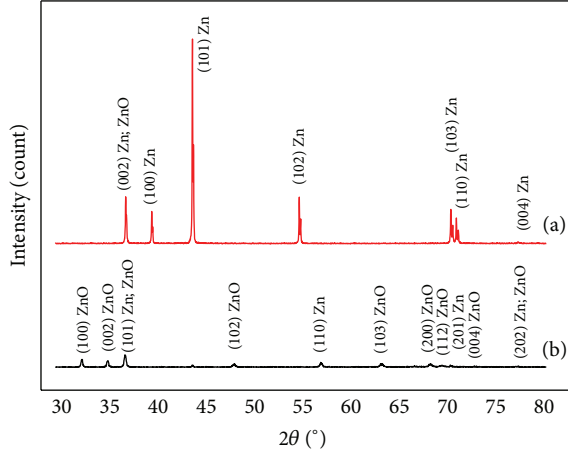
FIGURE 1: XRD pattern of (a) as-prepared ZnO and (b) annealed nanodisk-dendritic ZnO.

TABLE 2: Average compositional ratio of nanodisk-dendritic ZnO and as-prepared ZnO using EDX spectroscopy analysis.

Element	Atomic percentage (%)	
	Nanodisk-dendritic ZnO	As-prepared ZnO
Zinc	42.59	84.32
Oxygen	57.41	15.68

LSP-X150) was set to focus on the immersed portion of the photoelectrode to stimulate solar irradiation. The three electrodes were connected to the potentiostat (Metrohm Autolab PGSTAT204); the current-voltage value was measured. The photocurrent density has been measured by using Metrohm Autolab PGSTAT204, with linear sweep voltammetry potentiostatic procedure (−1 to 1 V potential applied). Photocatalytic degradation studies were implemented by dipping the nanodisk-dendritic ZnO thin film in 100 mL of 15 parts per million (ppm) of methyl orange (MO) solution in a quartz glass tube and placed in the photoreactor. The samples were photoilluminated at room temperature by using TUV 18 W UV-C Germicidal light. After leaving it in a reactor for 30 minutes in dark environment, 5 mL solution was withdrawn for every 1 hour from the quartz tubes to study the degradation of methyl orange (MO) after UV irradiation. A UV-Vis Spectrophotometer (UV-3101PC Shimadzu) was used to analyze the degradation percentage of MO solution.

3. Results and Discussion

3.1. Phase Transformation for Nanodisk-Dendritic ZnO. In this part of experiment, XRD analysis was used to investigate the crystallinity of the nanodisk-dendritic ZnO thin film and as-prepared ZnO thin film as presented in Figure 1. The XRD pattern of the as-prepared ZnO thin film exhibited major Zn phase, which points to the existence of amorphous nature (Figure 1(a)). The Bragg reflection of Zn phase was detected at 2θ values of $36.30°$, $39.00°$, $43.23°$, $54.33°$, $70.08°$, $70.65°$, and $77.02°$ in entire XRD patterns, corresponding to (002), (100), (101), (102), (013), (110), and (004) crystal planes, respectively. The presence of Zn phase was identified by ICDD file of 00-004-0831. Meanwhile, for nanodisk-dendritic ZnO thin film (Figure 1(b)), the result showed that the samples were in line with reference code ICDD 00-036-1451 which indicates the ZnO phase. The Bragg reflection of ZnO phase was detected at 2θ values of $31.75°$, $34.51°$, $36.31°$, $47.60°$, $62.29°$, $66.41°$, $67.94°$, $70.02°$, and $77.0°$ in entire XRD patterns, corresponding to (100), (002), (101), (102), (103), (200), (112),

(004), and (202) crystal planes, respectively. It showed that the sample was crystallized and uniform lattice strain was obtained after calcination process. All peaks were shifted to the left as the ZnO crystals were well and denser after calcination process. In addition, the nanodisk-dendritic ZnO sample is matched with the chemical formula ZnO (referring to XRD test) and consists of hexagonal crystal system. Besides, it also matched the wurtzite type because $a = 3.2498$ Å, $b = 3.2498$ Å, and $c = 5.2066$ Å. The wurtzite type is important in semiconductor application as compared to other crystal structures of ZnO: zinc blende and rocksalt. The significance of wurtzite type ZnO was obtained from the ideal arrangement, by changing the c/a ratio or the u value. From experimental observation, c/a ratios are smaller than ideal ones. In addition, c/a ratio also showed the association of difference for two constituents' electronegativity. Consequently, components with the greatest difference show largest departure from the ideal c/a ratio [22–24].

3.2. Morphological Structure of Nanodisk-Dendritic ZnO. Substrate was shrill of nanodisk-dendritic ZnO (Figure 2(a)). The nanodisk-dendritic zinc oxides have a perfect hexagonal shape with diagonal of approximately 1.7 μm and thickness of approximately 150.4 nm. This result is in line with past researches at which nanodisk-dendritic ZnO exhibits unique characteristics and consists of overlapping nanodisks and self-tiered structure [15]. The stem and the leaflets were built of hexagonal nanodisks where they were self-arranged and self-assembled and became little leaves. The EDX spectroscopy analysis was performed and it showed average atomic percentage of 42.59% and 57.41% of zinc and oxygen, respectively, for nanodisk-dendritic ZnO and average atomic percentage of 84.32% and 15.68% of zinc and oxygen, respectively, for as-prepared ZnO (Table 2). In this study, two-step process took place under dynamic electrolyte for the formation of nanodisk-dendritic ZnO. The first step was the formation of zinc hydroxide ($Zn(OH)_2$), followed by formation of zinc oxide (ZnO). However, this process occurred at all time until the reaction stopped. In the first place, the process started with dissolution of zinc chloride, potassium chloride and water to potassium ion (K^+), zinc ion (Zn^{2+}), chloride ion ($Cl^−$), and hydroxide ion ($OH^−$) and formation of hydrogen gas (H_2) occurred in the electrolyte by electrochemical process with energy supplied from direct electric current that separated the electrolyte into ions [27, 28] (1). Second, for the formation of zinc hydroxide ($Zn(OH)_2$) (intermediate growth stage), the K^+ (as directing agent) attracted the $OH^−$ to the cathode and produced increases in local pH, and saturation level changed at the cathode. When a supersaturation condition is reached, the nucleation of $Zn(OH)_2$ precipitation
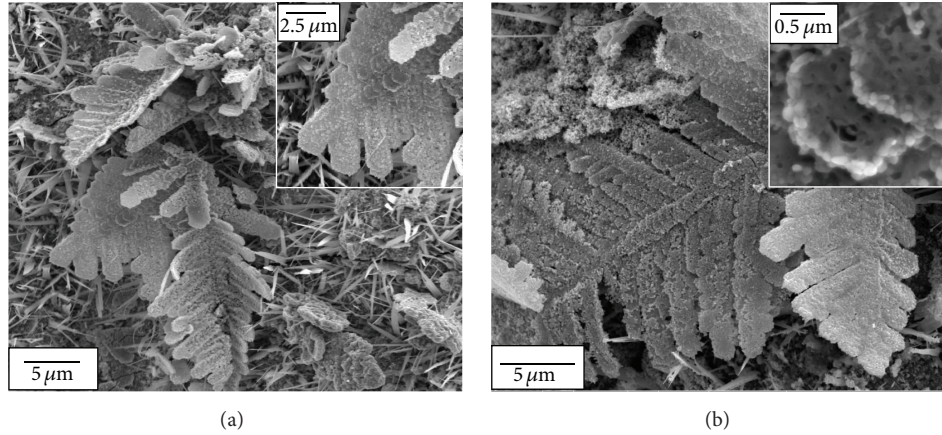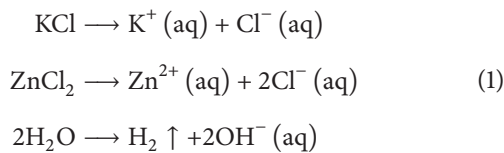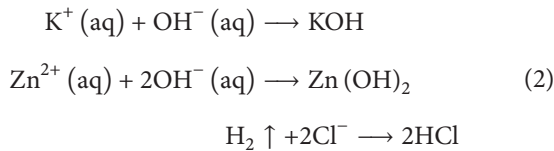
(a)

(b)

Figure 2: FESEM image of (a) ×6k magnification of nanodisk-dendritic ZnO; (inset) ×20k magnification of stacked hexagonal-shape nanodisk ZnO and (b) ×10k magnification of nanodisk-dendritic ZnO; (inset) ×100k magnification hexagonal-shape nanodisk ZnO.

occurred on the substrate surface (cathode) (2). The formation of zinc oxide (ZnO) occurred by dehydration process of $Zn(OH)_2$ on the substrate (3). At the beginning of deposition process, the Zn^{2+} concentration at the substrate surface decreased when pH is increased leading to slowest growth rate towards (0001). Diffusion of Zn^{2+} from (0001) to the substrate surface leads to the unit growing at preferential growth of [1000] direction. When many nanodisks stacked together, it is important to realize that their arrangements on the substrate were on horizontal position (1000) which is in the x-axis direction and it is clearly seen in symmetry shape. The crystal growth velocity along various planes depended on the atomic packing density [15]. (Figure 2(a) inset and Figure 2(b) inset). Below are the equations related to the formation of ZnO:

Dissolution of $KCl + ZnCl_2 + H_2O$ is as follows:

$$KCl \longrightarrow K^+ (aq) + Cl^- (aq)$$

$$ZnCl_2 \longrightarrow Zn^{2+} (aq) + 2Cl^- (aq) \qquad (1)$$

$$2H_2O \longrightarrow H_2 \uparrow + 2OH^- (aq)$$

Formation of zinc hydroxide $(Zn(OH)_2)$, KOH, and KCl is as follows:

$$K^+ (aq) + OH^- (aq) \longrightarrow KOH$$

$$Zn^{2+} (aq) + 2OH^- (aq) \longrightarrow Zn (OH)_2 \qquad (2)$$

$$H_2 \uparrow + 2Cl^- \longrightarrow 2HCl$$

Formation of zinc oxide (ZnO) is as follows:

$$Zn (OH)_2 \longrightarrow ZnO + H_2O \quad \text{(dehydration process)}$$

$$HCl + KOH \longrightarrow H_2O + KCl \qquad (3)$$
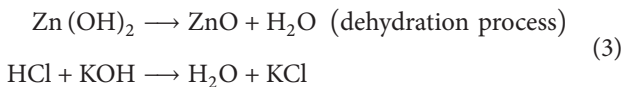
Past researches found the formation of dendrite shape due to the fast growth velocity of Zn ion in the electrolyte [29, 30].

Growth mechanism occurred in global diffusion and later oriented attachments were localized. Dislocation from the early crystal growth happened due to the high velocity of electrolyte (>350 rpm). Therefore, the second hexagonal nanodisk has grown slightly dislocated from the earlier crystal. Another key point is that nanodisk-dendritic tips were known to grow in the direction of maximum surface energy. The (1000) facet was out of sorts; therefore it contributed to highest effective surface energy [15, 31].

3.3. Photocatalytic Activity Evaluation. The photocatalytic activities of the nanodisk-dendritic ZnO and as-prepared ZnO were investigated using the MO degradation method under UV light radiation with the purpose to support the photocatalytic activity argument of nanodisk-dendritic ZnO. It was confirmed that nanodisk-dendritic ZnO exhibited good photocatalytic property when MO solution was degraded for approximately 80% after 6 hours under UV irradiation. Nanodisk-dendritic ZnO exhibited higher photocatalytic activity compared to as-prepared ZnO with MO concentration 18% after 6 hours (Figure 3(a)). Decomposition of MO solution can be explained by an oxidation process that took place on the surface of nanodisk-dendritic ZnO via photogenerated hole. In other words, an electron-hole pair existed in the absence of light intensity [32–34]. Under UV light illumination, energy produced was higher than nanodisk-dendritic ZnO band gap energy. Therefore, electrons at the conduction band and holes at the valence band were generated. Holes at the nanodisk-dendritic ZnO surfaces react with water to form highly reactive hydroxyl radicals $(OH^\bullet)$, and at the same time oxygen acts as an electron acceptor by being a superoxide radical anion [35]. The superoxide radical anions from hydroxyl radicals have an excellent oxidation ability [36] which may degrade organic dye, and, in MO decomposition, it was degraded to carbon dioxide and water [31]. Nanodisk-dendritic ZnO showed high photocatalytic property due to its high surface area and active photoresponse (2D structure).

FIGURE 3: Photodegradation of MO solution by (a) nanodisk-dendritic ZnO and (b) as-prepared ZnO with increasing degradation time.

FIGURE 5: Current density-voltage characteristics for (a) nanodisk-dendritic ZnO, (b) as-prepared ZnO under visible light, and (c) nanodisk-dendritic ZnO without illumination.

FIGURE 4: Current density-voltage characteristics for (a) nanodisk-dendritic ZnO and (b) as-prepared ZnO under ultraviolet ray and (c) nanodisk-dendritic ZnO without illumination.

3.4. Photoelectrochemical Response.

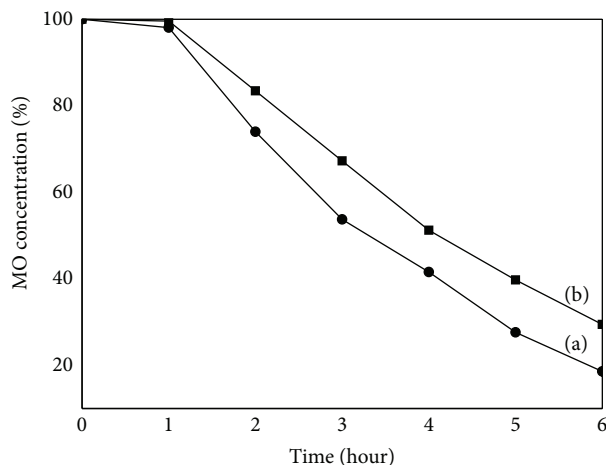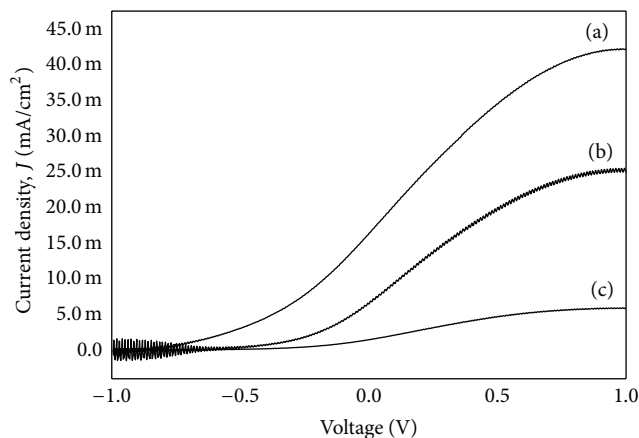A scanning potentiostat by mean to measure current (I) under an applied potential (V) could test the efficiency of nanodisk-dendritic ZnO photocatalytic activity. For water electrolysis application, the efficiencies of over 90% are at −1 to 1 V [37, 38]. From now on, in order to understand the efficiency nanodisk-dendritic ZnO thin films in water electrolysis, sample was evaluated and tested their I-V characteristics between −1 V and 1 V. Figure 4 was plotted to exhibit I-V characteristic curves for the (a) nanodisk-dendritic ZnO, (b) as-prepared ZnO under ultraviolet ray, and (c) nanodisk-dendritic ZnO without illumination. The significant photocurrent density j_p of an average value of 19.87 mA/cm^2 for nanodisk-dendritic ZnO under ultraviolet ray (Figure 4(a)) was obtained as compared to 6.45 mA/cm^2 for as-prepared ZnO under ultraviolet ray (Figure 4(b)) and 1.49 mA/cm^2 for nanodisk-dendritic ZnO without illumination (Figure 4(c)). The catalytic activity contribution can be observed from photocurrent density

differences under ultraviolet ray illumination and without ultraviolet ray illumination. However, the current density j value decreased with the increasing of spectrum wavelength until visible light spectrum (390–700 nm) is reached. Under visible light, average j_p of 14.05 mA/cm^2 was observed for the nanodisk-dendritic ZnO (Figure 5(a)), which is relatively higher when compared to as-prepared ZnO under visible light: j_p 2.14 mA/cm^2 (Figure 5(b)) and nanodisk-dendritic ZnO without illumination: 1.49 mA/cm^2 (Figure 5(c)).

Based on the results of j-V characteristic curves (Figures 4 and 5), as-prepared-ZnO film showed poor result due to the existence of oxygen vacancies inside the ZnO bulk, which points to the increasing number of recombination centers. The recombination centers clearly contributed to the decreasing of photoinduced e$^-$ mobility and back to the contact of Zn substrate because of series of resistance caused by increasing trap states. Besides, the amorphous phase comprises high concentration of other material defects such as impurities, dangling bonds, and microvoids, which similarly act as recombination center and result in a decrease of j_p [39]. Predominantly, as-prepared-ZnO film is basically unable to develop a regular depletion region [40]. It was found that the j_p of heat treated (600°C) nanodisk-dendritic ZnO sample was slightly increased to 19.87 mA/cm^2, which suggests that crystal structure of nanodisk-dendritic ZnO sample can improve the photocurrent generation effectively. In addition, the high specific surface area of nanodisk-dendritic architecture might have contributed to the strong light scattering effects and incident light absorption from any direction. In the electrolyte, the large active surface area established the photoinduced electrons and these electrons transferred to the substrate. By the use of external circuit, the photoinduced electron travels to counter electrode (platinum electrode) and enhances the photocatalytic activity and photoelectrochemical response significantly.

4. Conclusions

In this paper, nanodisk-dendritic ZnO with perfect hexagonal shape was fabricated by a simple one-step electrodeposition process with 600°C calcination temperature. From the characterization methods, it indicates that the sample is nanodisk-dendritic zinc oxide; with chemical formula, ZnO, and consists of hexagonal crystal system. It lies under tetragonal wurtzite type because $a = 3.2498$ Å, $b = 3.2498$ Å, and $c = 5.2066$ Å. The photocatalytic test (photocurrent density and methyl orange degradation) confirmed that nanodisk-dendritic zinc oxide has excellent photocatalytic activity. Prolonged electrodeposition time or increase of the $ZnCl_2$ concentration may increase the volume of nanodisk-dendritic ZnO and produce better photocatalytic activity.

Conflict of Interests

The authors declare that there is no conflict of interests regarding the publication of this paper.

Acknowledgments

References

[1] United States Environmental Protection Agency (EPA), *Global Warming*, United States Environmental Protection Agency (EPA), 2001.

[2] G. Bond, W. Showers, M. Cheseby et al., "A pervasive millennial-scale cycle in North Atlantic Holocene and glacial climates," *Science*, vol. 278, no. 5341, pp. 1257–1266, 1997.

[3] J.-B. Huang, S.-W. Wang, Y. Luo, Z.-C. Zhao, and X.-Y. Wen, "Debates on the causes of global warming," *Advances in Climate Change Research*, vol. 3, no. 1, pp. 38–44, 2012.

[4] R. J. Devoy, "Sea-level rise: causes, impacts, and scenarios for change," in *Coastal and Marine Hazards, Risks, and Disasters*, pp. 197–241, Elsevier, 2014.

[5] B. Nordell, "Thermal pollution causes global warming," *Global and Planetary Change*, vol. 38, no. 3-4, pp. 305–312, 2003.

[6] J. M. Ogden, "Prospects for building a hydrogen energy infrastructure," *Annual Review of Energy and the Environment*, vol. 24, no. 1, pp. 227–279, 1999.

[7] G. Vijayasarathi, "Alternate energy source using plants instead of photo-voltaic cell—an innovative solution for power crisis," *International Journal of Engineering Research & Technology*, vol. 1, no. 8, pp. 1–6, 2012.

[8] S. Roy and S. Basu, "Improved zinc oxide film for gas sensor applications," *Bulletin of Materials Science*, vol. 25, no. 6, pp. 513–515, 2002.

[9] Y. C. Kong, D. P. Yu, B. Zhang, W. Fang, and S. Q. Feng, "Ultraviolet-emitting ZnO nanowires synthesized by a physical vapor deposition approach," *Applied Physics Letters*, vol. 78, no. 4, pp. 407–409, 2001.

[10] Z. L. Wang, "Zinc oxide nanostructures: growth, properties and applications," *Journal of Physics: Condensed Matter*, vol. 16, no. 25, pp. R829–R858, 2004.

[11] S. Xu and Z. L. Wang, "One-dimensional ZnO nanostructures: solution growth and functional properties," *Nano Research*, vol. 4, no. 11, pp. 1013–1098, 2011.

[12] M. Abd-Ellah, N. Moghimi, L. Zhang et al., "Effect of electrolyte conductivity on controlled electrochemical synthesis of zinc oxide nanotubes and nanorods," *The Journal of Physical Chemistry C*, vol. 117, no. 13, pp. 6794–6799, 2013.

[13] C. J. Lee, T. J. Lee, S. C. Lyu, Y. Zhang, H. Ruh, and H. J. Lee, "Field emission from well-aligned zinc oxide nanowires grown at low temperature," *Applied Physics Letters*, vol. 81, no. 19, pp. 3648–3650, 2002.

[14] J. Zhang, M. Matsuoka, J. Sung Lee, and S. Chen, "Development of visible light-responsive photocatalysts," *International Journal of Photoenergy*, vol. 2012, Article ID 280297, 4 pages, 2012.

[15] X. Y. Zhang, J. Y. Dai, C. H. Lam et al., "Zinc/ZnO core-shell hexagonal nanodisk dendrites and their photoluminescence," *Acta Materialia*, vol. 55, no. 15, pp. 5039–5044, 2007.

[16] Y. Zhang, N. Wang, S. Gao et al., "A simple method to synthesize nanowires," *Chemistry of Materials*, vol. 14, no. 8, pp. 3564–3568, 2002.

[17] J. H. Zeng, B. B. Jin, and Y. F. Wang, "Facet enhanced photocatalytic effect with uniform single-crystalline zinc oxide nanodisks," *Chemical Physics Letters*, vol. 472, no. 1–3, pp. 90–95, 2009.

[18] S.-Y. Guo, S. Han, B. Chi, J. Pu, and J. Li, "Synthesis of shape-controlled mesoporous titanium phosphate nanocrystals: the hexagonal titanium phosphate with enhanced hydrogen generation from water splitting," *International Journal of Hydrogen Energy*, vol. 39, no. 6, pp. 2446–2453, 2014.

[19] Q. Zhang, C. S. Dandeneau, X. Zhou, and C. Cao, "ZnO nanostructures for dye-sensitized solar cells," *Advanced Materials*, vol. 21, no. 41, pp. 4087–4108, 2009.

[20] V. Germain, A. Brioude, D. Ingert, and M. P. Pileni, "Silver nanodisks: size selection via centrifugation and optical properties," *The Journal of Chemical Physics*, vol. 122, no. 12, Article ID 124707, 2005.

[21] C. X. Xu, X. W. Sun, Z. L. Dong, and M. B. Yu, "Zinc oxide nanodisk," *Applied Physics Letters*, vol. 85, no. 17, pp. 3878–3880, 2004.

[22] J. L. G. Fierro, *Metal Oxides: Chemistry and Applications*, CRC Press, 2010.

[23] E. H. Kisi and M. M. Elcombe, "u parameters for the wurtzite structure of ZnS and ZnO using powder neutron diffraction," *Acta Crystallographica—Section C: Crystal Structure Communications*, vol. 45, no. 12, pp. 1867–1870, 1989.

[24] M. O. Manasreh, *III-Nitride Semiconductors: Electrical, Structural and Defects Properties*, Elsevier, Amsterdam, The Netherlands, 2000.

[25] J. Yin, F. Gao, C. Wei, and Q. Lu, "Water amount dependence on morphologies and properties of ZnO nanostructures in double-solvent system," *Scientific Reports*, vol. 4, article 3736, 2014.

[26] G.-R. Li, X.-H. Lu, D.-L. Qu et al., "Electrochemical growth and control of ZnO dendritic structures," *Journal of Physical Chemistry C*, vol. 111, no. 18, pp. 6678–6683, 2007.

[27] B. Boddenberg, "Concepts in physical chemistry," *Zeitschrift für Physikalische Chemie*, vol. 195, part 1-2, pp. 287–289, 1996.

[28] J. M. Barthel, H. Krienke, and W. Kunz, *Physical Chemistry of Electrolyte Solutions: Modern Aspects*, vol. 5, Springer Science & Business Media, 1998.

[29] M. E. Perel'man, G. M. Rubinstein, and V. A. Tatartchenko, "Mechanisms of dendrites occurrence during crystallization: features of the ice crystals formation," *Physics Letters A*, vol. 372, no. 22, pp. 4100–4103, 2008.

[30] J. Xue, W. Liang, X. Liu, Q. Shen, and B. Xu, "Crystallization behavior and formation mechanism of dendrite Cu_2O crystals," *CrystEngComm*, vol. 14, no. 23, pp. 8017–8022, 2012.

[31] M. R. Hoffmann, S. T. Martin, W. Choi, and D. W. Bahnemann, "Environmental applications of semiconductor photocatalysis," *Chemical Reviews*, vol. 95, no. 1, pp. 69–96, 1995.

[32] N. Jain, A. Bhargava, and J. Panwar, "Enhanced photocatalytic degradation of methylene blue using biologically synthesized 'protein-capped' ZnO nanoparticles," *Chemical Engineering Journal*, vol. 243, pp. 549–555, 2014.

[33] S.-M. Lam, J.-C. Sin, A. Z. Abdullah, and A. R. Mohamed, "Degradation of wastewaters containing organic dyes photocatalysed by zinc oxide: a review," *Desalination and Water Treatment*, vol. 41, no. 1–3, pp. 131–169, 2012.

[34] C.-J. Lin, Y.-T. Lu, C.-H. Hsieh, and S.-H. Chien, "Surface modification of highly ordered TiO_2 nanotube arrays for efficient photoelectrocatalytic water splitting," *Applied Physics Letters*, vol. 94, no. 11, Article ID 113102, 2009.

[35] S.-Y. Pung, W.-P. Lee, and A. Aziz, "Kinetic study of organic dye degradation using ZnO particles with different morphologies as a photocatalyst," *International Journal of Inorganic Chemistry*, vol. 2012, Article ID 608183, 9 pages, 2012.

[36] X. Jia, M. Tian, Y. Liu, X. Wu, and H. Song, "In situ precipitation preparation of ZnO hollow spheres and their photocatalysis and gas-sensing properties," *Applied Physics A*, vol. 119, no. 3, pp. 1179–1185, 2015.

[37] S. Licht, B. Wang, S. Mukerji, T. Soga, M. Umeno, and H. Tributsch, "Efficient solar water splitting, exemplified by RuO_2-catalyzed AlGaAs/Si photoelectrolysis," *The Journal of Physical Chemistry B*, vol. 104, no. 38, pp. 8920–8924, 2000.

[38] S. Licht, B. Wang, S. Mukerji, T. Soga, M. Umeno, and H. Tributsch, "Over 18% solar energy conversion to generation of hydrogen fuel; theory and experiment for efficient solar water splitting," *International Journal of Hydrogen Energy*, vol. 26, no. 7, pp. 653–659, 2001.

[39] C. W. Lai and S. Sreekantan, "Photoelectrochemical properties of TiO_2 nanotube arrays: effect of electrolyte pH and annealing temperature," *Journal of Experimental Nanoscience*, vol. 9, no. 3, pp. 230–239, 2014.

[40] K.-S. Ahn, S. Lee, A. C. Dillon, C. E. Tracy, and R. Pitts, "The effect of thermal annealing on photoelectrochemical responses of WO_3 thin films," *Journal of Applied Physics*, vol. 101, no. 9, Article ID 093524, 2007.

Research Article

Fabrication and Characterization of Al/NiO Energetic Nanomultilayers

YiChao Yan, Wei Shi, HongChuan Jiang, Jie Xiong, WanLi Zhang, and Yanrong Li

State Key Laboratory of Electronic Thin Films and Integrated Devices, University of Electronic Science and Technology of China, Chengdu 610054, China

Correspondence should be addressed to Jie Xiong; jiexiong@uestc.edu.cn

The redox reaction between Al and metallic oxide has its advantage compared with intermetallic reaction and Al/NiO nanomutlilayers are a promising candidate for enhancing the performance of energetic igniter. Al/NiO nanomutlilayers with different modulation periods are prepared on alumina substrate by direct current (DC) magnetron sputtering. The thicknesses of each period are 250 nm, 500 nm, 750 nm, 1000 nm, and 1500 nm, respectively, and the total thickness is 3 μm. The X-ray diffraction (XRD) and scanning electron microscope (SEM) results of the as-deposited Al/NiO nanomutlilayers show that the NiO films are amorphous and the layered structures are clearly distinguished. The X-ray photoelectron spectroscopy (XPS) demonstrates that the thickness of Al_2O_3 increases on the side of Al monolayer after annealing at 450°C. The thermal diffusion time becomes greater significantly as the amount of thermal boundary conductance across the interfaces increases with relatively smaller modulation period. Differential scanning calorimeter (DSC) curve suggests that the energy release per unit mass is below the theoretical heat of the reaction due to the nonstoichiometric ratio between Al and NiO and the presence of impurities.

1. Introduction

In recent years, film ignition bridge devices have been widely reported, such as doped polycrystalline silicon [1–4], platinum [5], titanium [6], and chromium bridge [7], which can function in a few tens of microseconds and operate at one-tenth the input energy with over 30 times smaller in volume compared with the hot-wire devices. Thermal plasma is generated to ignite explosive powder by passing current through film bridge. A variety of energetic nanomultilayers, which can provide large negative reaction heats, consist of alternating nanoscale layers of metal or metal oxide such as Al/Ni [8–11], B/Ti [12], Al/CuO [13–15], and Al/MoO$_x$ [16]. In order to improve the transient ignition temperature and output energy, the nanomultilayers integrated on the semiconductor or metal film bridges have been investigated in many research groups. In the discharge mechanism of integrated ignition bridge, thermal plasma generated by the semiconductor or metal film bridges transfers along the nanomultilayers to make atoms diffuse normal to the layers and result in a rapid self-propagating exothermic reactions.

Hence, the integrated structure combines the advantages of film ignition bridge devices and reactive multilayer films, which may improve the ignition performance and reliability in the case of low electrical energy consumption, fast energy release rate, and large amount of reaction heat.

According to the literature [17], the amount of reaction heat released in redox reaction such as Al/CuO, Al/MoO$_x$, and Al/NiO is almost two times than that of intermetallic reaction. In addition, Al/NiO nanomultilayer redox reaction shows its advantage among the vast range of Al/metallic oxide reactions, which have been confirmed by the investigation of Al/metallic oxide nanocomposites such as nanowire [18, 19] and nanohoneycomb [20]. The various oxidation state of nickel in nickel oxides is an important parameter for released reaction heat. A number of nickel oxides with various oxidation states of nickel such as NiO, NiO_2, Ni_2O_3, Ni_3O_4, and NiO_4 have been reported, showing that the presence of nickel cation vacancy or interstitial oxygen in NiO crystalline lattice results in nonstoichiometric NiO$_x$.

It is well known that the coefficient of heat conduction, elements diffusivity, and grain boundary in nanomultilayers
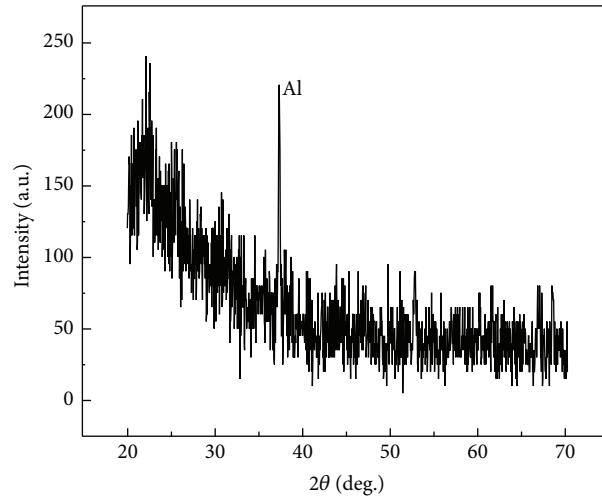
FIGURE 1: XRD spectrum of Al/NiO nanomultilayers with modulation period thickness of 1500 nm where the thickness ratio of Al to NiO per period is maintained at 1 : 1.5.

are mainly influenced by the film interfaces existing in nanomultilayers and deposition conditions, which can enhance the interfacial contact area. In this study, we focus on the preparation and characterization of the Al/NiO nanomultilayers with different modulation periods. The fabricated Al/NiO nanomultilayers are characterized by X-ray diffraction (XRD), scanning electron microscopy (SEM), X-ray photoelectron spectroscopy (XPS), ultrafast measurement system of thermal properties of thin film materials, and differential scanning calorimetry (DSC).

2. Experimental

Al and NiO films are sputter-deposited from Al (purity > 99.99%) and Ni (purity > 99.95%) targets of diameter 50 mm on alumina substrate (10 mm × 5 mm × 0.5 mm) in a multilayer form by direct current (DC) magnetron sputtering and DC reactive magnetron sputtering, respectively. Before deposition, the substrates are cleaned using acetone, alcohol, and deionized water in an ultrasonic bath for 10 min, respectively, which subsequently are dried by nitrogen gas and placed in the oven at 200°C for 20 min for further drying. The substrates move alternately under the afterglow from sputtered Al and Ni targets through a shield with optimized shape to allow for homogeneous film, where the distance between target and substrate is 60 mm. The sputtering power is fixed at 100 W for Al and Ni targets. In addition, the Al target is sputtered under argon ambient and the Ni target is sputtered under argon and oxygen ambient with argon partial pressure at 1.5 Pa and oxygen partial pressure at 0.25 Pa in order to obtain amorphous NiO film. After NiO monolayer is deposited at a time, the work gas argon and reactive gas oxygen in the chamber are pumped out completely to remove oxygen for preventing alumina. The base pressure is 4×10^{-4} Pa and the substrate temperature remains at room temperature in order to prevent the interdiffusion and reaction during deposition. The growth rates of Al monolayer

and NiO monolayer are a calculation of monolayer thickness divided by deposition time. The thickness ratio of Al to NiO per period is maintained at 1 : 1.5 to obtain final products with alumina and metal nickel. The total thickness of Al/NiO nanomultilayers is 3 μm with NiO monolayer on the bottom and Al monolayer on the top and the thicknesses of each period keep at 250 nm, 500 nm, 750 nm, 1000 nm, and 1500 nm, respectively.

The crystallographic structure of Al/NiO nanomultilayers is determined by Bede D1 XRD using Cu Ka radiation. The cross-sectional and top-view morphologies are performed using a JEOL-7500F SEM. The diffusion process is confirmed after postdeposition annealing at 450°C in flow argon gas using XPS (Axis Ultra DLD, Kratos Analytical Ltd.). The scanning pass energy is 40 eV and the step size is 0.1 eV. Ultrafast measurement system of thermal properties of thin film materials (NanoTR, PicoTherm) is performed to qualify the influence of the interfaces on the characteristic of heat conduction at room temperature with laser pulse width 1 ns and laser wavelength 1550 nm. The sample surface is coated with a thin molybdenum monolayer with thickness 100 nm so that the change in reflectivity of the sample surface is an indication of the change in temperature of the Al/NiO nanomultilayers. The onset temperatures and energy release values are investigated by DSC, the samples for DSC analysis are scraped from the substrates with a sharp blade, and the DSC experiment is carried out at a temperature range from 20 to 850°C at a heating rate of 5°C/min under a N_2 flow with a sample mass of 12 mg.

3. Results and Discussion

The XRD spectrum of the as-deposited Al/NiO nanomultilayers with modulation period thickness of 1500 nm is shown in Figure 1; metal Al diffraction peak can be clearly seen from the XRD spectrum. There are no peaks for metal Ni or NiO, indicating that the metal Ni is completely oxidized into

(a)   (b)
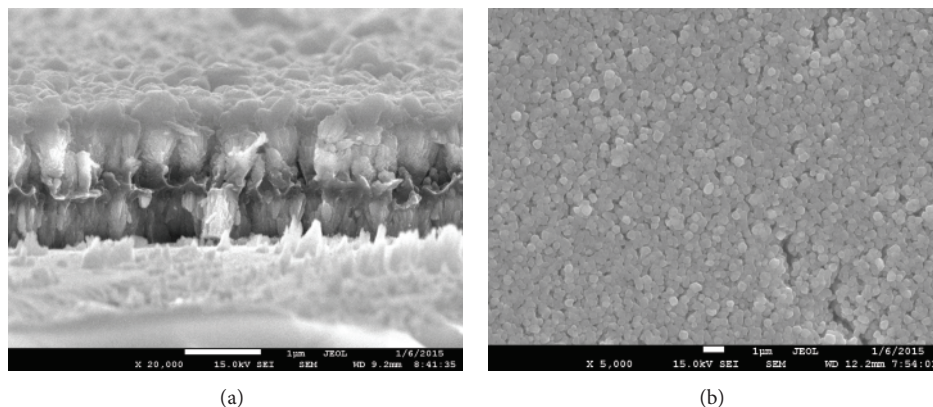
FIGURE 2: The cross-sectional (a) and top-view (b) SEM morphologies of Al/NiO nanomultilayer with modulation period thickness of 1500 nm.

amorphous NiO. Although there are no peaks for the Al_2O_3 in the XRD spectrum, part of the metal Al on the top surface of Al/NiO nanomultilayers is oxidized as the amorphous Al_2O_3, which is confirmed by SEM and XPS analysis in Figures 2 and 3. This means that the redox reaction between metal Al and NiO has not happened for as-deposited Al/NiO nanomultilayers, ascribing to the deposition condition of room temperature.

Figure 2 shows cross-sectional and top-view SEM morphologies of Al/NiO nanomultilayer with modulation thickness of 1500 nm. All the monolayers exhibit a columnar structure with the growth direction perpendicular to the interfaces alternately. As can be seen in the figure, the layered structures of Al/NiO nanomultilayers are clearly distinguished and the interfaces are sharp. As described previously, there is an obvious Al_2O_3 oxide layer on the top of Al monolayer. It can be identified that the diameters of the grain on multilayer surface are relatively not uniform because of oxidized metal Al surface.

The XPS spectra in Figure 3 indicate the presence of Al, Ni, O, and some organic contamination on the top of nanomultilayers. It can be observed that there is an obvious Al_2O_3 layer at the surface in the range of 1-2 nm in Figure 3(a). The Ni atoms are also detected in the as-deposited nanomultilayers; this means that only a small number of Ni atoms are not oxidized and diffuse into Al monolayer on the top; this is because the melting point of Ni is higher than that of Al, making it much easier for Ni atoms to diffuse into Al lattice due to the weaker bonds between Al atoms. After annealing at 450°C, when more oxygen atoms diffuse into Al monolayer significantly, the thickness of Al_2O_3 layer increases and much larger amount of Ni atoms accumulates at the surface as can be seen in Figure 3(b), indicating that redox reaction has happened and more metal Al is oxidized.

The change in thermoreflectivity of the sample surface in Figure 4 is an indication of the change in temperature of the Al/NiO nanomultilayers as described previously. The characteristic of heat conduction is determined by thermal diffusion time in monolayer film model where the heat diffuses from the surface to the substrate. Thermal diffusion time with different modulation thicknesses at 1500 nm,

1000 nm, 750 nm, 500 nm, and 250 nm is 5×10^{-9} s, 8×10^{-8} s, 9.6×10^{-8} s, 1.1×10^{-7} s, and 1.4×10^{-7} s, respectively. The amount of the interfaces between Al monolayer and NiO monolayer increases as the modulation period decreases, which indicates that the amount of the thermal boundary conductance across the interfaces increases and the thermal diffusion time becomes greater significantly. In addition, there is much smaller change in the rate of reduction of thermal diffusion time with increased interfaces.

Figure 5 shows the DSC data measured from Al/NiO nanomultilayers with modulation period thickness of 250 nm. The first exotherm is not easily distinguished starting at around 460°C and the second one is with an onset temperature of about 566°C, where the energy generation from the redox reaction is clearly visible and it reacts before the metal Al melts, suggesting the solid-solid diffusion reaction mechanism. There is a sharply rising endothermic peak at 635°C as the metal Al begins to melt; the remaining Al reacts with NiO by the liquid-solid diffusion mechanism with an onset temperature of about 812°C. The area integration of exotherm with an onset temperature of about 566°C based on the heat flow curve provides the energy release per unit mass of 2440 J/g, which is below the theoretical heat of the reaction (3440 J/g); this could be because the masses between Al and NiO are at nonstoichiometric ratio and the deposition process results in the presence of impurities and the oxidized Al on the surface. In addition, the smaller modulation period nanomultilayers can enhance the interfacial contact area and surface area, which will reduce the onset temperature and increase energy output of nanomultilayers. From this point of view, the nanomultilayers with much smaller modulation period are more suitable for energetic igniter.

4. Conclusions

The technique of integrating nanomultilayers on the semiconductor or metal film ignition bridge has been proven to be an effective approach for increasing the output energy in a short time. Al/NiO nanomultilayers with different modulation thicknesses of 250 nm, 500 nm, 750 nm, 1000 nm,
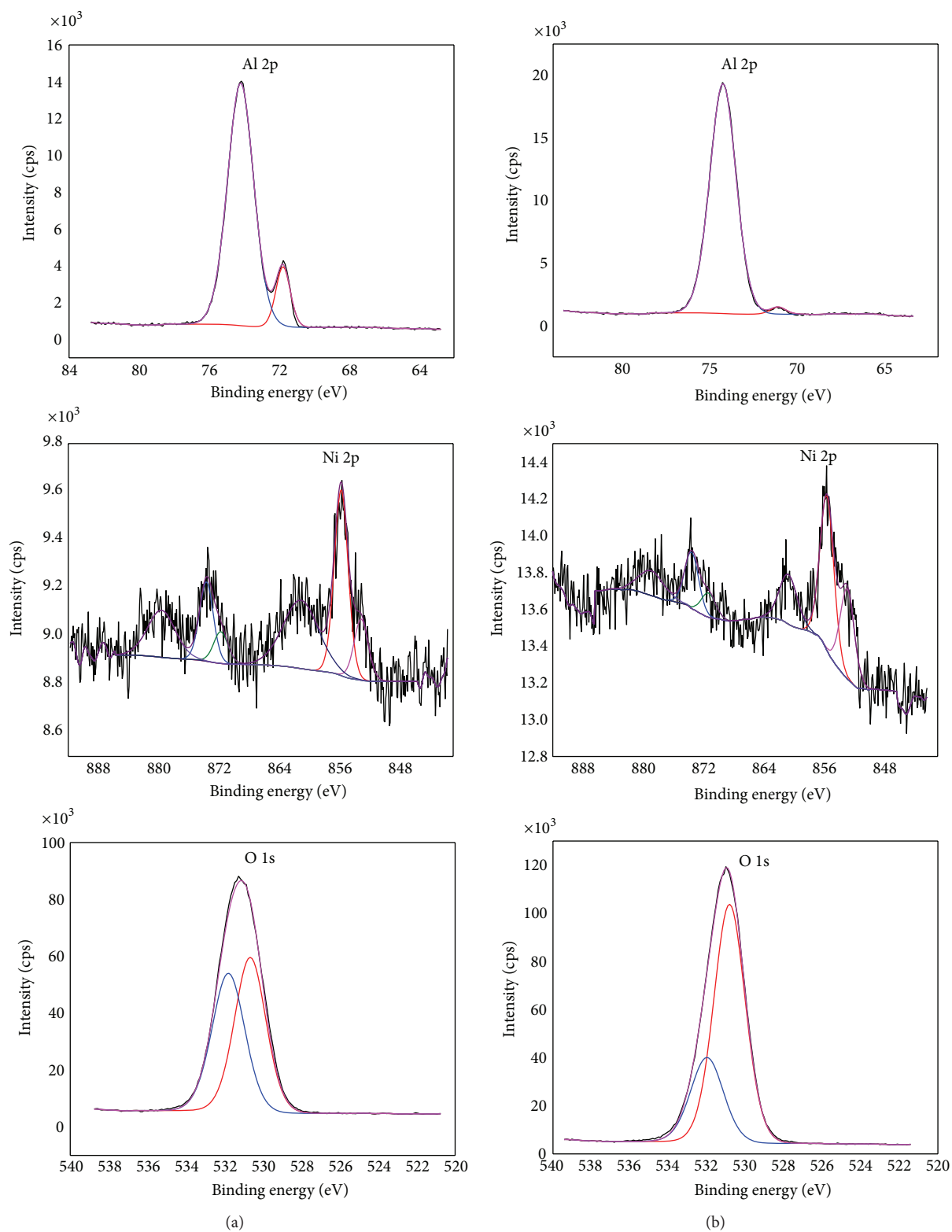
Figure 3: XPS spectra of Al/NiO nanomultilayers with modulation period thickness of 250 nm: (a) the up, middle, and down spectra show Al 2p, Ni 2p, and O 1s peaks of as-deposited nanomultilayers, respectively; (b) the up, middle, and down spectra show Al 2p, Ni 2p, and O 1s peaks of annealed nanomultilayers at 450°C, respectively.
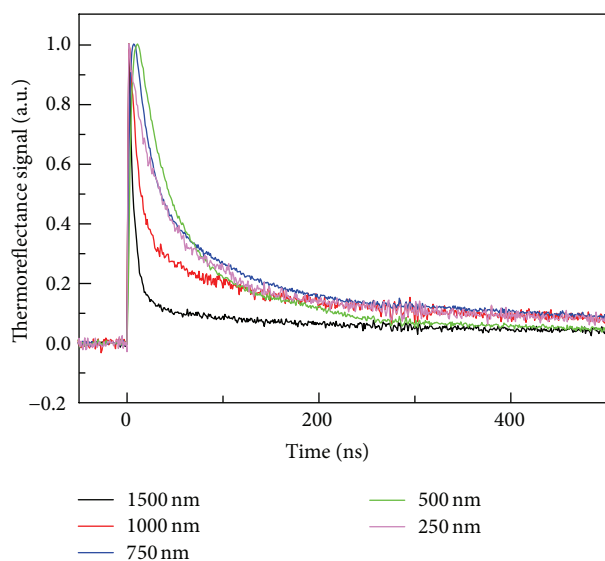
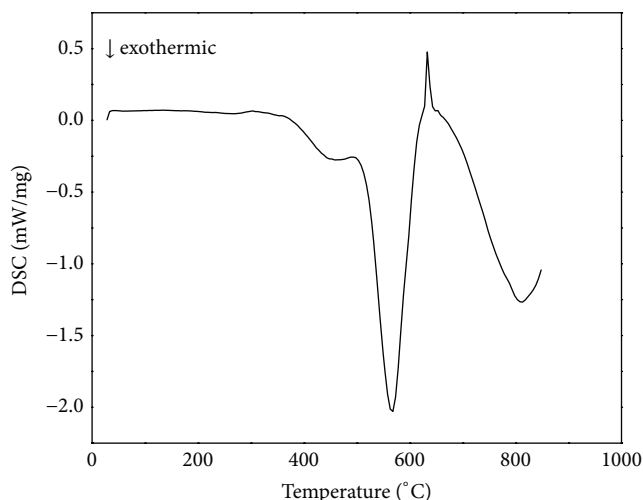FIGURE 4: The characteristic of heat conduction of Al/NiO nanomultilayers with different modulation periods.

FIGURE 5: DSC curve of Al/NiO nanomultilayers with modulation period thickness of 250 nm.

by standard microfabrication techniques that allow batch fabrication and high level of integration.

Conflict of Interests

The authors declare that there is no conflict of interests regarding the publication of this paper.

Acknowledgment

References

[1] D. A. Benson, M. E. Larsen, A. M. Renlund, W. M. Trott, and R. W. Bickes Jr., "Semiconductor bridge: a plasma generator for the ignition of explosives," *Journal of Applied Physics*, vol. 62, no. 5, pp. 1622–1632, 1987.

[2] J.-U. Kim, C.-O. Park, M.-I. Park, S.-H. Kim, and J.-B. Lee, "Characteristics of semiconductor bridge (SCB) plasma generated in a micro-electro-mechanical system (MEMS)," *Physics Letters, Section A: General, Atomic and Solid State Physics*, vol. 305, no. 6, pp. 413–418, 2002.

[3] M.-I. Park, H.-T. Choo, S.-H. Yoon, and C.-O. Park, "Comparison of plasma generation behaviors between a single crystal semiconductor bridge (single-SCB) and a polysilicon semiconductor bridge (poly-SCB)," *Sensors and Actuators A: Physical*, vol. 115, no. 1, pp. 104–108, 2004.

[4] K.-N. Lee, M.-I. Park, S.-H. Choi, C.-O. Park, and H. S. Uhm, "Characteristics of plasma generated by polysilicon semiconductor bridge (SCB)," *Sensors and Actuators A: Physical*, vol. 96, no. 2-3, pp. 252–257, 2002.

[5] G. F. Zhang, Z. You, S. Q. Hu, B. X. Li, and B. X. Wang, "MEMS-based propulsion arrays with solid propellant," *Journal of Tsinghua University (Science and Technology)*, vol. 44, no. 11, pp. 1489–1492, 2004.

[6] K. L. Zhang, S. K. Chou, S. S. Ang, and X. S. Tang, "A MEMS-based solid propellant microthruster with Au/Ti igniter," *Sensors and Actuators, A: Physical*, vol. 122, no. 1, pp. 113–123, 2005.

[7] X. Z. Wu, P. T. Dong, Z. Z. Li et al., "Design, fabrication and characterization of a solid propellant micro-thruster," in *Proceedings of the 4th IEEE International Conference on Nano/Micro Engineered and Molecular Systems (NEMS '09)*, pp. 476–479, January 2009.

[8] A. J. Gavens, D. Van Heerden, A. B. Mann, M. E. Reiss, and T. P. Weihs, "Effect of intermixing on self-propagating exothermic reactions in Al/Ni nanolaminate foils," *Journal of Applied Physics*, vol. 87, no. 3, pp. 1255–1263, 2000.

[9] R. Knepper, M. R. Snyder, G. Fritz, K. Fisher, O. M. Knio, and T. P. Weihs, "Effect of varying bilayer spacing distribution on reaction heat and velocity in reactive Al/Ni multilayers," *Journal of Applied Physics*, vol. 105, no. 8, Article ID 083504, 2009.

[10] S. Simões, F. Viana, A. S. Ramos, M. T. Vieira, and M. F. Vieira, "Anisothermal solid-state reactions of Ni/Al nanometric multilayers," *Intermetallics*, vol. 19, no. 3, pp. 350–356, 2011.

[11] M. Swain, S. Singh, S. Basu, and M. Gupta, "Effect of interface morphology on intermetallics formation upon annealing of Al-Ni multilayer," *Journal of Alloys and Compounds*, vol. 576, pp. 257–261, 2013.

and 1500 nm are successfully prepared, showing the clearly layered. The XPS result indicates that the thickness of Al_2O_3 increases at the monolayer of Al after annealing at $450°C$. The thermal diffusion time becomes greater significantly as the amount of thermal boundary conductance across the interfaces increases with relatively smaller modulation period. DSC curve suggests that the reaction is based on the solid-solid diffusion mechanism at the early stage and the energy release per unit mass is below the theoretical heat of the reaction due to the nonstoichiometric ratio between Al and NiO and the presence of impurities. In general, the parameters including thermal diffusion time, onset temperature, and energy release need an overall consideration and a continuously optimized fabrication process. It should be noted that Al/NiO nanomultilayers could be realized

[12] S. Tanaka, K. Kondo, H. Habu et al., "Test of B/Ti multilayer reactive igniters for a micro solid rocket array thruster," *Sensors and Actuators A: Physical*, vol. 144, no. 2, pp. 361–366, 2008.

[13] K. J. Blobaum, M. E. Reiss, J. M. Plitzko, and T. P. Weihs, "Deposition and characterization of a self-propagating CuO_x/Al thermite reaction in a multilayer foil geometry," *Journal of Applied Physics*, vol. 94, no. 5, pp. 2915–2922, 2003.

[14] K. J. Blobaum, A. J. Wagner, J. M. Plitzko, D. van Heerden, D. H. Fairbrother, and T. P. Weihs, "Investigating the reaction path and growth kinetics in CuO_x/Al multilayer foils," *Journal of Applied Physics*, vol. 94, no. 5, pp. 2923–2929, 2003.

[15] K. L. Zhang, C. Rossi, M. Petrantoni, and N. Mauran, "A nano initiator realized by integrating Al/CuO-based nanoenergetic materials with a Au/Pt/Cr microheater," *Journal of Microelectromechanical Systems*, vol. 17, no. 4, pp. 832–836, 2008.

[16] S. Fu, Y. Zhu, D. l. Li et al., "Deposition and characterization of highly energetic Al/MoO_x multilayer nano-films," *European Physical Journal—Applied Physics*, vol. 64, no. 3, Article ID 30301, 2013.

[17] S. H. Fischer and M. C. Grubelich, "Theoretical energy release of thermites, intermetallics and combustible metals," in *Proceedings of the 24th International Pyrotechnics Seminar*, Monterey, Calif, USA, July 1998.

[18] G. Bohlouli-Zanjani, J. Z. Wen, A. Hu, J. Persic, S. Ringuette, and Y. N. Zhou, "Thermo-chemical characterization of a Al nanoparticle and NiO nanowire composite modified by Cu powder," *Thermochimica Acta*, vol. 572, pp. 51–58, 2013.

[19] J. Z. Wen, S. Ringuette, G. Bohlouli-Zanjani et al., "Characterization of thermochemical properties of AL nanoparticle and NiO nanowire composites," *Nanoscale Research Letters*, vol. 8, article 184, 2013.

[20] K. L. Zhang, C. Rossi, P. Alphonse, C. Tenailleau, S. Cayez, and J.-Y. Chane-Ching, "Integrating Al with NiO nano honeycomb to realize an energetic material on silicon substrate," *Applied Physics A: Materials Science and Processing*, vol. 94, no. 4, pp. 957–962, 2009.

Research Article

Strain Driven Phase Decomposition in Ion-Beam Sputtered $Pr_{1-X}Ca_XMnO_3$ Films

Benedikt Ifland, Joerg Hoffmann, Thilo Kramer, Malte Scherff, Stephanie Mildner, and Christian Jooss

Institute of Materials Physics, University of Goettingen, Friedrich-Hund-Platz 1, 37077 Goettingen, Germany

Correspondence should be addressed to Christian Jooss; jooss@material.physik.uni-goettingen.de

The deposition of heteroepitaxial thin films on single crystalline substrates by means of physical deposition methods is commonly accompanied by mechanical strain due to lattice mismatch and defect generation. Here we present a detailed analysis of the influence of strain on the Mn solubility of $Pr_{1-X}Ca_XMnO_3$ thin films prepared by ion-beam sputtering. Combining results from X-ray diffraction, transmission electron microscopy and in situ hot-stage stress measurements, we give strong evidence that large tensile strain during deposition limits the Mn solubility range of the Perovskite phase to near-stoichiometric composition. Mn excess gives rise to MnO_z precipitates and the precipitation seems to represent a stress relaxation path. With respect to size and density of the precipitates, the relaxation process can be affected by the choice of substrate and the deposition parameters, that is, the deposition temperature and the used sputter gas.

1. Introduction

$Pr_{1-X}Ca_XMnO_3$ (PCMO) belongs to the class of Perovskite-type oxides with the general formula ABO_3 which exhibit rich and fascinating electronic and magnetic properties. These properties can be tailored via doping. In the case of the hole-doped PCMO, the replacement of rare-earth element Pr on the A-sites by the alkaline-earth element Ca gives rise to a series of different electronic and magnetic ground states. Above $X = 0.3$, charge ordered phases are observed which show colossal resistance effects in external fields such as the colossal magnetoresistance (CMR) [1].

These remarkable properties are sensitively related to the subtle balance between the interactions of spin, lattice, charge, and orbital degrees of freedom which can dramatically change due to defects and strain. Small changes in bonding angles or bonding lengths of the octahedral tilt system can significantly alter the transfer integral [2] and therefore the magnetic exchange interactions and charge carrier mobility [3]. Consequently, without taking into account lattice disorder and stress-strain state, the understanding of

structure-property relations of manganite thin films is hardly possible.

Strain appears in heteroepitaxially grown thin films due to the lattice mismatch (difference in lattice constants) and the thermal mismatch (difference in thermal expansion coefficients) between the substrate and the film. The effect of strain on charge ordering and the CMR in PCMO have been indeed observed in many studies [4–6].

In addition to lattice and thermal mismatch, the strain state of thin films is influenced by preparation induced defects. Sputter deposition of oxide films is commonly accompanied by the formation and annihilation of point-like intrinsic defects (e.g., Schottky defects) or nonstoichiometric defects (e.g., oxygen vacancies). Such defects can change the global lattice constant and can induce local disorder in the octahedral tilt system. Nonstoichiometric defects can also change the doping level. The role of electron-doping oxygen vacancies and A-site as well as B-site cation deficiencies in transport and magnetic properties has been, for example, studied in [7, 8].
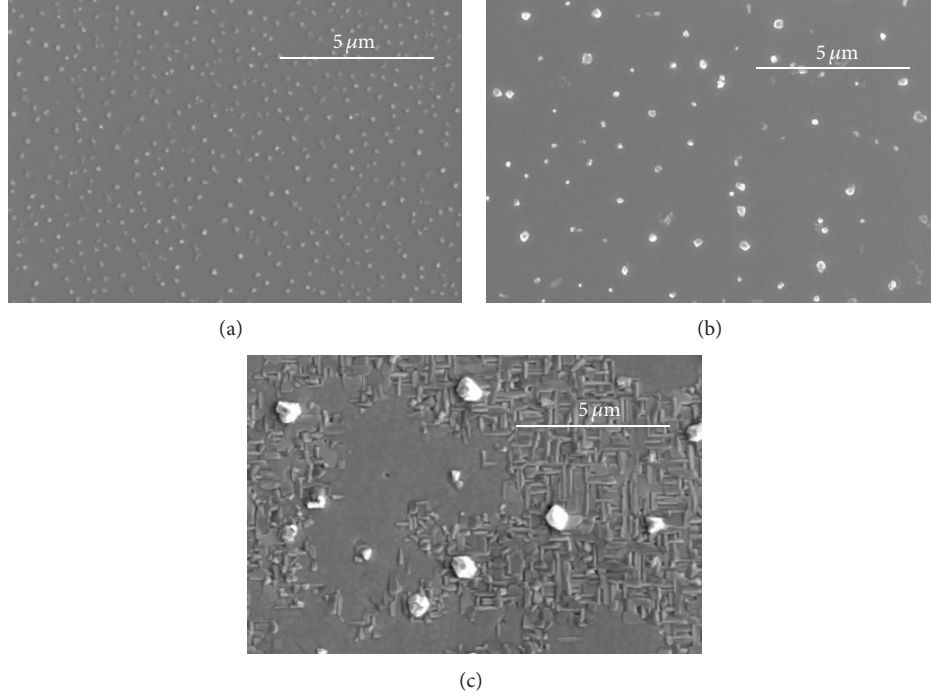
(a)

(b)

(c)

Figure 1: SEM pictures of three PCMO samples with $X \approx 0.3$ and an A-to-B site ratio close to 1 ($\delta \approx 0$) on different substrates: (a) STO (sample F03_1a), (b) MgO (sample E03_1), and (c) epitaxially grown Pt film on MgO (sample B03_1). The main parameters of these samples are summarized in Table 1.

In this contribution, we focus on a further important aspect of strain, that is, its effect on the appearance of crystallographic phases and solubility ranges which can induce pronounced differences to the equilibrium bulk phase diagram (e.g. [9]). Well-known examples for the change of solubility ranges are the strong increase of the Hydrogen solubility in Niobium thin film samples [10] and stress-induced precipitations of a second phase in semiconductors [11] and highly deformed metal alloys (e.g. [12]).
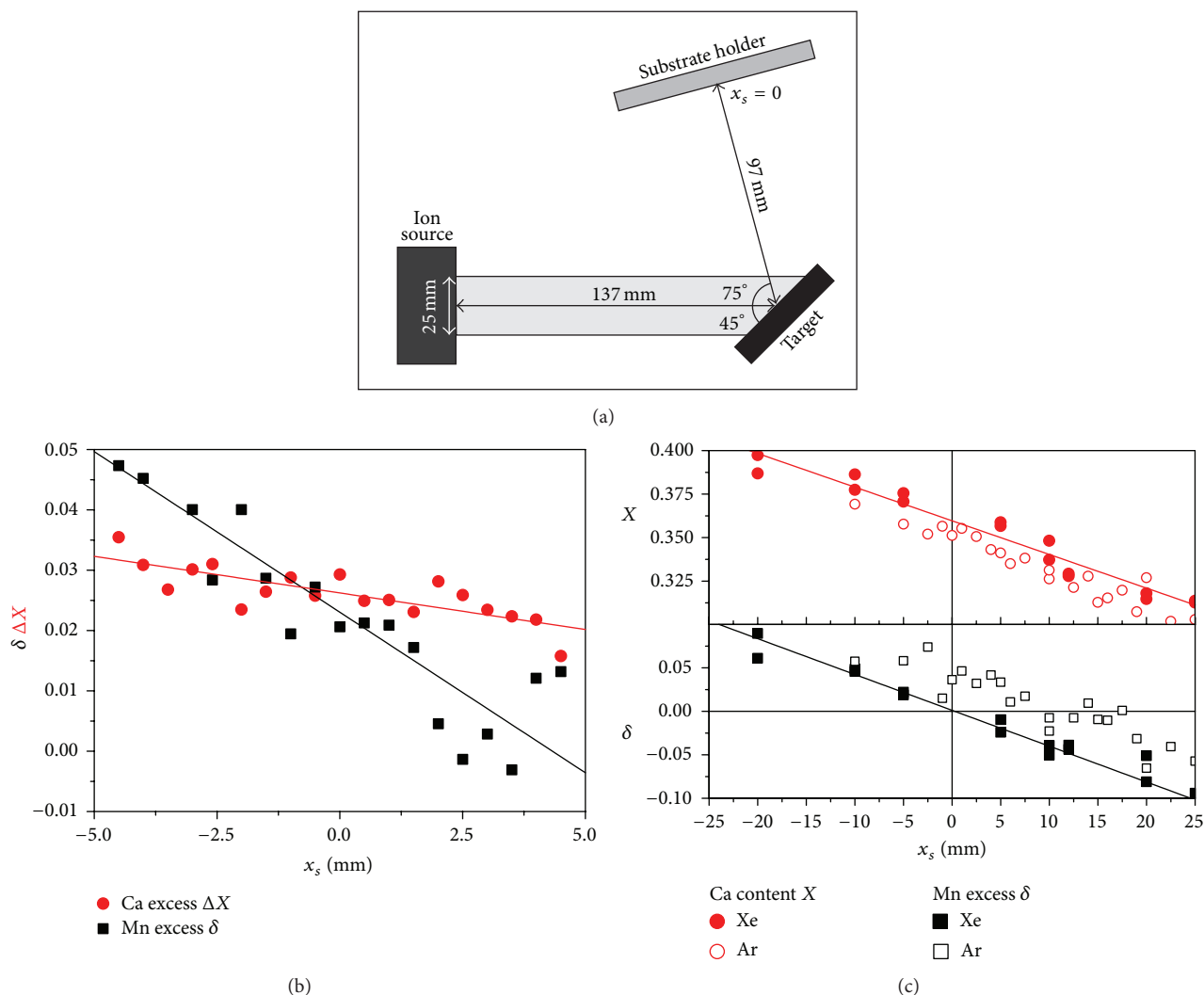
We show that a strain-induced precipitation of the nonequilibrium MnO_z phases takes place in ion-beam sputter (IBS) deposited PCMO thin films with near-stoichiometric composition. In contrast to film deposition by pulsed-laser deposition, where the strain strongly relaxes with increasing film thickness [4], films prepared by IBS remain in a highly strained state up to thicknesses of the order of 500 nm. The precipitation in these films takes place over the whole nominal hole-doping range from $X = 0$ to 0.5 and gives rise to the generation of growth disturbances (Figure 1). In order to investigate the influence of lattice mismatch and defect formation on the precipitation, we have used three different substrates (SrTiO$_3$ (STO), MgO, and Pt-coated MgO) and two different working gases (Xe and Ar). Although the nominal mismatch of PCMO to the used substrates is tensile which would give rise to compressive out-of-plane strain, the experimentally observed strain state at room temperature is quite different. Depending on the exact deposition parameters, PCMO films commonly reveal out-of-plane strains in the range from −0.3% to −1.2% on STO, from +0.3% to +1% on MgO, and from −0.5% to +0.4% on Pt-coated MgO. The discrepancy between nominal lattice mismatch and strain state is due to lattice expansion by preparation induced point defects and stress relaxation which eventually poses strong bounds to the upper Mn solubility limit.

2. Materials and Methods

Figure 2(a) shows schematically the ion-beam sputter set-up. The Kaufman source (2.5 cm beam diameter, Ion Tech Inc.) generates a noble gas (Ar or Xe) ion beam with a small divergence which is directed onto the target. The outgoing ion beam is neutralized by an electron emitting Ar plasma source, enabling sputtering of metallic as well as dielectric compounds. In our experiments, the beam current density and the beam voltage were fixed (4 mA/cm^2/1000 V). During deposition, the background pressure of impurity gases amounts to about 10^{-7} mbar. The partial pressures are $p_{Ar} = 3 \times 10^{-4}$ mbar for neutralization and sputtering with Ar ions with an additional Xe inlet of $p_{Xe} = 1 \times 10^{-4}$ mbar in the case of Xe sputtering. In order to enable nearly stoichiometric oxygen content in the films, an oxygen inlet corresponding to $p_{O_2} = 1.4 \times 10^{-4}$ mbar is supplied. Unless otherwise stated, the deposition temperatures T_s (on top of the substrate) were $T_s = 750°C$ or $T_s = 800°C$.

The sputter targets were prepared by a repeating milling and calcination process starting from mixture of Pr$_6$O$_{11}$, CaCO$_3$, and Mn$_2$O$_3$ powders. According to Pr$_{1-X}$Ca$_X$Mn$_{1+\delta}$, the composition of targets and films is characterized by the Ca content (X_{target} and X) and the Mn excess (δ_{target} and δ),

FIGURE 2: (a) Scheme of an ion-beam sputtering device with Kaufman source, target, and substrate holder. (b) Variation of the Mn excess (Pr, Ca)$_1$Mn$_{1+\delta}$ and Ca excess $\Delta X = X - X_{\text{target}}$ along the substrate holder (lateral position x_s). The nominal composition of the target corresponds to $\delta = 0$ and $X_{\text{target}} = 0.28$. A 1.9 μm thick film was deposited at $T_s = 800°$C on MgO in order to measure the composition by means of microprobe. (c) Variation of the Mn excess (Pr, Ca)$_1$Mn$_{1+\delta}$ and Ca content X along the substrate holder for 300 nm thick films prepared from the off-stoichiometric target with nominal composition $\delta = -0.02$ and $X_{\text{target}} = 0.34$. Solid symbols correspond to Xe and open symbols correspond to Ar as sputter gas. The composition was measured by means of EDX including a thin film correction.

where X and δ are the determined values of the thin films. We have used targets with $X_{\text{target}} = 0, 0.28, 0.34, 0.5$ and $\delta_{\text{target}} = 0$ as well as one off-stoichiometric target with $X_{\text{target}} = 0.34$ and $\delta_{\text{target}} = -0.02$. The main parameters of the film samples are summarized in Table 1. Single crystalline (100) SrTiO$_3$ (STO) and (100) MgO and almost single crystalline (100) Pt films on MgO (Pt-MgO) were used as substrates. The size of the substrates is $5 \times 10 \times 1$ mm. The epitaxial 300 nm thick Pt films were deposited via IBS at $T_s = 750°$C.

X-ray diffraction (XRD) studies of θ-2θ scans were carried out with a Bruker D8 Discover system with Cu K$_\alpha$ radiation ($\lambda = 0.15418$ nm). The film composition was determined by means of Energy Dispersive X-Ray Analysis (EDX, AN 10000, Link) incorporated in a Scanning Electron Microscope (SEM, Stereoscan 360, Cambridge Instruments)

and by microprobe (JEOL 8900 RL electron probe microanalyzer). For surface topology investigations, we have used a FEI Nova NanoSEM and a Nova Nano Lab 600 SEM. The latter is equipped with a Focused Ion Beam (FIB) etching device, allowing the preparation of electron-transparent lamellas for cross-sectional transmission electron microscopy (TEM) investigations. The TEM investigations were performed in a Phillips CM12 and in a FEI Titan 300 keV equipped with an Electron Energy Loss Spectrometer (EELS) Gatan Quantum ER/965P. EDX measurement on TEM samples was done in the CM12 with a Si drift detector from Oxford with an energy resolution of 136 eV.

We have also measured the stress evolution of the PCMO films during high-temperature deposition on STO and Pt-coated MgO substrates by using a SIG-2000SP system from

TABLE 1: Ca content X, Mn excess δ, substrate type, used sputter gas and thickness d_f of the different samples, and the deposition temperature T_s. Samples with the same capital letter but different numbers were prepared in the same deposition run. Small letters indicate that samples were prepared at the same lateral position x_s but at different vertical positions y_s. Therefore, composition and thickness of these samples are equal.

Sample	X	δ	Substrate	Sputter gas	d_f [nm]	T_s [°C]
A0_1	0	0	STO	Xe	410	675
B03_1	0.3	0	Pt/MgO	Xe	300	800
C03_1	0.35	0	STNO	Xe	110	800
D03_1a	0.33	0	STO	Ar	175	750
D03_1b	0.33	0	MgO	Ar	175	750
E03_1	0.35	0	MgO	Xe	300	800
F03_1a	0.36	0	STO	Xe	130	750
F03_1b	0.36	0	MgO	Xe	130	750
G03_1	0.35	−0.02	STO	Xe	165	750
H05_1	0.5	0	Pt/MgO	Xe	380	800

Sigma-Physik Messtechnik. Deposition of a stressed film on single-side clamped bar-shaped substrates (3 mm × 15 mm × 0.1 mm) gives rise to a bending of the substrate with increasing film thickness. This bending is monitored by the change of distance between two laser spots being reflected from the substrate to the detector. The thickness dependent stress can be then calculated from Stoney's formula [13].

3. Results

Ion-beam sputtering takes place at a very low total pressure. Since the ejection angle of the individual target-forming elements (Pr, Ca, and Mn) is different [14] and scattering in the gas phase is almost negligible, the composition of the deposited film varies with the position along the substrate holder x_s. A typical example of this variation in composition is shown in Figure 2(b). The measurement has been performed by microprobe on a 1.9 μm thick film, where no thin film corrections are required. The Ca content X as well as the Mn excess δ varies almost linearly with the position on the substrate holder, but the film composition does not reach the target composition. It should be noted that the concentration does not significantly vary perpendicular to the x_s direction; that is, in the vertical y_s direction the homogeneity range amounts to about 15 mm. Therefore, it is possible to prepare two films with the same composition in one run (see also caption of Table 1).

Figure 2(c) shows that the Ca content and the A-to-B site ratio depends on the used sputter gas, that is, Xe or Ar. The film compositions across the sample holder were measured by EDX on about 300 nm thick film sample. We have also performed a comparison between EDX and microprobe analysis. Within the scattering of the data, the slope of the concentration profiles (Ca content, Mn excess) is equal for both methods. However, most probably due to the limited energy resolution, EDX measurement reveals a slightly lower Mn content and a higher Ca content than

TABLE 2: Lattice parameters a, b, and c for $Pr_{1-X}Ca_X MnO_3$ (a) according to [15]. $\langle a_{pc} \rangle$ is defined as the mean value of the pseudocubic lattice constant, that is, the mean value of $a/\sqrt{2}$, $b/\sqrt{2}$ and $c/2$. The lattice mismatch to STO, Pt, and MgO deduced from the pseudocubic lattice constant is also included using $a_{STO} = 0.3905$ nm, $a_{Pt} = 0.3923$ nm, and $a_{MgO} = 0.4213$ nm. We have also used the atom positions in the unit cell from [15] to calculate the intensity ratios by means of the CaRIne software (b).

(a)

X	a [nm]	b [nm]	c [nm]	$\langle a_{pc} \rangle$ [nm]	Δ_{STO} [%]	Δ_{Pt} [%]	Δ_{MgO} [%]
0.0	0.5445	0.5809	0.7585	0.3917	0.30	−0.16	−7.03
0.2	0.5442	0.5552	0.7657	0.3867	−0.96	−1.42	−8.20
0.3	0.5426	0.5478	0.7679	0.3850	−1.41	−1.86	−8.62
0.4	0.5415	0.5438	0.7664	0.3835	−1.78	−2.23	−8.96
0.5	0.5395	0.5430	0.7612	0.3814	−2.34	−2.78	−9.48

(b)

(hkl)	d_{hkl} [nm]	I [%]
(112)	0.2720	100.0
(200)	0.2713	44.9
(220)	0.1928	13.7
(004)	0.1920	13.4

microprobe analysis. In the following, we use the EDX results. Therefore, we may underestimate δ by an amount of 0.02 and overestimate X by 0.028.

PCMO films prepared by ion-beam sputtering reveal the commonly observed epitaxial relations between the deposited films and all three underlying cubic substrates. Using the Pbnm notation for PCMO, two different growth directions are observed:

$$[001] \,//\, PCMO\ [001]\ \text{and}\ [001] \,//\, PCMO\ [110]$$

In-plane, the a and b directions of (001)-grown PCMO are aligned along the $\langle 110 \rangle$ directions of the substrate while the c-direction of (110)-grown domains is aligned along the $\langle 100 \rangle$ and $\langle 010 \rangle$ directions. Additional exchange of a and b directions gives rise to all in all six different twin domains. As a reference for samples with different Ca contents, we are using the Pbnm bulk lattice parameters determined by Jirak et al. [15]. These parameters and the most relevant reflection intensities are summarized in Table 2.

The Ca content, the substrate choice, and the exact deposition conditions only influence the volume fractions of the misorientations and the twin domains. PMO films ($X = 0$) on STO reveal no misorientations and the dominating growth direction is $\langle 110 \rangle$ for samples deposited at $T_s \geq 750$°C. A preferred [001] growth direction is only observed for lower deposition temperatures (Figure 3(a)).

Figure 3(b) shows an overview of XRD scans for two samples with a Ca content of $X = 0.36$ and Mn excess of $\delta \approx 0$ prepared both on STO (top) and on MgO (bottom) in the same deposition run. In contrast to PMO, the two growth directions are almost indistinguishable in XRD because the
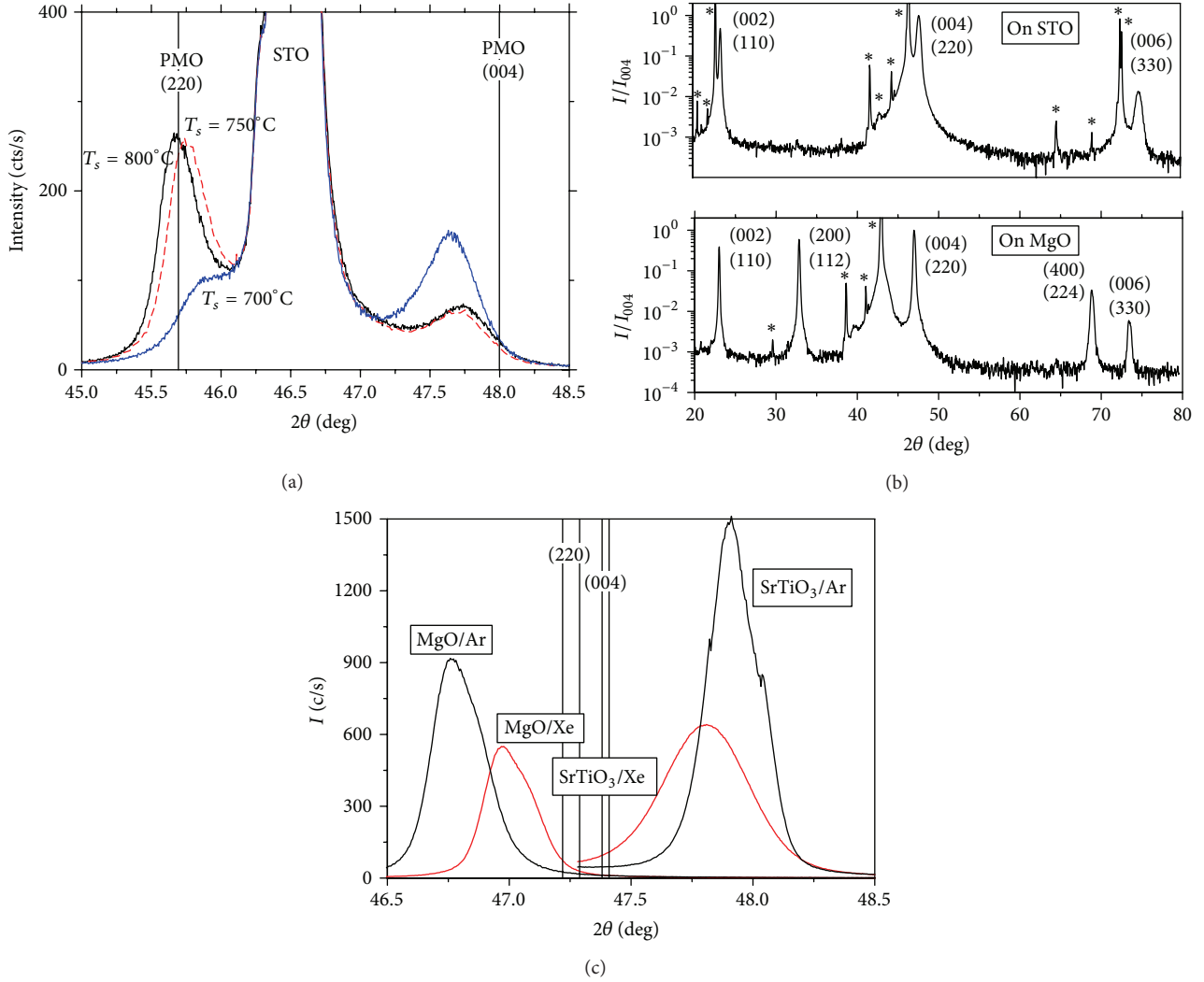
(a)

(b)

(c)

FIGURE 3: X-ray diffraction pattern of PCMO films. (a) Detailed scans in the vicinity of the (004)/(220) reflection of 400 nm thick PMO films on STO prepared by Xe sputtering at different deposition temperatures. The vertical lines have been calculated from the bulk data in Table 2. (b) Overview: PCMO ($\delta = 0$, $X = 0.36$) on SrTiO$_3$ (top) and MgO (bottom) prepared by Xe sputtering in the same run (samples F03_1a and F03_1b). The stars mark reflections which correspond to the respective substrate. This was confirmed by X-ray analysis of the noncoated substrate backsides. (c) Detailed scans in the vicinity of the (004)/(220) reflection. In addition, samples prepared by Ar sputtering ($\delta = 0$ and $X = 0.33$) are also shown (D03_1a, D03_1b): the straight lines correspond to the bulk plane spacing of d_{220} (left) and d_{004} (right) for $X = 0.33$ and 0.36. The plane spacings have been calculated from the bulk data in Table 2.

plane spacings d_{004} and d_{220} are very similar. It has been pointed out that the preferable growth direction depends on the Ca content; that is, [001] growth dominates for $X = 0.5$ and [110] growth dominates for $X = 0.3$ [16]. However, we observe by means of TEM that films with $X \approx 0.3$ reveal large volume fraction (~75%) of the [001] growth direction.

Films prepared on MgO show an additional pronounced peak in XRD which corresponds to [200] or [112] growth direction. Since the structure factors of [112]/[200] are much larger than the structure factors of [220]/[004] (see Table 2), the volume fraction of this misorientation amounts only to a few volume percent for $X \approx 0.3$. This is also observed for films on Pt/MgO. In contrast, PCMO films with $X = 0.5$ on MgO reveal large volume fraction of the [112] orientation, which has been also reported in [6].

Regardless of the details of composition and deposition, films prepared by ion-beam sputtering are highly strained and the strain depends on the substrate type and the used sputter gas. Figure 3(c) shows detailed scans in the vicinity of the [220]/[004] reflection for samples prepared on STO and MgO using Ar and Xe as sputter gases. The main observations are as follows:

(i) Deposition on STO results in a decrease of the lattice spacing perpendicular to the substrate (out-of-plane) with respect to bulk lattice spacing. This implies a tensile in-plane strain state. In contrast, deposition on MgO causes a compressive in-plane strain state.

(ii) The asymmetry of the four reflections may indicate that the [220] volume fraction is higher on MgO
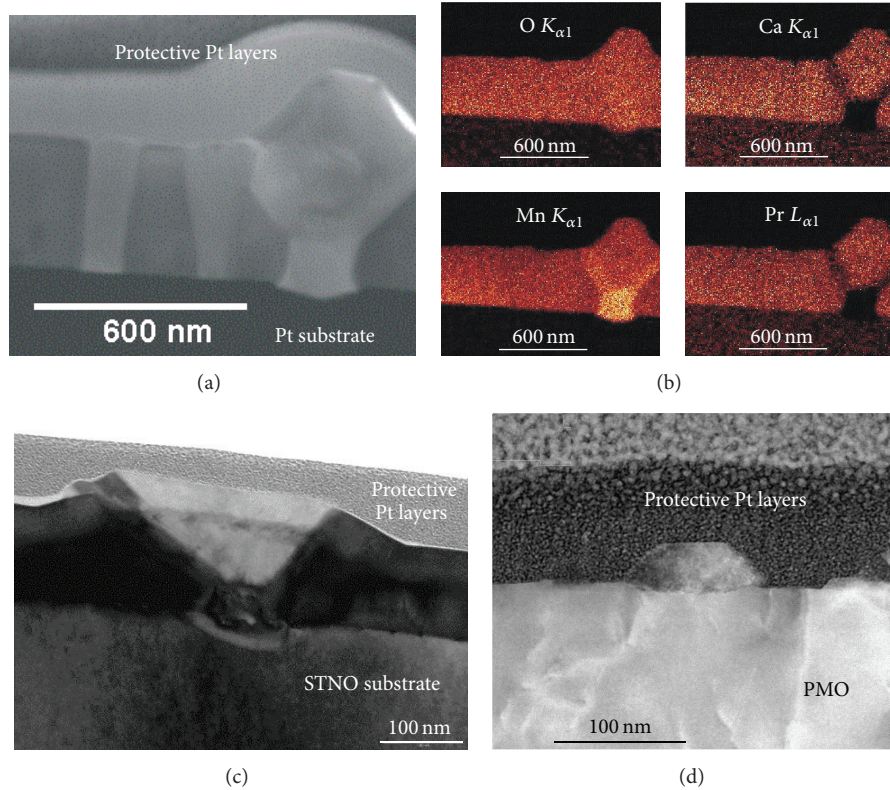
(a)

(b)

(c)

(d)

FIGURE 4: Cross-sectional TEM analysis of PCMO thin films ($\delta \approx 0$). (a) PCMO ($X = 0.5$) film on Pt-coated MgO (H05_1), bright-field image of an area with two twin domains (left) and a pronounced growth disturbance (right). (b) EDX element mapping of the same area. (c) Growth disturbance in an 110 nm thick PCMO film ($X = 0.35$) on Nb-doped (0.1 wt.%) STO substrate (C03_1). (d) Surface precipitate on top of a 410 nm thick PMO ($X = 0$) film on STO (A0_1). The sample was postannealed for 20 h at 900°C in air.

substrates but not strongly affected by the choice of the sputter gas. Large volume fractions of this orientation have been also observed for $X = 0.5$ by means of TEM.

(iii) The in-plane strain seems to be higher in case of Ar sputtering, presumably due to higher Ar incorporation. The small difference in the Ca content ($X = 0.33$ for Ar sputtering and $X = 0.36$ for Xe sputtering) cannot explain the large difference in lattice parameters.

In ion-beam sputtering, the emitted target atoms and, especially, the target-reflected noble gas atoms give rise to pronounced defect and strain generation [17]. This is partly compensated by defect annihilation due to the rather high deposition temperatures. The impact of reflected Ar atoms can be directly measured because of Ar-incorporation. Energy Dispersive X-Ray Analysis (EDX) of PCMO samples prepared by Ar as working gas reveals an Ar content of about 1 at.%. It is interesting to note that the usage of Ar instead of Xe increases the compressive strain on MgO and the tensile strain on STO. This excludes that a simple atomic volume argument related to Ar-incorporation can explain the strain state. We rather assume that point defect generation by impinging Ar atoms is additionally influencing the substrate induced strain states.

In contrast, the Xe atoms with large atomic radius are hardly implemented. Xe reflection at the target only contributes to defect formation at the surface of the growing film. The full-width-half-maximums (FWHM) of the XRD reflections are larger for films prepared by means of Xe sputtering. This points to a higher degree of lattice disorder.

Independently from the Ca content and the used substrate type, PCMO films with near-stoichiometric composition ($\delta \approx 0$) contain precipitates of a MnO_z phase which give rise to pronounced growth disturbances as shown in Figure 1. Figures 4(a) and 4(b) reveal a cross-sectional TEM bright-field image and the corresponding EDX mapping of the different elements for a PCMO film with $X = 0.5$ on Pt/MgO. A precipitate nucleated at the interface between Pt and PCMO provokes a pronounced outgrowing PCMO misorientation. Within the resolution of the EDX system only manganese and oxygen are detected in the precipitate. The low Pr and Ca signal in the grain boundary between the PCMO outgrowth and the surrounding PCMO matrix points to a pronounced grain boundary wetting with MnO_z.

Precipitation can take place at the interface to the substrate as well as in the interior (Figure 4(c)) and at the surface of PCMO (Figure 4(d)). We have no reliable statistic with respect to preferred nucleation sites, but it seems that all three nucleation types are present in PCMO films with $X = 0.3$ and 0.5. In contrast, PMO films seem to only reveal
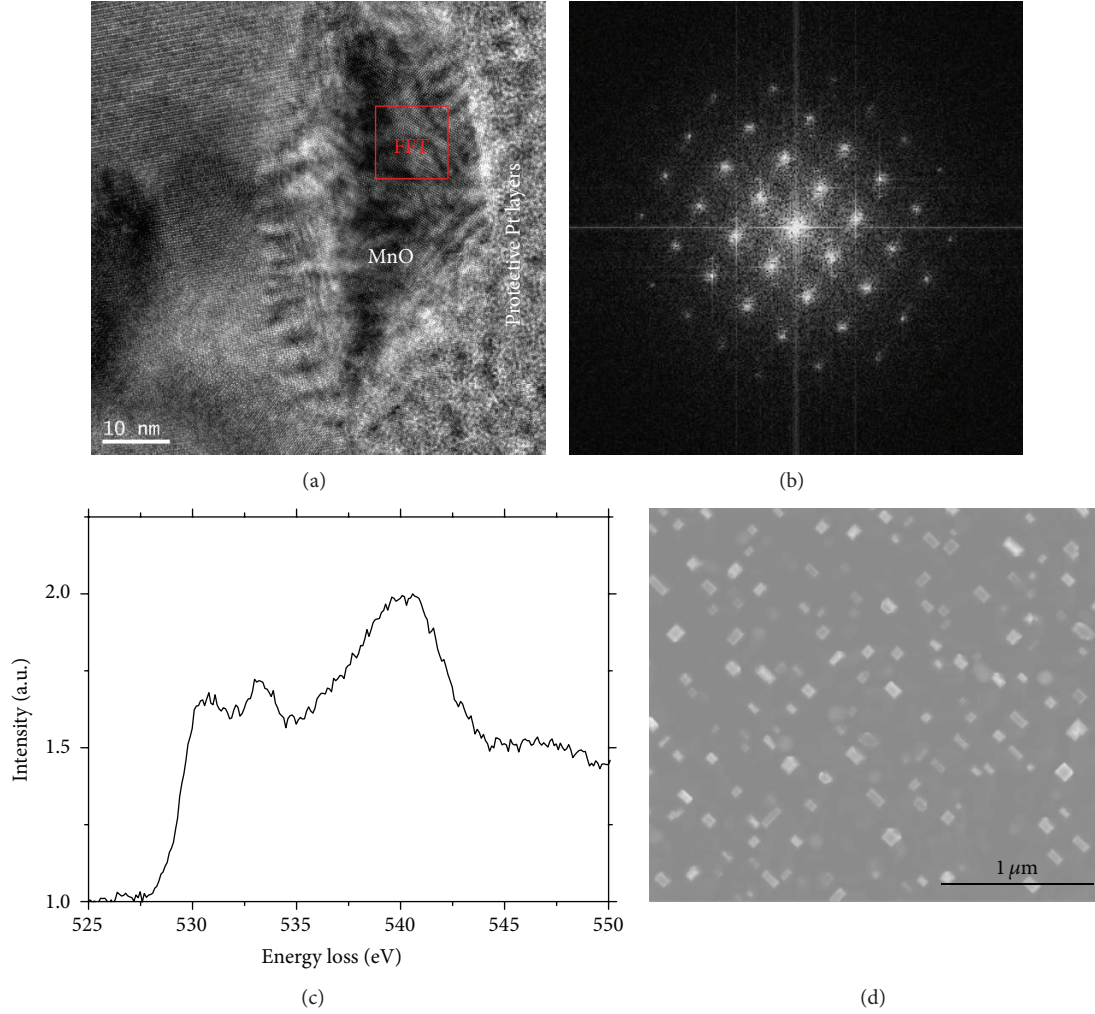
(a)

(b)

(c)

(d)

FIGURE 5: Detailed analysis of surface precipitates in PMO (sample shown in Figure 4(d)). The underlying PMO reveal two different twin domains with common [110] growth directions. (a) High-resolution image of a surface precipitates and top area of PMO. (b) FFT image of the surface precipitate. The selection for the FFT is marked in (a). (c) EELS spectrum of the oxygen K edge of a surface precipitate, which reveals the typical features of MnO [18]. (d) SEM image of the PMO surface showing very regular and well-orientated surface precipitates. The precipitate edges are parallel to the ⟨110⟩ directions of the STO substrate.

surface precipitates, even in thick films. For example, the PMO film presented in Figure 4(d) is about 400 nm thick. Therefore, precipitation can induce different microstructures, such as embedded precipitates, surface precipitates, and near substrate precipitates leading to PCMO misorientations which protrude from the film surface.

Manganese can form different oxides, for example, MnO, Mn_2O_3, Mn_3O_4, and MnO_2. In order to identify the crystal structure of the MnO_z precipitates, we have analyzed the precipitates in more detail. Figure 5 shows a high-resolution image (a) and the local Fast Fourier Transformation (FFT) image of the surface precipitate (b). By taking into account the lattice parameters (see Table 3) of the different MnO_z phases, the FFT of the surface precipitate with an in-plane lattice parameter of $a_{in} = 0.41$ nm and an out-of-plane parameter of $a_{oop} = 0.48$ nm is only compatible with a highly distorted MnO or MnO_2 phase. Mn_2O_3 and Mn_3O_4 can be excluded because the lattice parameters are too large.

TABLE 3: Space group and lattice parameters a, b, and c of the different manganese oxides.

	Space group	a [nm]	b [nm]	c [nm]	Ref.
MnO	Fm3m	0.445	0.445	0.445	[31]
MnO_2	Pbnm	0.452	0.927	0.286	[32]
Mn_2O_3	Pcab	0.941	0.942	0.940	[33]
Mn_3O_4	I41/amd	0.575	0.575	0.942	[34]

Comparing the EELS spectra at the oxygen K edge of the precipitates (Figure 5(c)) with reference data of the various manganese oxides [18] here points to the MnO phase.

The sample shown in Figure 5 was additionally postan-nealed for 20 h at 900°C. From the viewpoint of the equilib-rium phase diagram [19], a transition from the MnO phase which is only stable at low oxygen partial pressures to the Mn_2O_3 phase is expected but not observed. Consequently,
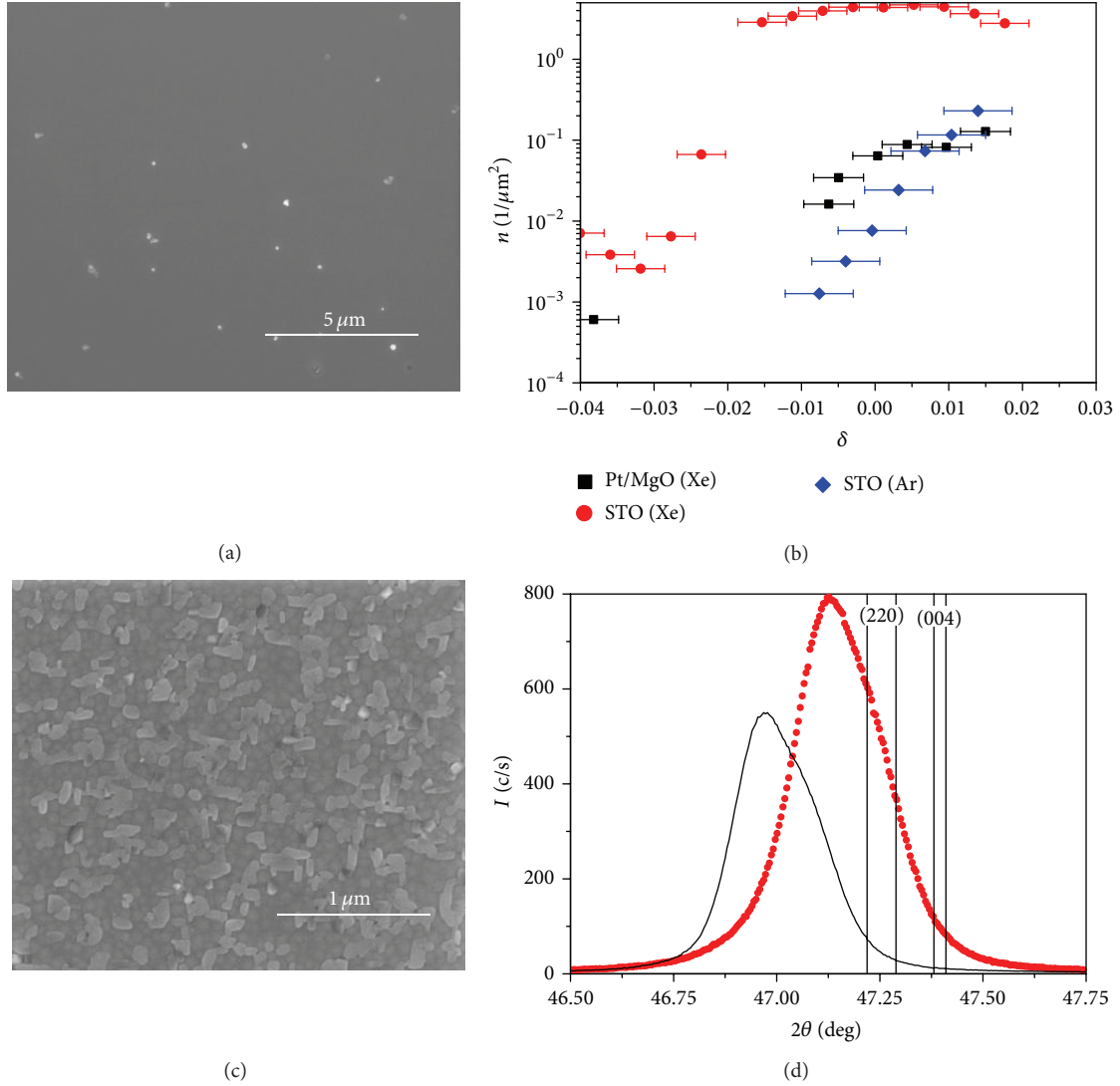
(a)

(b)

(c)

(d)

Figure 6: Outgrowth density and the influence of Mn excess for samples with $X \approx 0.3$. (a) SEM picture of a PCMO film (G03_1) with a small Mn deficit ($\delta = -0.02$) on STO. (b) Surface density of outgrowths in dependence on the Mn excess. The Mn excess δ was deduced from EDX measurements using linear fits of the concentration profile (see also Figure 2(c)). The error bar represents the uncertainness in the concentration measurement. Same symbols belong to samples prepared in the same deposition run. The respective stoichiometric samples ($\delta = 0$) are B03_1 (black squares, substrate Pt/MgO, and sputter gas Xe), F03_1a (red circles, STO, and Xe), and D03_1a (blue diamonds, STO, and Ar). (c) SEM picture of a PCMO film on MgO (F03_1b). The film has the same composition ($X = 0.36$, $\delta = 0$) and was prepared in the same run as the sample F03_1a on STO shown in Figure 1(a). (d) XRD patterns of two PCMO films ($X = 0.36$, $\delta = 0$) on MgO prepared in different runs. The sample marked by solid symbols reveals outgrowths; the second film (F03_1b, solid line) is free of outgrowths.

the MnO phase seems to be stabilized by coherent or semicoherent growth on the underlying PMO film. Since the MnO lattice constant is larger than the PMO lattice constant, such growth should give rise to compressive in-plane strain within the precipitate, that is, to the experimentally observed relation $a_{\text{in}} < a_{\text{oop}}$. The preferred orientation of the precipitate edges parallel to the [110] directions of STO also points to an epitaxial relation between MnO and PMO (Figure 5(d)). However, since quantitative EDX investigations on precipitates in different samples point to MnO_2 and precipitation might be different in PMO and PCMO because

of different misfits, we currently only would like to conclude the formation of MnO_z phases.

The TEM results imply a correlation between growth disturbances visible at the PCMO surface (Figure 1) and the presence of MnO_z precipitates. The link becomes also apparent by comparing samples prepared with different Mn contents. Figure 1(a) ($\delta = 0$) and Figure 6(a) ($\delta = -0.02$) show that the surface number density of outgrowths n decreases by orders of magnitude in Mn-deficit films. Plotting n versus the Mn excess δ (Figure 6(b)) reveals the same trend for samples on STO and Pt-coated MgO substrates

and for different sputter gases: the outgrowths vanish if the films become Mn deficient. Since δ was deduced from EDX measurements, we may slightly underestimate the Mn content by about 2%. Therefore, we only state that the outgrowth vanishes close to the stoichiometric composition $\delta \approx 0$.

Depending on small change in the detailed deposition conditions, films prepared on MgO can reveal no MnO_z precipitates for near-stoichiometric compositions $\delta \pm 0.02$. The sample on MgO shown in Figure 6(c) is outgrowth-free and also cross section TEM analysis shows no MnO_z precipitates in the volume of the thin films. In contrast, the film on STO (Figure 1(a)) prepared in the same run and with the same composition (at the same position x_s but at different positions y_s) reveals a high density of growth disturbances. However, the precipitation is not only controlled by the substrate choice, for example, by interfacial energies or lattice mismatch. Sometimes, PCMO films on MgO substrates grown under the same deposition conditions show the formation of precipitates (cf., e.g., Figures 6(c) and 1(b)). It is interesting to compare samples with and without precipitates with respect to their strain state. The X-ray diffraction pattern in Figure 6(d) shows that the out-of-plane strain in precipitate-free samples is significantly higher. Therefore, the precipitation is related to both the Mn content and the strain.

4. Discussion

As far as we know, no phase diagram of Ca-doped PMO has been published which takes Mn excess into account. The Mn solubility in the Perovskite phases of $LaMnO_3$ and $PrMnO_3$ corresponds to $\delta \approx 0.1$. Ca-doping of $LaMnO_3$ seems to increase the solubility [20–22]. Such large solubilities are not observed in our PCMO thin film samples (Figure 6(b)). By taking into account the uncertainness in concentration measurement, the maximum solubility seems to be smaller than $\delta \approx 0.02$. Low deposition temperatures T_s prohibit the formation of outgrowths. However, such films commonly reveal no CMR [23] and are of minor interest. Because of the limited statistic of TEM investigations and the uncertainness in concentration determination, we cannot quantitatively relate Mn excess, outgrowth density, and typical size of precipitates. However, assuming that precipitation takes place if $\delta > 0$, one may write (A represents A-site cations Pr and Ca)

$$A + (1 + \delta)\, Mn + \frac{3 + 2\delta}{2} O_2 \longrightarrow AMnO_3 + \delta MnO_2 \quad (1)$$
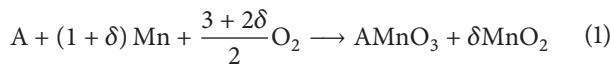
Since there is a clear correlation between MnO_z formation and outgrowth density n, we assume that each precipitate gives rise to a visible growth disturbance. Consequently, the volume fraction of precipitates for a small excess δ is expressed as

$$\frac{V_{MnO_2}}{V_{MnO_2} + V_{PCMO}} \approx \delta \cdot \frac{V^m_{MnO_2}}{V^m_{PCMO}} \approx \frac{n \cdot v_{MnO_2}}{d_f}, \quad (2)$$

where V^m are the mole volumes, v_{MnO_2} is the mean volume of the precipitates, and d_f is the film thickness. Using the ratio

of mole volumes of about 0.46, Mn excess of 2%, and small (large) precipitates with a volume $v_P \approx 2.4 \times 10^5$ nm^3 (2.0×10^7 nm^3) should result in a surface density of outgrowths of $n \approx 4.2/\mu m^2$ ($0.14/\mu m^2$). This coarse estimations support the main trends shown in Figure 6(b): the formation of a high density of small precipitates on STO and a lower density of large precipitates with pronounced grain boundary wetting on Pt-coated MgO (see also Figure 4(b)).

The most probable origin of the limited solubility is the strain accompanying heteroepitaxial growth. Incorporation of Mn excess in the Perovskite phase is compensated by the formation of A-site vacancies which gives rise to a reduced unit cell volume (e.g., for $LaMnO_3$ [20] and for $PrMnO_3$ [24]). It has been shown by means of DFT calculations that compressive in-plane strain favors the formation of cation vacancies [25]. Although the change of the lattice constants is rather small (of the order of -0.06% for $PrMnO_3$ with $\delta = 0.01$ [24]), a tensile lattice mismatch to the substrate may favor the formation of the stoichiometric Perovskite phase with its larger unit cell and therefore drive the precipitation of MnO_z.

However, the different strain states on different substrates at room temperature cannot be directly compared without taking into account the pronounced influence of phase formation which depends on the deposition parameters. PCMO undergoes a phase transition from cubic to orthorhombic in a temperature range of 1100–1200 K [26] which is very close to the typical deposition temperature of about 1073 K. The strain generated by this transition relaxes partly by twinning.

In addition to the twinning induced strain relaxation during film growth, the precipitation of MnO_z is affected by the mobility of cations. MnO_z formation requires a sufficiently high surface mobility of adatoms. Because of the pronounced wetting (Figure 4(b)), grain boundary diffusion also seems to play a significant role. It is therefore important to determine the strain evolution during deposition and cooling down to room temperature.

In order to determine the stress state during film deposition and cooling, we have performed in situ stress measurements with the hot stage. The thickness dependent stress for deposition on STO (at $T_s = 800°C$) and Pt-coated MgO (at $T_s = 700°C$) is shown in Figure 7. It is out of the frame of this contribution to discuss all details of these measurements, we will therefore mainly focus on the main observations:

(i) The stress in the early growth state of PCMO on STO is tensile and rather large (up to 4 GPa). Due to the large lattice mismatch $\Delta_s = (\langle a_{pc} \rangle - a_s)/a_s$ between PCMO and STO of $\Delta_{STO} = -1.6\%$ (see Table 1), the growth mode is most probably 3D growth and the island coalescence may give rise to the pronounced stress maximum at a film thickness of about 10 nm [27]. Although the misfit to Pt ($\Delta_{Pt} = -2.0\%$) is larger, the tensile stress is lower on Pt-coated MgO substrates because the elastically softer Pt film partly accommodates the misfit. Nevertheless, the stress in the early growth state is also of the order of GPa.

(ii) After the early growth stage, the stress decreases with increasing thickness but still stress remains high. The
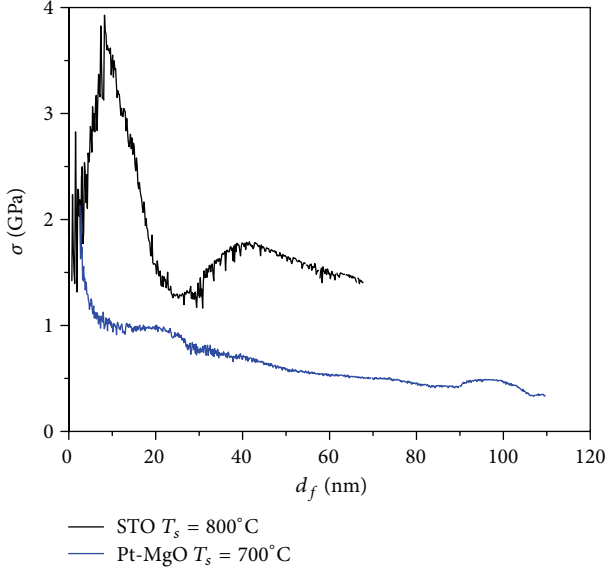
FIGURE 7: In situ determination of the thickness dependent stress during deposition of PCMO ($X = 0.33$, $\delta = 0$) on STO and Pt-coated MgO substrates. The actual film thicknesses were calculated from deposition rate times time and the final thickness amounts to about 100 nm for both samples. In the case of the deposition on STO, the reflected laser beams moved out of the detection window above $d_f \approx 65$ nm. Using the linear part of the plot, we estimate the stress at 100 nm to be about 1 GPa. During cooling, the reflected beams moved back and the stress evolution could be measured.

almost linear decrease is not very different for samples on STO and Pt-coated MgO.

(iii) Cooling down the samples from deposition temperature to room temperature strongly modifies the stress. For the 100 nm thick films, the stress decreases from about 1 GPa to 490 MPa on STO and from 250 MPa to −260 MPa in the case of Pt-coated MgO. Postmeasurement values in XRD at room temperature show that the PCMO film on STO (Pt-coated MgO) reveals an out-of-plane strain of $\varepsilon_{oop} = -0.5\%$ (+0.4%) which implies a tensile (compressive) in-plane strain.

It is worthwhile to note that this strong change of the stress during cooling cannot be attributed to the thermal strain induced due the difference in thermal expansion coefficient between film and substrate. Assuming for simplicity an isotropic biaxial strain state with a reasonable Poisson ratio for PCMO of $\nu \approx 0.35$, the stress change due to cooling from T_s down to room temperature T_0 is given by

$$
\begin{aligned}
\frac{\Delta\sigma}{\sigma(T_0)} &= \frac{\sigma(T_s) - \sigma(T_0)}{\sigma(T_0)} = \frac{\Delta\varepsilon}{\varepsilon_{ip}(T_0)} \\
&= -\frac{2 \cdot \nu}{1 - \nu} \cdot (\alpha_S - \alpha_{ip}) \cdot \frac{(T_0 - T_s)}{\varepsilon_{oop}(T_0)} \\
&\cong -(\alpha_S - \alpha_{ip}) \cdot \frac{(T_0 - T_s)}{\varepsilon_{oop}(T_0)},
\end{aligned}
\tag{3}
$$

TABLE 4: Linear thermal expansion coefficient of PCMO and substrate materials. The thermal strain $\Delta\varepsilon$ generated in PCMO films on the different substrates during cooling von 800°C down to room temperature is also mentioned.

	α [10^{-6}/K]	$\Delta\varepsilon$ [%]
$Pr_{0.7}Ca_{0.3}MnO_3$	11.9 [35]	
$SrTiO_3$	9	0.23
Pt	8.8	0.24
MgO	8	0.3

where α_S and α_{ip} are the almost constant linear thermal expansion coefficients of the substrate and the PCMO film in the high-temperature range, respectively. Since α_{ip} is larger than α_S, only small additional tensile strain contributions are expected (see Table 4) in contrast to the experimental findings. For PCMO on STO, for example, the observed stress change $\Delta\sigma/\sigma \approx 1$ corresponds to the generation of an additional compressive in-plane strain which is of the order of the room temperature out-of-plane strain $\Delta\varepsilon \approx -\varepsilon_{oop} = 0.5\%$.

The defect structure of the PCMO thin films strongly affects the correlation physics of the PCMO thin films. Hoffmann et al. [23] show a systematic study of the influence of preparation induced octahedral disorder on the CMR in thin film PCMO samples with $X = 0.32$–0.34 prepared by means of PLD and IBS deposition on STO and MgO. Independent of the deposition method, the CMR only can be observed if the deposition temperature is high enough (about 750°C). Postannealing at temperatures above the deposition temperature increases the CMR transition temperature due to defect annihilation.

In addition to octahedral disorder, point like defects have a strong effect on the correlated electron properties. Oxygen vacancies which are formed by resistive switching can suppress the CMR effect in Pt-PCMO-Pt sandwich structures [28] and can even give rise to vacancy induced metal-insulator transitions [29]. However, the influence of point defects on the correlation properties is rather complex due to specific features of defect chemistry in manganites. For example, oxygen vacancy formation can significantly affect the A/B cation site ratio [30] with drastic effects on the ferromagnetic properties.

In the IBS PCMO films presented in this paper, Mn excess has only a minor influence, because the high stress state results in MnO_z precipitation and therefore drives the formation of a near-stoichiometric PCMO phase. Our results show that the evolving strain state and its influence on the correlation effect, for example, the CMR, are rather complex. Beside the lattice mismatch, the generation of most likely point-like defects due to the high-energy impact and the annihilation due to the high deposition temperatures has to be taken into account. In general, the flexibility of the octahedral tilt system allows for accommodation of the misfit in very thin films, which has been indeed observed for PLD films [4]. For IBS films, we observe only a moderate decrease of stress with increasing film thickness. This implies that the net defect generation rate during deposition significantly

contributes to the stress state. This contribution does not strongly depend on the substrate choice. Defect annihilation might be the origin of the pronounced compressive stress contribution, which appears during the slow cooling down to room temperature after the deposition.

The formation of MnO_z precipitates also seems to be an important pathway of stress relaxation, because the room temperature strain of precipitate-free samples is significantly higher. Large tensile stress during deposition seems to favor the precipitation. We have not measured the stress during deposition for MgO substrates. Although the nominal lattice mismatch between PCMO and MgO is highly tensile, the room temperature strain state is compressive. We therefore expect that the misfit stress contribution to the stress-strain state of PCMO on MgO during deposition is not so high due to the presence of a coincidence lattice. Conclusively, the observed compressive stress must evolve because of the defect relaxation processes including twins and point defects, which are not strongly affected by the substrate choice.

Deposition at temperatures close to the cubic-orthorhombic phase transition and pronounced stress relaxation during deposition and cooling seems to be the reason for the rather broad ranges of possible strain states at room temperature on the same type of substrate. However, the appearance of precipitation is not only controlled by the lattice mismatch. Using Ar instead of Xe changes the number density of precipitates at the same Mn excess (Figure 6(b)). We suggest that the precipitation as stress relaxation takes place if the stress during deposition exceeds a critical threshold. This might explain why deposition with Xe with its high defect generation rate can result in a room temperature state with a low strain (Figure 3(b)).

5. Conclusions

The deposition of $Pr_{1-X}Ca_XMnO_3$ with X ranging from 0 to 0.5 by means of ion-beam sputtering is accompanied by high density of point defects which is determined by the balance of generation and annihilation rates. After termination of the film deposition, defect generation is stopped and some of the strain may be relaxed via point defect relaxation channels. However, we conclude that the formation of MnO_z precipitates represents another important relaxation path if a stress threshold is overcome. The high tensile strain during the early growth stage on STO seems to favor the formation of a high density of precipitates due to the reduction of misfit. Even if the stress is lower for the Pt-coated MgO, the remaining stress is in the order of GPa and seems to be high enough to result in the formation of precipitates. We do not expect large tensile strain on MgO. Therefore, precipitation only takes place if the stress caused by defect formation exceeds the critical stress.

Conflict of Interests

The authors declare that there is no conflict of interests regarding the publication of this paper.

References

[1] E. Dagotto, *Nanoscale Phase Separation and Colossal Magnetoresistance*, Springer Series in Solid-State Sciences, Springer, Berlin, Germany, 2003.

[2] J. L. García-Muñoz, J. Fontcuberta, M. Suaaidi, and X. Obradors, "Bandwidth narrowing in bulk $L_{2/3}A_{1/3}MnO_3$ magnetoresistive oxides," *Journal of Physics Condensed Matter*, vol. 8, no. 50, pp. L787–L793, 1996.

[3] A. J. Millis, P. B. Littlewood, and B. I. Shraiman, "Double exchange alone does not explain the resistivity of $La_{1-x}Sr_xMnO_3$," *Physical Review Letters*, vol. 74, no. 25, pp. 5144–5147, 1995.

[4] W. Prellier, C. Simon, A. M. Haghiri-Gosnet, B. Mercey, and B. Raveau, "Thickness dependence of the stability of the charge-ordered state in $Pr_{0.5}Ca_{0.5}MnO_3$ thin films," *Physical Review B*, vol. 62, no. 24, Article ID R16337, 2000.

[5] Z. Q. Yang, Y. Q. Zhang, J. Aarts, M.-Y. Wu, and H. W. Zandbergen, "Enhancing the charge ordering temperature in thin films of $Pr_{0.5}Ca_{0.5}MnO_3$ by strain," *Applied Physics Letters*, vol. 88, no. 7, Article ID 072507, 2006.

[6] D. K. Baisnab, T. Geetha Kumary, A. T. Satya et al., "Intricacies of strain and magnetic field induced charge order melting in $Pr_{0.5}Ca_{0.5}MnO_3$ thin films," *Journal of Magnetism and Magnetic Materials*, vol. 323, no. 22, pp. 2823–2827, 2011.

[7] T. L. Aselage, D. Emin, S. S. McCready et al., "Metal-semiconductor and magnetic transitions in compensated polycrystalline $La_{1-x}Ca_xMnO_{3-\delta}(x = 0.20, 0.25)$," *Physical Review B*, vol. 68, Article ID 134448, 2003.

[8] A. Arulraj, R. Mahesh, G. N. Subbanna, R. Mahendiran, A. K. Raychadhuri, and C. N. R. Rao, "Insulator-metal transitions, giant magnetoresistance, and related aspects of the cation-deficient LaMnO_3 compositions $La_{1-\delta}MnO_3$ and $LaMn_{1-\delta'}O_3$," *Journal of Solid State Chemistry*, vol. 127, no. 1, pp. 87–91, 1996.

[9] A. R. Kaul, O. Y. Gorbenko, and A. A. Kamenev, "The role of heteroepitaxy in the development of new thin-film oxide-based functional materials," *Russian Chemical Reviews*, vol. 73, no. 9, pp. 861–880, 2004.

[10] A. Pundt and R. Kirchheim, "Hydrogen in metals: microstructural aspects," *Annual Review of Materials Research*, vol. 36, pp. 555–608, 2006.

[11] F. La Via, V. Privitera, C. Spinella, and E. Rimini, "Stress-induced precipitation of dopants diffused into Si from $TiSi_2$ and $CoSi_2$ implanted layers," *Semiconductor Science and Technology*, vol. 8, no. 7, pp. 1196–1203, 1993.

[12] S. Tian, J. Zhang, Y. Xu, Z. Hu, and H. Yang, "Stress-induced precipitation of fine gamma′-phase and thermodynamics analysis," *Journal of Materials Science & Technology*, vol. 17, no. 2, pp. 257–259, 2001.

[13] G. G. Stoney, "The tension of metallic films deposited by electrolysis," *Proceedings of the Royal Society of London Series A*, vol. 82, no. 553, pp. 172–175, 1909.

[14] S. D. Ekpe, L. W. Bezuidenhout, and S. K. Dew, "Deposition rate model of magnetron sputtered particles," *Thin Solid Films*, vol. 474, no. 1-2, pp. 330–336, 2005.

[15] Z. Jirak, S. Krupicka, Z. Simsa, M. Dlouha, and S. Vratislav, "Neutron diffraction study of $P_{1-x}Ca_xMnO_3$ perovskites," *Journal of Magnetism and Magnetic Materials*, vol. 53, p. 153, 1985.

[16] M. Fujimoto, H. Koyama, Y. Nishi et al., "Crystallographic domain structure of an epitaxial $(Pr_{0.7}Ca_{0.3})MnO_3$ thin film grown on a $SrTiO_3$ single crystal substrate," *Journal of the American Ceramic Society*, vol. 90, no. 7, pp. 2205–2209, 2007.

[17] H. Windischmann, "Intrinsic stress in sputter-deposited thin films," *Critical Reviews in Solid State and Materials Sciences*, vol. 17, no. 6, pp. 547–596, 1992.

[18] H. Paterson, "ELNES of 3d transition-metal oxides," *Ultramicroscopy*, vol. 32, p. 319, 1990.

[19] R. Metselaar, R. E. J. Van Tol, and P. Piercy, "The electrical conductivity and thermoelectric power of Mn_3O_4 at high temperatures," *Journal of Solid State Chemistry*, vol. 38, no. 3, pp. 335–341, 1981.

[20] J. A. M. van Roosmalen, P. van Vlaanderen, E. H. P. Cordfunke, W. L. Ijdo, and D. J. W. Ijdo, "Phases in the Perovskite-type $LaMnO_{3+\delta}$ solid solution and the La_2O_3-Mn_2O_3 phase diagram," *Journal of Solid State Chemistry*, vol. 114, no. 2, pp. 516–523, 1995.

[21] V. F. Balakirev, O. M. Fedorova, S. K. Estemirova, and Y. V. Golikov, "The homogeneity range of praseodymium manganite $Pr_{2-x}Mn_xO_{3\pm\delta}$ in air," *Doklady Physical Chemistry*, vol. 414, no. 1, pp. 110–111, 2007.

[22] F. Figueiras, J. M. Vieira, M. E. Guzik, J. Legendziewicz, P. B. Tavares, and V. S. Amaral, "The effects of Ca and Mn excess co-doping in CMR manganites solid solution structures," *Materials Science Forum*, vol. 514–516, no. 1, pp. 294–298, 2006.

[23] J. Hoffmann, P. Moschkau, S. Mildner et al., "Effects of interaction and disorder on polarons in colossal resistance manganite $Pr_{0.68}Ca_{0.32}MnO_3$ thin films," *Materials Research Express*, vol. 1, no. 4, Article ID 046403, 2014.

[24] W. Boujelben, A. Cheikh-Rouhou, J. C. Joubert, and J. Pierre, "Stuctural and magnetic study of Perovskite manganites oxides $Pr_{0.5}Sr_{0.5-x}\square_xMnO_3$," *Physical and Chemical News*, vol. 2, pp. 1–3, 2001.

[25] U. Aschauer, N. Vonrüti, and N. A. Spaldin, "Effect of epitaxial strain on cation and anion vacancy formation in MnO," http://arxiv.org/abs/1506.00995v1.

[26] M. A. Carpenter, R. E. A. McKnight, C. J. Howard, and K. S. Knight, "Symmetry and strain analysis of structural phase transitions in $Pr_{0.48}Ca_{0.52}MnO_3$," *Physical Review B*, vol. 82, no. 9, Article ID 094101, 2010.

[27] M. F. Doerner and W. D. Nix, "Stresses and deformation processes in thin films on substrates," *Critical Reviews in Solid State and Materials Sciences*, vol. 14, no. 3, pp. 225–268, 1988.

[28] M. Scherff, J. Hoffmann, B. Meyer, T. Danz, and C. Jooss, "Interplay of cross-plane polaronic transport and resistive switching in Pt-$Pr_{0.67}Ca_{0.33}MnO_3$–Pt heterostructures," *New Journal of Physics*, vol. 15, Article ID 103008, 2013.

[29] H. S. Lee, S. G. Choi, H.-H. Park, and M. J. Rozenberg, "A new route to the Mott-Hubbard metal-insulator transition: strong correlations effects in $Pr_{0.7}Ca_{0.3}MnO_3$," *Scientific Reports*, vol. 3, article 1704, 2013.

[30] I. Marozau, P. T. Das, M. Döbeli et al., "Influence of la and Mn vacancies on the electronic and magnetic properties of $LaMnO_3$ thin films grown by pulsed laser deposition," *Physical Review B*, vol. 89, no. 17, Article ID 174422, 2014.

[31] B. Morosin, "Exchange striction effects in MnO and MnS," *Physical Review B*, vol. 1, no. 1, pp. 236–243, 1970.

[32] J. E. Post and P. J. Heaney, "Neutron and synchrotron X-ray diffraction study of the structures and dehydration behaviors of ramsdellite and 'groutellite'," *American Mineralogist*, vol. 89, no. 7, pp. 969–975, 2004.

[33] S. Geller, "Structures of α-Mn_2O_3, $(Mn_{0.983}Fe_{0.017})_2O_3$ and $(Mn_{0.37}Fe_{0.63})_2O_3$ and relation to magnetic ordering," *Acta Crystallographica B*, vol. 27, pp. 821–828, 1971.

[34] V. Baron, J. Gutzmer, H. Rundlo, and R. Tellgren, "The influence of iron substitution on the magnetic properties of hausmannite, $Mn^{2+}(Fe,Mn)_2^{3+}0_4$," *American Mineralogist*, vol. 83, no. 7-8, pp. 786–793, 1998.

[35] H. Rim, S. Jeung, E. Jung, and J. Lee, "Characteristics of $Pr_{1-x}M_xMnO_3$ (M = Ca, Sr) as cathode material in solid oxide fuel cells," *Materials Chemistry and Physics*, vol. 52, no. 1, pp. 54–59, 1998.

Research Article

Facile Synthesis of Rambutan-Like ZnO Hierarchical Hollow Microspheres with Highly Photocatalytic Activity

Ke-Jian Ju,[1] Ming Zhang,[2] Qian-Li Zhang,[1] Jie Wei,[1] and Ai-Jun Wang[2,3]

[1]*School of Chemistry and Biological Engineering, Suzhou University of Science and Technology, Suzhou 215009, China*
[2]*School of Chemistry and Chemical Engineering, Henan Normal University, Xinxiang 453007, China*
[3]*College of Geography and Environmental Science, Zhejiang Normal University, Jinhua 321004, China*

Correspondence should be addressed to Qian-Li Zhang; zqlmhb@163.com and Ai-Jun Wang; ajwang@zjnu.cn

Rambutan-like ZnO hierarchical hollow microspheres (ZnO HHMs) were constructed under hydrothermal conditions, using carboxyl methyl starch (CMS) as a soft template. The resulting products were characterized by using X-ray diffraction (XRD), scanning electron microscopy (SEM), and transmission electron microscopy (TEM). The experimental parameters and growth mechanism of rambutan-like ZnO HHMs were discussed in some detail. The as-prepared samples displayed improved photocatalytic activity for the degradation of rhodamine B under ultraviolet (UV) irradiation.

1. Introduction

ZnO has attracted global interest as a promising alternative semiconductor to TiO_2 in dye-sensitized solar cells, owing to its direct wide band gap (3.37 eV) and high electron mobility ($17\,cm^2 \cdot V^{-1} \cdot s^{-1}$) for single-crystal ZnO nanostructures [1, 2]. Furthermore, single-crystalline ZnO displays efficient electron transport collection and a faster charge transfer for its 2/3-fold electron mobility than TiO_2. As a result, single-crystalline ZnO with a variety of sizes and shapes have been prepared, including nanowires [3, 4], nanofiber [5], nanodiscs [6], nanorods [7, 8], nanotubes [9, 10], nanonails [11], core-shell [12], and hierarchical structures [13, 14].

Now, one-dimensional (1D) ZnO nanostructures such as nanowires and nanotubes have been prepared to reduce recombination phenomena upon the electron transport process and improve the electron collection efficiency [15]. However, these 1D structures suffer from a rather low specific surface area. To solve this issue, ZnO hollow structures have attracted great attention because of their huge active surface area, stability, high porosity, and permeability (mesoporous nature) [16, 17].

To date, hollow ZnO spheres have mainly been synthesized by hard template [18]. For instance, ZnO hollow spheres have been prepared using spherobacterium *Streptococcus thermophilus* as a biotemplate [19]. However, the incubation of bacteria is time-consuming and complicated and requires special agents. Furthermore, expensive raw materials, complex process control, and sophisticated equipment are often needed, which is unfavorable for potential large-scale synthesis of single-crystal ZnO structures.

Alternatively, soft templates are expected to be more flexible in preparing ZnO hollow structures. For example, hierarchically nanoporous ZnO hollow spheres were facilely obtained using glucose as a template [20], where calcining the products is essential. Lately, flower-like and double-caged peanut-like ZnO hollow structures were prepared in our group [21, 22], which showed enhanced surface area and improved catalytic activity. Moreover, hollow microsphere assembled by the units (e.g., nanoparticles and nanorods) have some additional advantages such as enlarged surface area, easy separation, rich interface, and good stability [20–22].

Hydrothermal method is usually used for the synthesis of high-crystallized powders, owing to its simplicity, facility, low cost, and scalability [23, 24]. Besides, the products will own high purity and narrow particle size distribution. Herein, a simple hydrothermal method was developed for large-scale

synthesis of rambutan-like ZnO hierarchical hollow microspheres (HHMs) under low temperature (120°C) without the calcination procedure, using carboxyl methyl starch (CMS) as a soft template. The catalytic activity of the resulting product was examined by the photodegradation of rhodamine B as a model system.

2. Experimental Section

2.1. Chemical and Reagents. All the reagents were of analytical grade and were purchased from Aladdin Industrial Corporation and used without further purification. All aqueous solutions were prepared with twice-distilled water.

2.2. Preparation of Rambutan-Like ZnO HHMs. The rambutan-like ZnO HHMs were prepared with the assistance of CMS under hydrothermal conditions. In a typical procedure, 0.65 g of CMS was dissolved in 25 mL of water under stirring, followed by the addition of 6.25 mL of zinc nitrate solution (50 mM) into the above solution under stirring. Next, 0.625 mL of ammonia solution (25%, *w/V*) was dropwise put into the mixed solution. After stirring for 15 min, the mixture was transferred to a 50 mL Teflon-lined autoclave, sealed, and kept at 120°C for 12 h and finally cooled to room temperature naturally. The final white precipitate was collected by centrifugation, thoroughly washed with water and ethanol, and dried at 60°C in vacuum.

Control experiments with different amounts of ammonia and CMS and different temperature were performed, respectively. And the time-dependent experiments were conducted to investigate the formation mechanism of rambutan-like ZnO HHMs.

2.3. Characterization. Field emission scanning electron microscopy (FESEM) was performed with a JSM-6390LV microscope. Transmission electron microscope (TEM) and high-resolution TEM (HRTEM) images were recorded on a JEOL JEM-2100F using an accelerating voltage of 200 kV. X-ray diffraction (XRD) analysis was carried out on a Rigaku Dmax-2000 diffractometer with Cu Kα radiation. The surface areas were calculated by the Brunauer-Emmett-Teller (BET) method, and the pore size distribution was calculated from the adsorption branch using the Barett-Joyner-Halenda (BJH) theory. The UV-vis spectra were recorded on a Lambda 950 UV/vis spectrometer (PerkinElmer, USA).

2.4. Photocatalytic Experiments. The photocatalytic activity of the samples was evaluated by the photocatalytic decolorization of rhodamine B (RhB, Amresco Inc.) in aqueous solution at ambient temperature. To improve the degree of crystallinity, the product was calcined at 400°C for 2 h. Photocatalytic experiments were performed as follows: the reaction system containing 50 mL of RhB with an initial concentration of 2.5×10^{-5} M and 15 mg of the ZnO samples was stirred in the dark for 1 h to reach adsorption-desorption equilibrium before ultraviolet (UV) light irradiation. A 300 W high-pressure Hg lamp (Yaming Company, Shanghai, 8 cm away from the suspension) was used as a light source to trigger the photocatalytic reaction. The solutions were collected and centrifuged every 10 min to measure the degradation of RhB in solution by UV-vis spectroscopy.

3. Results and Discussion

3.1. Characterization of Rambutan-Like ZnO HHMs. Figure 1(a) shows the typical SEM image of rambutan-like ZnO HHMs with the average diameter of ~1 μm, where ZnO nanorods perpendicularly grow outwards on the surface of the shell, regardless of the curvature of ZnO microspheres (Figures 1(a)–1(c)). This observation is different from that of commercial ZnO samples with irregular nanoparticles (Figures S1 and S2A in Supplementary Material available online at http://dx.doi.org/10.1155/2015/242798, supporting information). Higher magnification SEM image of the cracked one demonstrates their hollow spheres again (Figure 1(c)).

As illustrated by the XRD pattern of typical ZnO HHMs (Figure 1(d)), all the diffraction peaks are well indexed to the wurtzite hexagonal ZnO with lattice constants $a = 3.249$ Å and $c = 5.207$ Å (JCPDS card 36-1451) [25, 26], respectively. No any other peaks from impurity are observed, revealing complete removal of the soft template in our system, as further proved by FTIR analysis (Figure S3, supporting information) in which all the characteristic peaks match well with pure ZnO nanoparticles [27].

TEM measurements were conducted to provide more detailed information about ZnO HHMs (Figure 2). Notably, the slight pale center together with the deep dark edge outside evidences the sphere with a large void space inside (Figure 2(a)). Similar spheres were observed using polystyrene microspheres as a hard template [28], while solid spheres were obtained with larger sizes (5 μm) in their system. The selected area electron diffraction (SAED) patterns taken from the selected area of the TEM image (Figure 2(b)) show their single-crystalline nature. Additionally, Figures 2(c)-2(d) show that all parts of the nanorods on the ZnO spheres surface only have the fringes of planes with d value of 0.25 nm [29], suggesting that the nanorods exhibit the $\{10\bar{1}1\}$ orientation. The commercial ZnO samples are also highly crystalline with a plane spacing of 0.26 nm, corresponding to the distance between two (0002) crystal planes, which indicates that they preferentially grow along the [0001] directions [29] (Figure S2B, supporting information).

Figure 3 provides the nitrogen adsorption-desorption isotherm of the typical sample calcined at 300°C. The isotherm displays a typical IV curve, while the hysteresis loop is associated with narrow slit-like pores in the sample, as confirmed by the pore size distribution curve (Inset in Figure 3). The BET specific surface area of the product is about 41.5 m$^2 \cdot$ g^{-1}, which is much larger than that of commercial ZnO powders with a value of 3.64 m$^2 \cdot$ g^{-1} [30]. This value is also higher than those of ZnO hollow spheres with the value of 9.77 m$^2 \cdot$ g^{-1} [30] and ZnO flowers with the value of 25.16 m$^2 \cdot$ g^{-1} [31]. The corresponding pore size distribution curve exhibits that most of the pores have the size of *ca.* 20 nm. The enlarged surface area of ZnO HHMs is expected to have excellent photocatalytic performance.
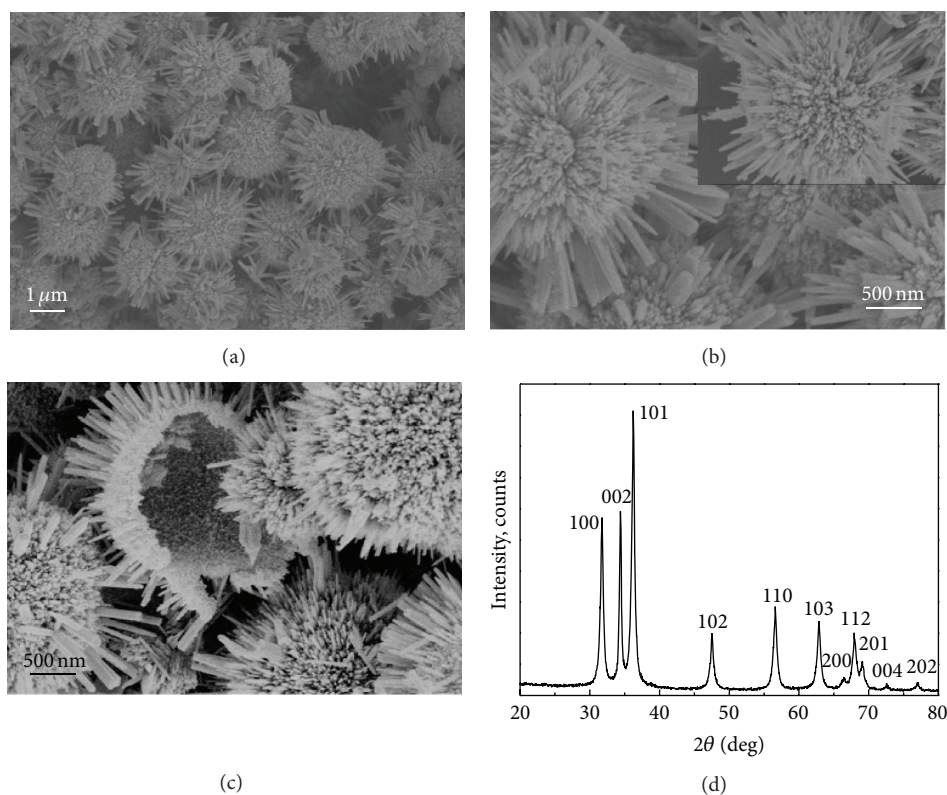
(a)

(b)

(c)

(d)

FIGURE 1: Morphological and structural characterizations of rambutan-like ZnO HHMs: the corresponding low (a) and high ((b)-(c)) magnification of the SEM images and the XRD patterns (d). The inset shows the high magnification of the SEM images of (b).
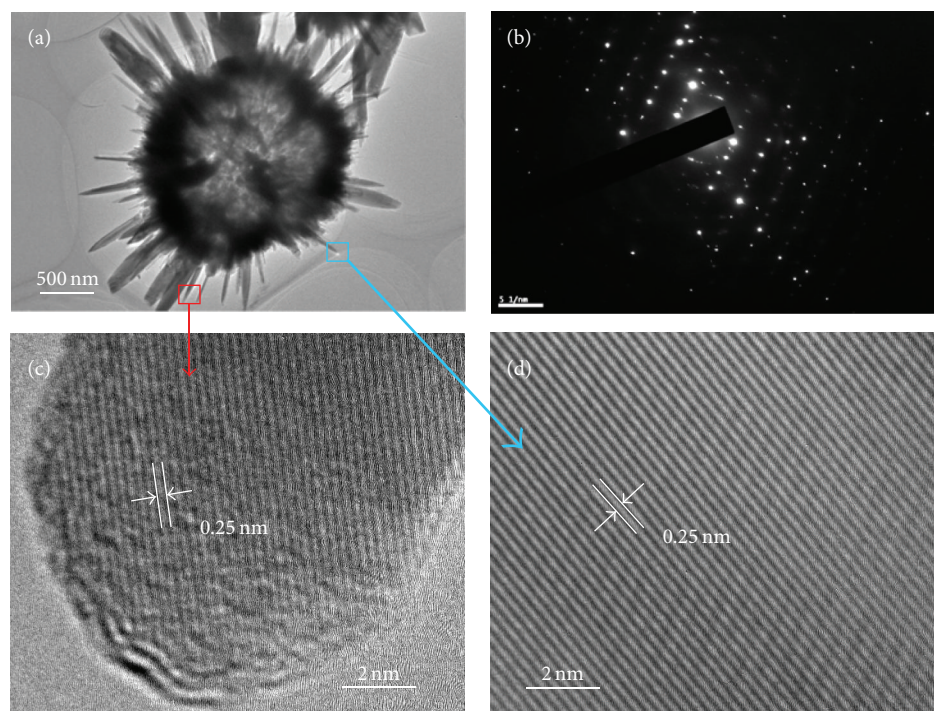

FIGURE 2: (a) TEM image of rambutan-like ZnO HHMs. (b) The SAED patterns corresponding to the selected area of the TEM image. HRTEM images of the tip (c) and the main body (d) of the nanorods on the hollow sphere.
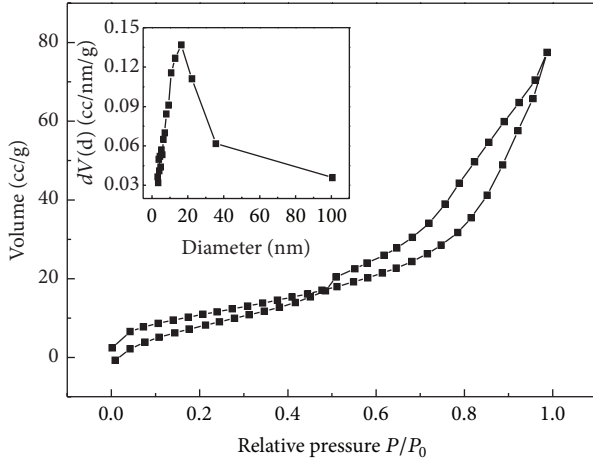
FIGURE 3: Typical N_2 gas adsorption-desorption isotherm of rambutan-like ZnO HHMs. Inset shows the corresponding pore size distribution.

3.2. Effects of Ammonia.

The amount of ammonia is crucial for the formation of unique rambutan-like ZnO HHMs (Figure 4). When 0.3 mL ammonia is put into the reaction system, ZnO spheres are basically formed with rough surface (Figure 4(a)), while some ZnO spheres were obtained with a few nanorods on the surface (Figure 4(b)) by using 0.5 mL ammonia. However, the density of the nanorods decreases on the spheres in the case of 0.7 mL ammonia (Figure 4(c)), and bald ZnO particles emerge by the addition of 1.2 mL ammonia to the reaction system (Figure 4(d)).
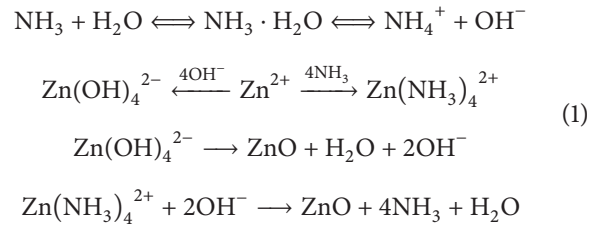
3.3. Effects of CMS.

CMS is served as prior nucleation sites for ZnO at the initial crystallization process. When the CMS concentration is low ($2\,mg\cdot mL^{-1}$), there are a lot of bare ZnO spheres with rough surfaces (Figure 5(a)). And vertical ZnO nanorods grow on the ZnO spheres in the presence of $2.6\,mg\cdot mL^{-1}$ CMS, resulting in rambutan-like morphology (Figure 1(a)). However, sufficient CMS such as $4\,mg\cdot mL^{-1}$ would prevent the growth of nanorods on the surface of ZnO hollow spheres, causing the lower density of the nanorods (Figure 5(b)). Besides, $6\,mg\cdot mL^{-1}$ CMS induces the emergence of many deformed and even broken ZnO flowers (Figure 5(c)), because the nucleation takes place along the prior nucleation sites. When the amount of CMS further increased to $12\,mg\cdot mL^{-1}$ (Figure 5(d)), disordered aggregates are formed.

3.4. Effects of the Reaction Temperature.

Different morphologies are obtained by adjusting the reaction temperature from 80 to 160°C. The aggregation of ZnO spheres (Figure 6(a)) transforms to immature rambutan-like crystals below 100°C (Figure 6(b)), and well-defined rambutan-like ZnO HHMs were obtained at 120°C (Figure 2(b)). However, the density of the nanorods on the surfaces of ZnO HHMs drops down at 140°C (Figure 6(c)), and broken bald spheres show up as the temperature is up to 160°C (Figure 6(d)). These results demonstrate that the rates of the nucleation and crystal growth are sensitive to the reaction temperature [22]. At lower temperature, the crystal growth rate is higher than that of nucleation. The increase of the temperature greatly facilitates the nucleation rate and the newly generated crystal nuclei are easy to aggregate together, realizing crystal growth for adequate space present, leading to the formation of rambutan-like ZnO HHMs. On the contrary, at much higher temperature, the nucleation rate is much higher than that of crystal grain growth, and thereby crystal nuclei are produced.

3.5. Effects of the Reaction Time and Formation Mechanism.

Time-dependent experiments were carried out to deeply understand the formation mechanism of ZnO HHMs (Figures 7(a)–7(d)). Firstly, the products are just composed of solid spheres with the reaction time of 2 h (Figure 7(a)). When the reaction time is 5 h, small nanorods emerge on ZnO spheres (Figure 7(b)) and rambutan-like ZnO HHMs as the reaction time is 12 h (Figure 2(b)). However, the density of the nanorods is decreased by extending the reaction time to 24 (Figure 7(c)) and 48 h (Figure 7(d)), owing to the Ostwald ripening effects (Figure 8).

In general, ZnO has a strong tendency to self-oriented growth. At the initial stage, newly generated ZnO is quickly congregated to spherical aggregates to decrease their surface energies and hence amorphous solid spheres are formed through the following reactions [21, 32]:

$$NH_3 + H_2O \Longleftrightarrow NH_3 \cdot H_2O \Longleftrightarrow NH_4^+ + OH^-$$

$$Zn(OH)_4^{2-} \xleftarrow{4OH^-} Zn^{2+} \xrightarrow{4NH_3} Zn(NH_3)_4^{2+}$$

$$Zn(OH)_4^{2-} \longrightarrow ZnO + H_2O + 2OH^- \qquad (1)$$

$$Zn(NH_3)_4^{2+} + 2OH^- \longrightarrow ZnO + 4NH_3 + H_2O$$

It should be mentioned that the original solid phase might not be well crystallized, owing to rapid spontaneous nucleation. Thus, Ostwald ripening dictates growth and recrystallization after hydrolysis. With time extending, the surface layer of the spheres firstly crystallizes, due to the direct contact with the surrounding solution. As a result, the materials inside the solid spheres have a strong tendency to dissolve, which provides the driving force for the spontaneous Ostwald ripening [33]. This assumption is strongly supported by the above experimental data, while it is different from that described by Shen's group [34]. In their work, original solid microspheres were composed by $Zn(OH)_2$, rather than solid ZnO spheres in our case (Figure S4, supporting information).

The formation process of rambutan-like ZnO HHMs can be further addressed by TEM measurements (Figure 9). At the very early stage, the precipitated crystallites assemble together to form solid ZnO spheres (Figures 9(a) and 9(b)). With the increase of the reaction time, the inner crystallites with higher surface energy would dissolve and transfer outside to produce channels connecting inner and outer spaces in the oxide shells (Figure 9(c)) [35]. Finally, the hollow interior of the ZnO spheres emerged (Figure 9(d)), which is also supported by the broken one from the SEM image (Figure 1(c)).
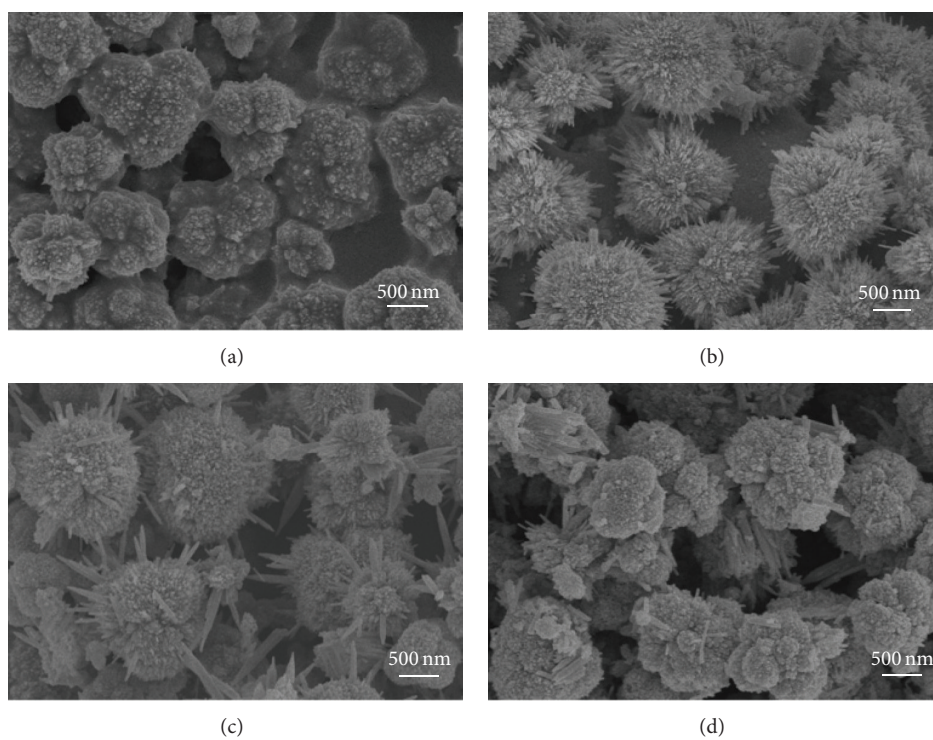
(a)

(b)

(c)

(d)

FIGURE 4: SEM images of the products prepared with different volumes of ammonia: 0.3 mL (a), 0.5 mL (b), 0.7 mL (c), and 1.2 mL (d).
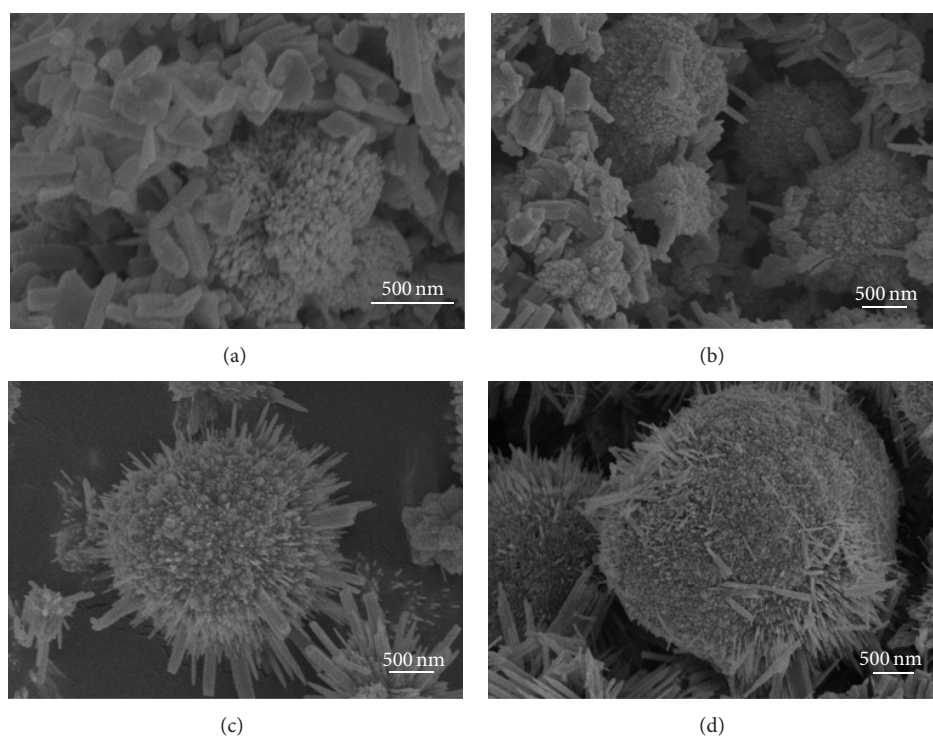

(a)

(b)

(c)

(d)

FIGURE 5: SEM images of the products prepared with different amounts of CMS: 2 mg·mL^{-1} (a), 4 mg·mL^{-1} (b), 6 mg·mL^{-1} (c), and 12 mg·mL^{-1} (d).

(a)

(b)

(c)

(d)

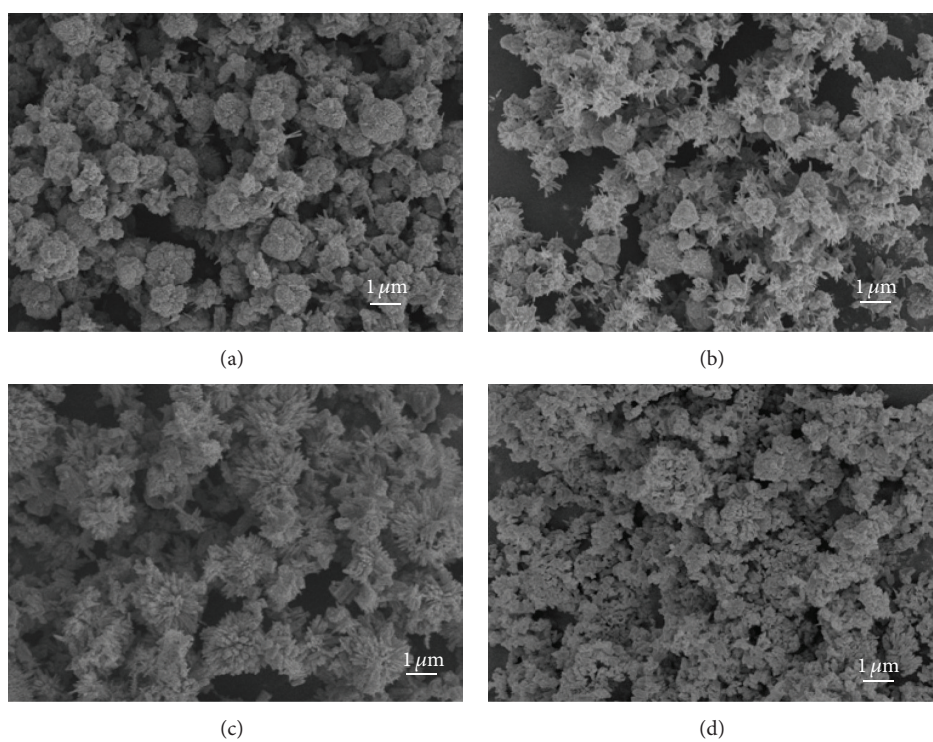Figure 6: SEM images of the products obtained at different reaction temperature: 80°C (a), 100°C (b), 140°C (c), and 160°C (d).
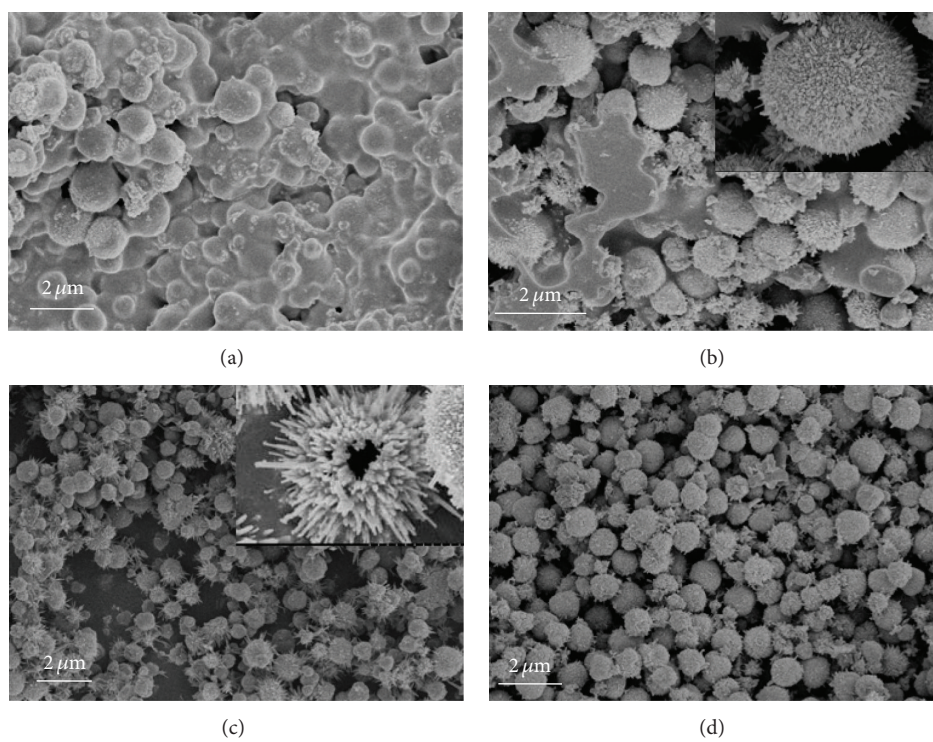

(a)

(b)

(c)

(d)

Figure 7: SEM images of the products obtained at different reaction time: 2 h (a), 5 h (b), 24 h (c), and 48 h (d). Inset shows high magnification of the images (b) and (c).
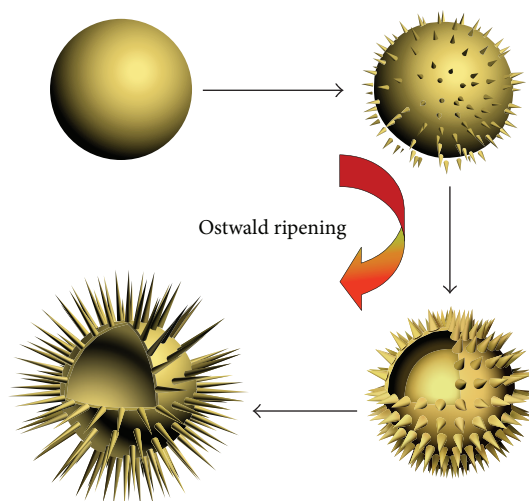
FIGURE 8: The formation mechanism of rambutan-like ZnO HHMs based on time-dependent evolution of the growth process.
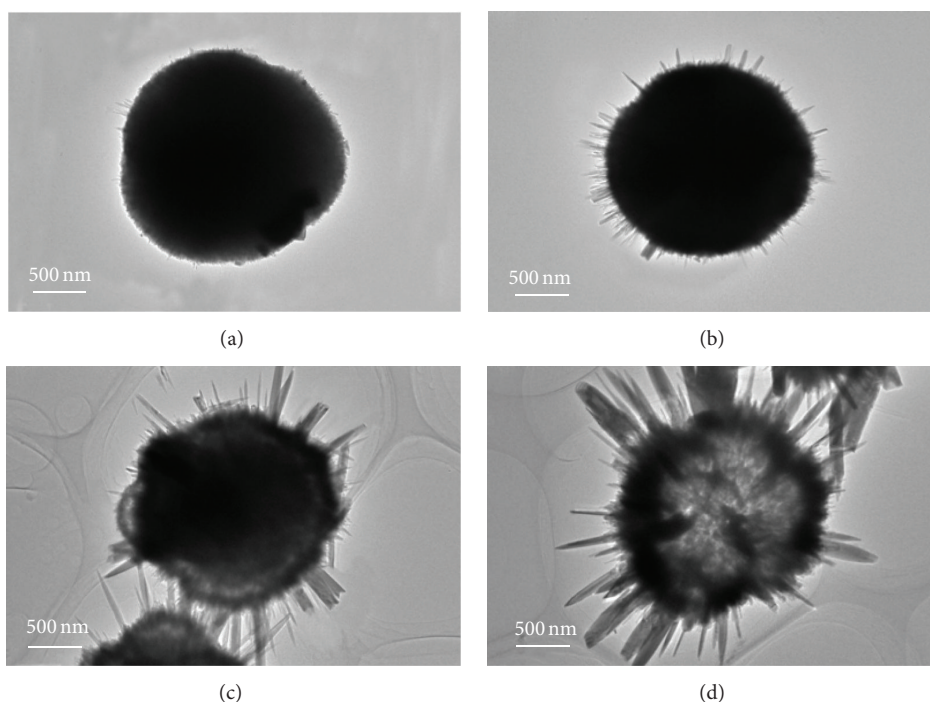

(a)

(b)

(c)

(d)

FIGURE 9: TEM images of the products obtained at different reaction time: 2 h (a), 5 h (b), 8 h (c), and 12 h (d).

In our study, CMS, as a soft template, not only facilitates the formation of well-dispersed rambutan-like ZnO HHMs, but also serves as a diffusion boundary to restrain rapid crystal growth and prevent direct fusion among the ZnO spheres during the ripening process. Based on the analysis, the formation of rambutan-like ZnO HHMs is ascribed to CMS-assisted Ostwald ripening mechanism.

3.6. Photocatalytic Activity. In the last decade, photocatalytic oxidation process provides an effective route for the destruction of hazardous and toxic pollutants [36]. RhB were chosen as a model pollutant to evaluate the photocatalytic activity of rambutan-like ZnO HHMs.

Figure 10(a) shows the photocatalytic degradation of RhB in the aqueous solution as a function of exposure time in the presence of the ZnO catalysts under UV light irradiation. With the increase of the reaction time, the absorption peak intensity of RhB greatly drops down and even disappears within 90 min in the presence of rambutan-like ZnO HHMs. The time for photodegradation of RhB is much shorter than that of hollow ZnO nanospheres (150 min) [37]. The apparent reaction rate constant ($k_{app.}$) is found to be 4.15×10^{-2} min^{-1} for rambutan-like ZnO HHMs (Figure 10(b)), while $k_{app.}$ is
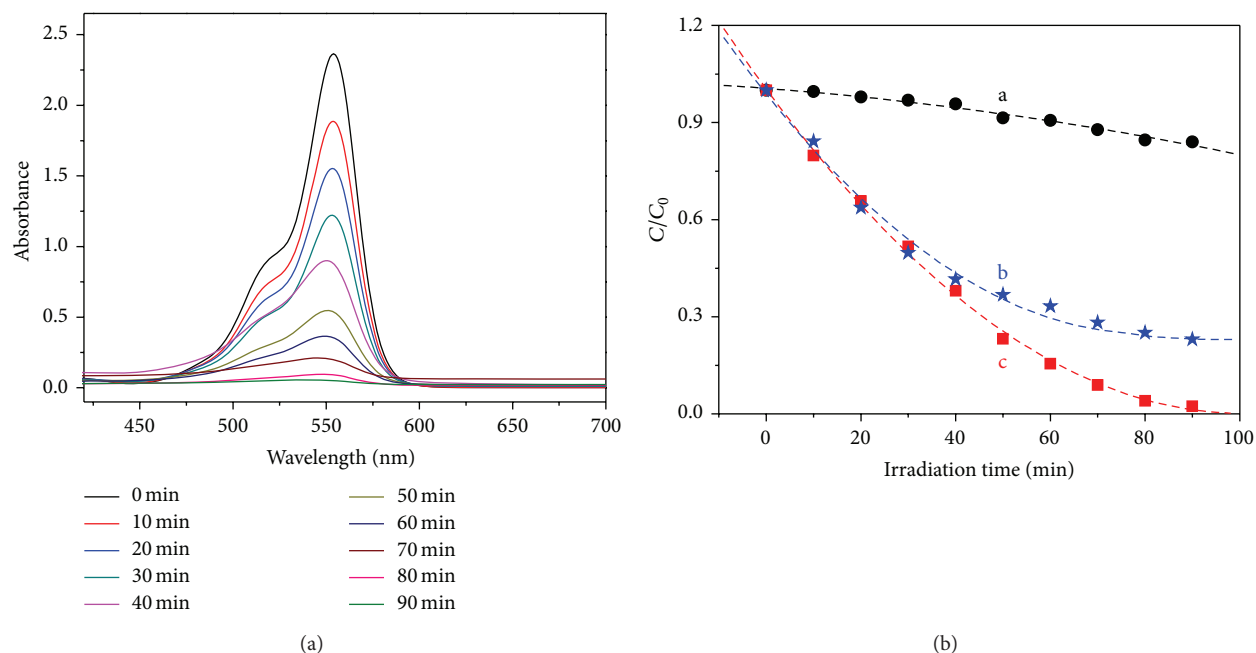
(a)

(b)

FIGURE 10: (a) UV-vis absorption spectra from the 2.5×10^{-5} M RhB solution with 0.3 mg·mL^{-1} hollow rambutan-like ZnO HHMs at different time intervals and (b) RhB photodegradation curves of the C/C_0 versus time in the absence (curve a) and presence of commercial ZnO (curve b) or rambutan-like ZnO HHMs (curve c).

2.12×10^{-2} min^{-1} for the blank system (without ZnO). The $k_{app.}$ of rambutan-like ZnO HHMs is much higher than the photocatalysis of Congo red (4.15×10^{-2} min^{-1}) using hollow flower-like ZnO structures as a catalyst [21], although the amount of the catalysts used is at the same level. After 90 min of UV irradiation, almost 100% of RhB molecules are decomposed for rambutan-like ZnO HHMs, unlike that of commercial ZnO with 23% of RhB molecules remaining. It indicates that the photocatalytic activity of rambutan-like ZnO HHMs is much higher than that of commercial ZnO. Moreover, the rambutan-like ZnO HHMs also display highly photocatalytic stability after five times recycling (Figure S5, supporting information).

Figure S6 (supporting information) shows the photocatalytic performance when using the samples obtained at different reaction time. It is found that the photocatalytic activity increased when the morphology is more close to the structure of ZnO HHMs, owing to the enlarged surface area of the unique structures. RhB molecules are excited by the absorption of UV light, and electrons are injected into the conduction band of ZnO particles, facilitating the oxidation of RhB molecules [38]. These results clearly demonstrate that ZnO HHMs have enhanced photocatalytic activity. In addition, the exposed facets of the ZnO structures also play an important role. The nanorods of ZnO HHMs are growing along the $\{10\bar{1}1\}$ planes. The weaker coordinated O atoms on the surface are more likely to be saturated by H atoms in aqueous solution, thereby releasing more free OH radicals under irradiation, as supported by the previous work [39].

4. Conclusions

In summary, a simple and green pathway has been explored for the construction of rambutan-like ZnO HHMs under hydrothermal conditions. CMS, as a soft template, plays an important role in the synthesis procedure. The formation of rambutan-like ZnO HHMs was attributed to CMS-assisted Ostwald ripening process. The as-prepared ZnO structures were demonstrated as a good catalyst for photocatalytic degradation of RhB. This work not only provides a simple method to prepare ZnO hollow structures, but also sheds some light on the improvement of the photocatalytic performance by designing efficient catalysts.

Conflict of Interests

The authors declare that there is no conflict of interests regarding the publication of this paper.

Acknowledgment

References

[1] P. Baviskar, A. Ennaoui, and B. Sankapal, "Influence of processing parameters on chemically grown ZnO films with low cost Eosin-Y dye towards efficient dye sensitized solar cell," *Solar Energy*, vol. 105, pp. 445–454, 2014.

[2] A. B. Gurav, S. S. Latthe, R. S. Vhatkar et al., "Superhydrophobic surface decorated with vertical ZnO nanorods modified by stearic acid," *Ceramics International*, vol. 40, no. 5, pp. 7151–7160, 2014.

[3] P. Labouchere, A. K. Chandiran, T. Moehl et al., "Passivation of ZnO nanowire guests and 3D inverse opal host photoanodes for dye-sensitized solar cells," *Advanced Energy Materials*, vol. 4, no. 12, 2014.

[4] L. Liu, K. Hong, X. Ge, D. Liu, and M. Xu, "Controllable and rapid synthesis of long ZnO nanowire arrays for dye-sensitized solar cells," *The Journal of Physical Chemistry C*, vol. 118, no. 29, pp. 15551–15555, 2014.

[5] A. Katoch, S.-W. Choi, H. W. Kim, and S. S. Kim, "Highly sensitive and selective H_2 sensing by ZnO nanofibers and the underlying sensing mechanism," *Journal of Hazardous Materials*, vol. 286, no. 9, pp. 229–235, 2015.

[6] S. Hussain, T. Liu, M. Kashif et al., "Surfactant dependent growth of twinned ZnO nanodisks," *Materials Letters*, vol. 118, pp. 165–168, 2014.

[7] T. Bai, Y. Xie, C. Zhang, Y. Zhang, J. Hu, and J. Wang, "Facile fabrication of ZnO nanorods/ZnO nanosheet-spheres hybrid photoanode for dye-sensitized solar cells," *Functional Materials Letters*, vol. 8, no. 1, Article ID 1550012, 2015.

[8] P. P. Das, S. A. Agarkar, S. Mukhopadhyay, U. Manju, S. B. Ogale, and P. S. Devi, "Defects in chemically synthesized and thermally processed ZnO nanorods: implications for active layer properties in dye-sensitized solar cells," *Inorganic Chemistry*, vol. 53, no. 8, pp. 3961–3972, 2014.

[9] J. Yang, Y. Lin, Y. Meng, and Y. Lin, "Oriented ZnO nanotubes arrays decorated with TiO2 nanoparticles for dye-sensitized solar cell applications," *Applied Physics A*, vol. 114, no. 4, pp. 1195–1199, 2014.

[10] J.-S. Jeong, B.-H. Choe, J.-H. Lee, J.-J. Lee, and W.-Y. Choi, "ZnO-coated TiO$_2$ nanotube arrays for a photoelectrode in dye-sensitized solar cells," *Journal of Electronic Materials*, vol. 43, no. 2, pp. 375–380, 2014.

[11] T. A. Safeera, N. Johns, P. V. Athma, P. V. Sreenivasan, and E. I. Anila, "Synthesis and characterization of ZnO nanonails," *AIP Conference Proceedings*, vol. 1620, no. 1, pp. 572–577, 2014.

[12] L. Song, Q. Jiang, P. Du, Y. Yang, J. Xiong, and C. Cui, "Novel structure of TiO$_2$-ZnO core shell rice grain for photoanode of dye-sensitized solar cells," *Journal of Power Sources*, vol. 261, no. 1, pp. 1–6, 2014.

[13] S. Zhu, L. Shan, X. Chen et al., "Hierarchical ZnO architectures consisting of nanorods and nanosheets prepared via a solution route for photovoltaic enhancement in dye-sensitized solar cells," *RSC Advances*, vol. 3, no. 9, pp. 2910–2916, 2013.

[14] T.-T. Miao, Y.-R. Guo, and Q.-J. Pan, "The SL-assisted synthesis of hierarchical ZnO nanostructures and their enhanced photocatalytic activity," *Journal of Nanoparticle Research*, vol. 15, no. 6, pp. 1–12, 2013.

[15] K. Wijeratne and J. Bandara, "Aspect-ratio dependent electron transport and recombination in dye-sensitized solar cells fabricated with one-dimensional ZnO nanostructures," *Electrochimica Acta*, vol. 148, no. 1, pp. 302–309, 2014.

[16] X. Zhou, W. Feng, C. Wang et al., "Porous ZnO/ZnCo$_2$O$_4$ hollow spheres: synthesis, characterization, and applications in gas sensing," *Journal of Materials Chemistry A*, vol. 2, no. 41, pp. 17683–17690, 2014.

[17] J. Shi, Y. Liu, X. Zhou, Q. Su, J. Zhang, and G. Du, "Hierarchical ZnO hollow microspheres with strong violet emission and enhanced photoelectrochemical response," *Materials Letters*, vol. 132, no. 1, pp. 421–424, 2014.

[18] C. Ottone, K. Bejtka, A. Chiodoni et al., "Comprehensive study of the templating effect on the ZnO nanostructure formation within porous hard membranes," *New Journal of Chemistry*, vol. 38, no. 5, pp. 2058–2065, 2014.

[19] R. Selvakumar, N. Seethalakshmi, P. Thavamani, R. Naidu, and M. Megharaj, "Recent advances in the synthesis of inorganic nano/microstructures using microbial biotemplates and their applications," *RSC Advances*, vol. 4, no. 94, pp. 52156–52169, 2014.

[20] J. Yu and X. Yu, "Hydrothermal synthesis and photocatalytic activity of zinc oxide hollow spheres," *Environmental Science & Technology*, vol. 42, no. 13, pp. 4902–4907, 2008.

[21] J.-J. Feng, Q.-C. Liao, A.-J. Wang, and J.-R. Chen, "Mannite supported hydrothermal synthesis of hollow flower-like ZnO structures for photocatalytic applications," *CrystEngComm*, vol. 13, no. 12, pp. 4202–4210, 2011.

[22] A.-J. Wang, Q.-C. Liao, J.-J. Feng, P.-P. Zhang, A.-Q. Li, and J.-J. Wang, "Apple pectin-mediated green synthesis of hollow double-caged peanut-like ZnO hierarchical superstructures and photocatalytic applications," *CrystEngComm*, vol. 14, no. 1, pp. 256–263, 2012.

[23] A. B. Djurišić, X. Y. Chen, and Y. H. Leung, "Recent progress in hydrothermal synthesis of zinc oxide nanomaterials," *Recent Patents on Nanotechnology*, vol. 6, no. 2, pp. 124–134, 2012.

[24] Y.-W. Cheng, H.-L. Su, W.-H. Lin, and C.-F. Lin, "Forming extremely smooth ZnO thin film on silicon substrates for growth of large and well-aligned ZnO rods with the hydrothermal method," *Journal of Sol-Gel Science and Technology*, vol. 70, no. 1, pp. 81–89, 2014.

[25] W. Guo, M. Fu, C. Zhai, and Z. Wang, "Hydrothermal synthesis and gas-sensing properties of ultrathin hexagonal ZnO nanosheets," *Ceramics International*, vol. 40, no. 1, pp. 2295–2298, 2014.

[26] C. Wang, S. Ma, A. Sun et al., "Characterization of electrospun Pr-doped ZnO nanostructure for acetic acid sensor," *Sensors and Actuators B: Chemical*, vol. 193, no. 31, pp. 326–333, 2014.

[27] A. C. Janaki, E. Sailatha, and S. Gunasekaran, "Synthesis, characteristics and antimicrobial activity of ZnO nanoparticles," *Spectrochimica Acta Part A: Molecular and Biomolecular Spectroscopy*, vol. 144, no. 5, pp. 17–22, 2015.

[28] V. M. Guérin, J. Elias, T. T. Nguyen, L. Philippe, and T. Pauporté, "Ordered networks of ZnO-nanowire hierarchical urchin-like structures for improved dye-sensitized solar cells," *Physical Chemistry Chemical Physics*, vol. 14, no. 37, pp. 12948–12955, 2012.

[29] J.-J. Feng, Z.-Z. Wang, Y.-F. Li, J.-R. Chen, and A.-J. Wang, "Control growth of single crystalline ZnO nanorod arrays and nanoflowers with enhanced photocatalytic activity," *Journal of Nanoparticle Research*, vol. 15, no. 4, pp. 1–12, 2013.

[30] Z. Deng, M. Chen, G. Gu, and L. Wu, "A facile method to fabricate ZnO hollow spheres and their photocatalytic property," *The Journal of Physical Chemistry B*, vol. 112, no. 1, pp. 16–22, 2008.

[31] B. Li and Y. Wang, "Facile synthesis and enhanced photocatalytic performance of flower-like ZnO hierarchical microstructures," *The Journal of Physical Chemistry C*, vol. 114, no. 2, pp. 890–896, 2010.

[32] J. Duan, X. Huang, and E. Wang, "PEG-assisted synthesis of ZnO nanotubes," *Materials Letters*, vol. 60, no. 15, pp. 1918–1921, 2006.

[33] X. W. Lou, L. A. Archer, and Z. Yang, "Hollow micro-/nanos-tructures: synthesis and applications," *Advanced Materials*, vol. 20, no. 21, pp. 3987–4019, 2008.

[34] Y. F. Zhu, D. H. Fan, and W. Z. Shen, "Template-free synthesis of zinc oxide hollow microspheres in aqueous solution at low temperature," *The Journal of Physical Chemistry C*, vol. 111, no. 50, pp. 18629–18635, 2007.

[35] J. Li and C. Z. Hua, "Hollowing Sn-doped TiO_2 nanospheres via Ostwald ripening," *Journal of the American Chemical Society*, vol. 129, no. 51, pp. 15839–15847, 2007.

[36] Z. Zhang, M. Zhang, J. Deng et al., "Potocatalytic oxidative degradation of organic pollutant with molecular oxygen activated by a novel biomimetic catalyst $ZnPz(dtn-COOH)_4$," *Applied Catalysis B: Environmental*, vol. 132-133, no. 27, pp. 90–97, 2013.

[37] C. Zhu, B. Lu, Q. Su, E. Xie, and W. Lan, "A simple method for the preparation of hollow ZnO nanospheres for use as a high performance photocatalyst," *Nanoscale*, vol. 4, no. 10, pp. 3060–3064, 2012.

[38] W. Teng, X. Li, Q. Zhao, J. Zhao, and D. Zhang, "*In situ* capture of active species and oxidation mechanism of RhB and MB dyes over sunlight-driven Ag/Ag_3PO_4 plasmonic nanocatalyst," *Applied Catalysis B: Environmental*, vol. 125, pp. 538–545, 2012.

[39] J. Chang and E. R. Waclawik, "Facet-controlled self-assembly of ZnO nanocrystals by non-hydrolytic aminolysis and their photodegradation activities," *CrystEngComm*, vol. 14, no. 11, pp. 4041–4048, 2012.